Journal of Umm Al-Qura University for Applied Science 6 (2020) 1-5

Journal of Umm Al-Qura University for Applied Science

journal homepage: https://uqu.edu.sa/en/jas/87823

Flavonoid Biosynthesis Genes During Seed Development in *Arabidopsis Thaliana*

Maha Aljabri[a,b,c,*], James Doughty[c] and Rod J. Scott[c].

[a] *Department of Biology, Faculty of Applied Science, Umm Al-Qura University, Makkah, Saudi Arabia.*
[b] *Research Laboratories Centre, Faculty of Applied Science, Umm Al-Qura University, Makkah, Saudi Arabia*
[c] *Department of Biology and Biochemistry, Bath university, Claverton Down, Bath, UK, BA2 7AY.*

ARTICLE INFO

Article History:
Submission date: 25/2/2020
Accepted date: 22/6/2020

Keywords:
Seed development, Endosperm cellularisation, Interploidy crosses, Transparent testa mutants, Flavonoid.

ABSTRACT

Many plants, including agronomically important species, exhibit post-zygotic barriers to hybridisation, in both interploidy crosses within species and interspecific crosses between related species. For instance, crosses between diploid (2x) and tetraploid (4x) plants result in a triploid block where serious endosperm under- or over-proliferation kills the developing triploid embryo. Although most ecotypes of the model species Arabidopsis thaliana tolerate 2x × 4x crosses to create a large viable seed, one ecotype, Columbia (Col-0), exhibits a triploid block when the paternal parent is certainly tetraploid. Recently, lack-of-function mutants in the flavonoid biosynthesis pathway (FBP) that operate in the seed coat have been identified as highly effective maternal suppressors of the Col4x-mediated triploid block. The present hypothesis is that a maternal messenger responsible for regulating the appropriate timing of endosperm cellularisation usually is attenuated or blocked simply by an operating FBP; consequently, mutations in the FBP enhance cellularisation and decrease seed lethality by removing the signalling block. This research attempts to understand the role of the FBP and its products in the seed development regulation following 2x × 4x crosses. To this end, an assortment of some of the FBP mutants was assembled to assess their influence on alleviating the triploid block using confocal and light microscopy. The results revealed that many (although not all) mutations of the FBP alleviated the triploid block and that, specifically, perturbations to FBP that led to a reduced amount of proanthocyanidins was connected with 'rescue' from Col4x-induced seed lethality. These details could have a potential biotechnological utility in overcoming hybridisation barriers when discovering new hybrids to increase endosperm size and, thus, seed yield in crop plants.

1. Introduction

The global population is projected to increase to approximately 10 billion by 2050; therefore, increasing food production is critical [1]. Seeds constitute approximately 68% of the world's food supply and are a vital source of nutrition [2]. Seeds result from sexual reproduction in plants through double fertilisation and are made up of three components: the seed coat (testa), the embryo and the endosperm (Figure 1A) [3]. The development of the seed coat is determined by the maternal genome, whereas the endosperm and the embryo develop under the control of both parental genomes (Figure 1B) [2]. Seed development entails two distinct phases: embryo development and seed maturation [4].

Most flowering plants, including *Arabidopsis thaliana*, have an embryo sac containing seven cells, which consist of four cell types: the egg cell; two synergid cells, which are essential for pollen tube attraction; the central cell; and three cells called antipodal cells, whose function is currently unknown. The embryo sac is surrounded by diploid integument tissues that together constitute the ovule. The egg cell (n) is fertilised by one of the sperm cells (n) delivered through the pollen tube, resulting in a diploid zygote (embryo 2n). The homodiploid central cell (2n) is fertilised by the second sperm cell (n) giving rise to the triploid endosperm (3n), which functions as a nutrient source for the embryo. The triploid endosperm progresses through a free-nuclear multinucleate stage up to the pre-globular embryo stage followed by cellularisation. The ovule integuments differentiate to form the seed coat that protects the seed during embryogenesis, dormancy and germination [5].

The embryo, endosperm and integument cells need to synchronise their growth during seed development. The interaction between the endosperm and integuments during growth may be an important factor in determining the seed size [6]. Thus, the aberrant behaviour of the zygotic (including the endosperm) or maternal tissues can affect the seed size; this can result from unbalancing the programme of endosperm development due to interspecific and interploidy hybridisation [7]. Maternal modifier genes, such as members of the flavonoid biosynthesis pathway (FBP), can re-impose a normal (balanced) programme on the endosperm—in the endothelium—and restore a relatively normal viability [8, 9].

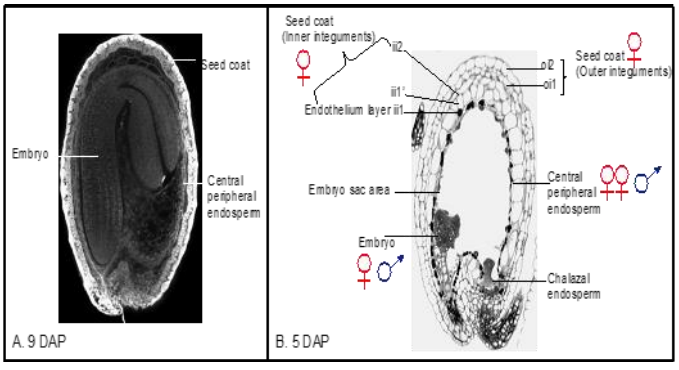

Figure 1. A. *thaliana* seed anatomy at 5 and 9 days after pollination (DAP). A. General seed structure. **B. The seed at the incipient endosperm cellularisation stage.** The outer integument includes the outer integument second layer (oi2) termed 'epidermis' and outer integument first layer (oi1) termed 'palisade'. The inner integument contains ii2, ii1' and ii1 and is called 'endothelium' (adapted from [10]).

* **Corresponding Author**
Department of Biology, Faculty of Applied Science, Umm Al-Qura University, Makkah, Saudi Arabia.
E-mail address: myjabri@uqu.edu.sa (Maha Aljabri).

1.1. FBP

Flavonoids, a diverse family of plant secondary metabolites, are synthesised from the phenylpropanoid pathway by converting phenylalanine to 4-malonyl-CoA [11]. In the Brassicaceae, flavonoids have many roles such as attraction of insects to aid with pollen dispersal and regulation of polar auxin transport, as well as a physiological role in seed dormancy or viability [12-16].

1.2. Triploid block in A. thaliana seed development

Generally, the normal development of the endosperm involves a parental genomic ratio of 2m:1p, which is the ideal balance between the paternal proliferation genes (growth promoters) and the maternal growth inhibition genes to form a healthy seed. Any disruption of this balance can cause developmental defects. Any imbalance in this ratio causes negative consequences for the developing seed, which can result in lethality [17].

A triploid block is common in plants, but *A. thaliana* exhibits a tetraploid block [9]. A triploid block in the Col-0 ecotype can be due to mating a diploid parent with a tetraploid parent (2x × 4x or 4x × 2x = 3x), and the result of this mating is abnormal viable progeny [9, 18]. Dilkes *et al.* showed that the outcome for 2x × 4x crosses using the Col-0 ecotype is largely non-viable progeny and a much lower tolerance than the seeds with a parent from the L*er* ecotype in interploidy crosses [8]. Therefore, understanding post-zygotic hybridisation barriers are critical to be able to manipulate and overcome them to potentially create larger seeds for yield increase in agriculture.

1.3. Regulation of endosperm development—a maternal cellularisation signal

As discussed earlier, the behaviour of seeds that result from hybridisation is significantly influenced by endosperm cellularisation. Dilkes *et al.* pointed out that a loss-of-function mutation in the *TRANSPARENT TESTA GLABRA2 (TTG2)* gene in *A. thaliana* – which encodes a transcription factor of the WRKY family [8]; means that the seed parent is almost completely resistant to Col-0 killing, indicating that the maternal integument tissues regulate endosperm cellularisation. Therefore, if *TTG2* plants were to be used as the maternal source, then the absence of *TTG2* proteins act as 'rescuers', modifying the triploid block seen in Col-0 and producing small seeds [5,8]. The FBP is present in an endothelium layer: the ii1 layer of maternal inner integument layers (Figure 1). Hence, by combining our knowledge from the molecular players in the FBP and the effect of the triploid block, we hypothesise that the transport of a cellularising factor between the maternal integuments and the endosperm is inhibited by a functional FBP in *A. thaliana* interploidy cross (Col2x × Col4x). This is known as the maternal cellularisation signal hypothesis (Figure 2). This research investigates the role of the FBP (in a few genes) and its intermediates in regulating paternal Col4x-induced seed lethality ('Col-killer') in *A. thaliana*.

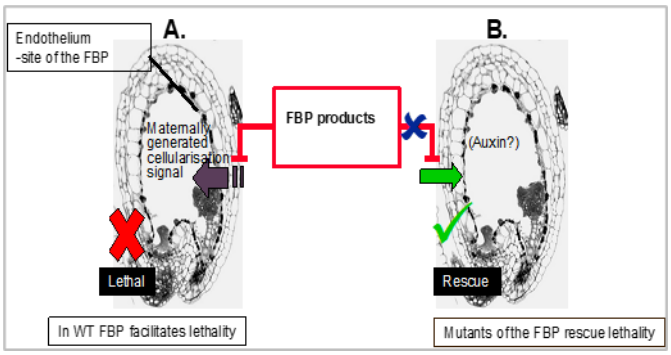

Figure 2. Model displaying the effect of FBP products in wild-type and FBP mutant in *A. thaliana.* **A.** FBP inhibits the action of an endosperm cellularisation factor (2x × 4x). The model predicts that the maternal integument layers create a maternal cellularisation factor that is transported into the endosperm through the endothelium (purple arrow). The FBP (red box) in the endothelium layer inhibits this signal. Consequently, endosperm cellularisation does not occur or is significantly late. Delayed cellularisation allows lethal over-proliferation of the endosperm, as is seen in Col2x × Col4x crosses. **B.** FBP mutants alleviate the inhibition/transport of the cellularisation factor. Presenting a *tt* mutation (blue x) disrupts the FBP (red box) in the endothelium layer. This prevents or causes a decrease in the production of the ultimate products of the pathway (e.g. proanthocyanidins (PAs)). Therefore, the transportation of the cellularisation factor through the maternal integument layers to the endosperm is increased (green arrow). Consequently, endosperm cellularisation happens early, thus rescuing Col4x-mediated seed lethality [19].

2. Results and discussion

Overall, seeds produced from crosses involving various maternal FBP mutants in the Col-0 ecotype and Col4x differed from each other as well as from seeds derived from balanced 2x × 2x in their weight and size (Figures 3, 4 and Table 1). In balanced cross Col2x × Col2x, at 5 DAP, the central peripheral endosperm was cellularised and the embryo already reached the heart stage. By 7 DAP, even though the chalazal endosperm continued to be present, the embryo reached the torpedo stage. By seed maturity, balanced crosses generated viable, plump seeds (Figure 4 and Table 1).

Confocal microscopy analysis revealed well-defined differences in seed development between FBP mutants crossed with Col4x and the control (Col2x × Col4x). The size of seed seemed to increase with seed development generally in most crosses from 5 to 7 DAP. At 5 DAP, the growth of embryos (3n) was inhibited and remained at (a) the early heart stage of development in Col2x and *tt4*, (b) the heart stage in *tt6*, and (c) the globular stage in *tt14/19*, *tt10*, and *anl1*. Notably, by 7 DAP, a significant delay in development was clear for many lines (Col2x, *tt4*, *tt14/19*, *tt10*, and *anl1*) where embryo development remained at a globular-like stage, being overgrown and abnormal in structure. As seen in Figure 4 and Table 1, most crosses between FBP mutants in the Col-0 background and Col4x pollen parents led to dramatic rises in the embryo sac area between 5 and 7 DAP (*tt4, tt6, tt19/14, tt10,* and *anl1).*This contrasts with the control Col2x × Col4x cross, where expansion of the embryo sac between 5 and 7 DAP was small.

The central peripheral endosperm endured accelerated mitosis, resulting in delayed endosperm cellularisation at 5 DAP. The chalazal endosperm size in all crosses was increased, and some were vacuolated between 5 and 7 DAP, as can be clearly observed in *tt6* × Col4x crosses (Figure 4 (C)). At 5 DAP, the chalazal endosperm area in *anl1*× Col4x cross was the smallest, with a mean of 764 µm^2. At 7 DAP, the chalazal endosperm area in *anl1* × Col4x cross was the largest, with a mean area of 52,555 µm^2. Taken together, the data indicate that maternally carried FBP mutations have a dramatic effect on chalazal endosperm development. At 5 and 7 DAP, *tt10* × Col4x crosses collapse of chalazal endosperm was evident along with nodule formation on the peripheral endosperm (Figure 4 (E)). In *tt19/14* × Col4x, the number of nodules was lowest at 5 DAP, with a mean of 0.3. Moreover, the number of nodules in tt10 × Col4x was smallest at 7 DAP, with a mean of 0.1 (Table 1).

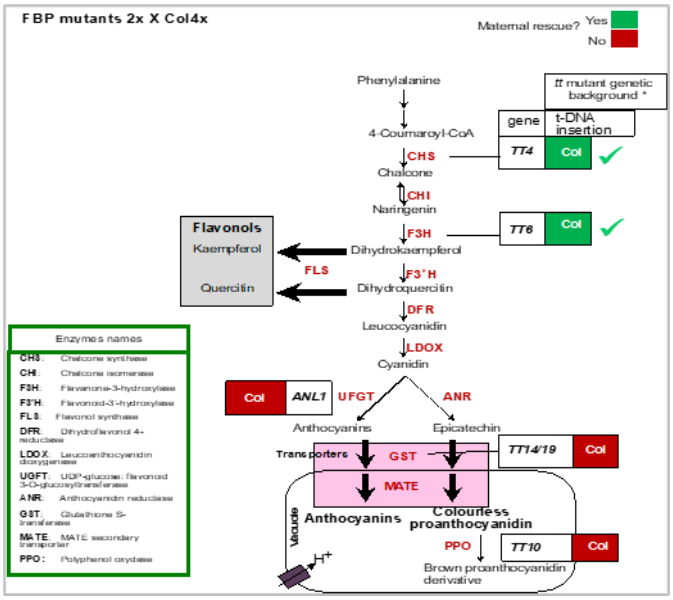

Figure 3. The FBP and its potential role controlling endosperm cellularisation in interploidy hybrids. An updated model of FBP in the *A. thaliana* seed coat. The pink box shows transporters into the vacuole. The white box indicates the vacuole. Mutant alleles of genes with green backgrounds rescue Col4x-induced seed lethality (paternal excess). Genes with red backgrounds do not rescue seed lethality. The presence of an active pathway can be proposed to disrupt the transport of a cellularisation factor into the endosperm. Enzymes are shown with a red colour, and their names are listed in the green box to the left (modified from [16, 19, 20, 21]).

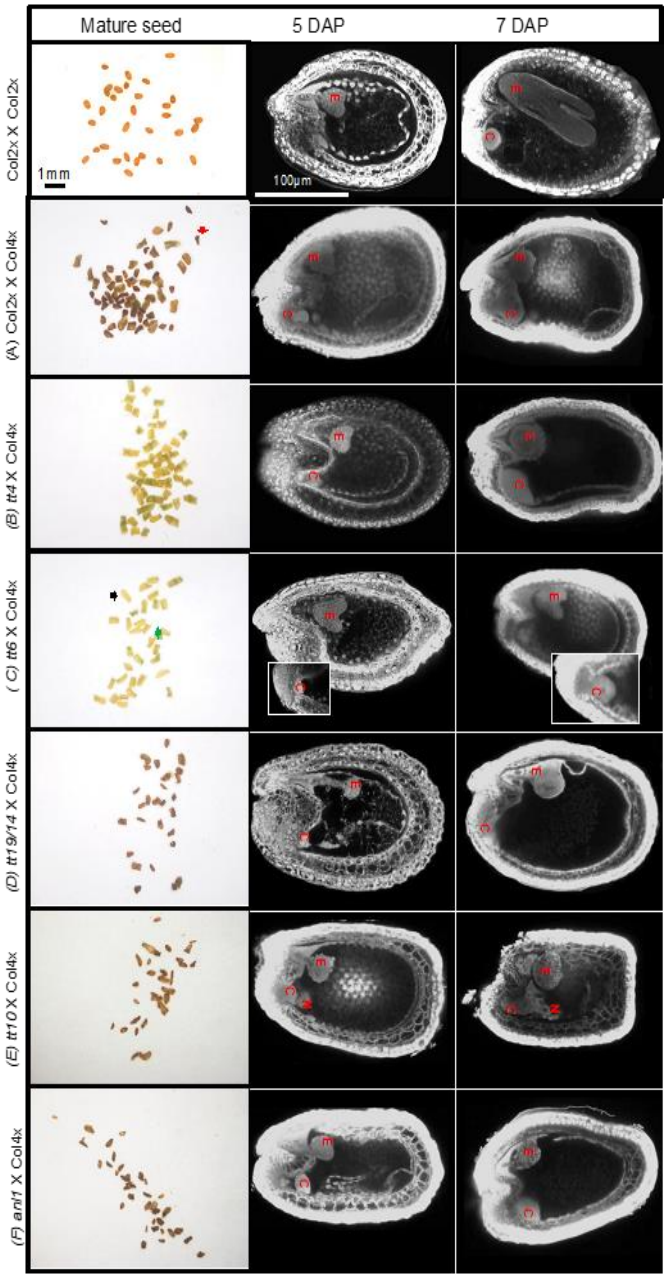

Figure 4. Effect of some mutations in the FBP on seed development (the Col-0 ecotype) following interploidy crosses. The first row: diploid crosses (2x × 2x) in the Col-0 ecotype. Column 1 (left): mature seeds (having paternal excess) derived from interploidy crosses (2x × 4x). Columns 2 (middle) and 3 (right): Confocal laser scanning photomicrographs of tt mutants in interploidy crosses at 5 and 7 DAP. Seeds were classified and counted as plump (indicated using a black arrow), burst (indicated using a green arrow) or shrivelled (indicated using a red arrow). Abbreviation: E: embryo; C: chalazal endosperm and N: nodules. All magnifications: 20x. Scale bars, column 1: 1 mm; columns 2 and 3: 100 µm

These results support previous research in 2x × 4x interploidy crosses that the seed has an embryo (3x) containing twice the normal number of paternal genomes (1m: 2p). The endosperm resulting from these crosses (4x) was affected by paternal genome dosage (2m: 2p), which led to abnormal seed development. This was characterised by accelerated endosperm mitosis and a delay in, or failure of, endosperm cellularisation; this excessive over-proliferation was linked to embryo abortion [7, 8].

Table 1 shows a variation in seed weight amongst seeds derived from the various FBP mutant crosses. Mature seeds arising from *tt4* × Col4x were the heaviest (mean weight: 25 µg). Subsequently, seeds derived from *tt6* with Col4x cross-produced heavy seeds in comparison to seeds derived from the Col2x × Col4x control had a mean weight of 22 µg. However, several mutants (*anl1* and *tt10*) produced seeds which were lighter than the control cross with *anl1*, creating the lowest seeds weight (6 µg).

In general, most FBP mutant's mature seeds have an irregular shape and in the same crossing line. There are some plump and burst seeds (large seed size) and shrivelled seeds (small seed size). Notably, seeds derived from *tt4* and *tt6* crossed to Col4x are noticeably more angular and larger than Col2x × Col4x seeds, most having angular, plump and burst shape seeds (rescue–viable category) (Figure 4 (B) and (C)). Mature seeds of *tt14/19*, *tt10*, and *anl1* with Col4x are different from the control cross; Col2x × Col4x being smaller and irregularly shaped almost all have shrivelled seeds (lethal–unviable category) (Figure 4 (D), (E), and (F)).

Furthermore, the seed-coating phenotype of the *tt4* and *tt6* mutants was yellowish. *TT4* works at the first stage of the FBP and encodes chalcone synthase (CHS) (Figure 3); therefore, its disruption should, in theory, have a substantial influence on the FBP. Significantly, the *tt6* mutant could affect good 'rescue' which encodes F3H, the next enzyme in the FBP. *tt14/19* had a tan brown seed coat. Kubo *et al.* (2007) reported lower levels of anthocyanin in plant tissues, which reflects the importance of *TT14/19* in anthocyanin transport [22]. *tt10* seeds had a very pale brown phenotype. *TT10*, the last gene of the FBP, whose product operates inside the vacuole of the endothelium layer, provided useful information on the potential role of proanthocyanidins (PAs) in the rescue of Col4x-induced seed lethality. *TT10* has a role in the oxidation of PAs [23] and catalyses the change to PAs from procyanidin. *anl1* seed coat colour was darker than that of the control cross.

According to effects from the Col-0 FBP mutant study (Figure 4 and Table 1), several mutants, but not all, were capable of rescuing Col4x-induced seed lethality. Seed weight and the percentage of plump/burst seeds were consistent with one another as indicators of 'rescue' and that was in *tt4* and *tt6*. *tt4* and *tt6* are enzymatic steps operating early in the FBP (Figure 2) that would potentially block the production of all main classes of flavonoids [24]. Notably, seeds caused from maternal *anl1* (having less anthocyanin and potentially more PAs), as confirmed by Kubo *et al.* (2007), had higher seed lethality than the control Col2x × Col4x. Furthermore, they stated that a possible description of *anl1* seed colour phenotype, even with a reduced anthocyanin level, were faults in a) the regulatory gene of the anthocyanin pathway or b) a synthetic gene in the late step of anthocyanin biosynthesis in *A. thaliana* [22].

The Col-0 ecotype produces pollen/sperm that is especially aggressive in favouring endosperm proliferation and repressing endosperm cellularisation, an effect that has been hypothesised to be due to differences in genomic imprinting of as yet uncharacterised loci in this ecotype [8, 18, 25]. Clearly, the Col-0 ecotype is highly sensitive to the effects of paternal excess and FBP mutations that affect the good rescue in ecotypes.

The main hypothesis that rescue of Col4x-induced seed lethality is affected by timely cellularisation of the endosperm [8] remains plausible and is supported by some of the data presented in this study. In most of the crosses studied for the *tt* mutants in the Col-0 ecotype, evidence of cellularisation was not found by 7 DAP. Thus, further research is required to clarify if and when cellularisation occurs in these crosses [8].

Overall, following interploidy crosses, seed survival is strongly affected by genetic ecotype in *A. thaliana* as well as getting influenced by the FBP; indeed, the L*er* ecotype has decreased expression of *TTG2* [8]. In addition, the outcomes showed that FBP mutants in the Col-0 ecotype crossed with Col4x had relatively low mature seed weights even though the seed cavity was much bigger than that in controls (Col2x × Col4x). The likely reason behind this apparent discrepancy is that the number of endosperm nuclei increased dramatically during seed development in these crosses. However, the low level of endosperm cellularisation led to a failure of endosperm to feed the growing embryo sufficiently in many seeds, and subsequently, these seeds collapsed, thus affecting the mean seed weight values. On the basis of the above discussion, further investigation is warranted to recognise the signalling molecule(s) that are crucial for endosperm cellularisation and factors influencing the movement of the cellularisation 'signal'. Moreover, a role for auxin should be considered because certain flavonols are known to be crucial for auxin

Table 1: Summary data for a range of FBP mutants crossed with Col4x in the Col-0 ecotype. All plants in column 1 are the maternal origin of the cross with paternal Col4x background. The mean weight of the mature seeds could be a reliable measure to indicate 'rescue' of Col4x-induced seed lethality by crosses involving maternally carried mutations in the FBP. Thus, the series of FBP mutant crosses comprehensive in this table are ordered by seed weight running from heaviest at the top.

Genotype	Seed development at 5 and 7 DAP								Mature seeds	
	Embryo stage		Embryo sac area (µm ^{2})		Chalazal endosperm area (µm ^{2})		Nodules number		Seed weight (µg)	%Plump and burst seed
	5 DAP	7 DAP	5 DAP	7 DAP	5 DAP	7 DAP	5 DAP	7 DAP		
Col 2x × Col2x (reference cross)	Heart	Torpedo	nd	nd	nd	nd	0	0	17± 3 (250)	nd
Col2x (Background ecotype)	Early heart	Overgrown globular retarded	40026	50771	2645	6312	0.8	0.5	14 ± 2 (517)	6 ± 1
tt4	Early heart	Overgrown globular retarded	34534	130296 ***	1716	14663 ***	1.2	0.8	25 ± 1(483) **	21 ±2 **
tt6	Heart	Heart	38077	103324 ***	994 *	4604	0.5	1.2	22 ± 1 (243) **	27 ±5 **
tt19/14	Globular	Overgrown globular retarded	23655 **	109010 **	873 *	6471	0.3	0.2	17 ± 2 (245)	20 ± 5
tt10	Globular	Overgrown globular retarded	38261	108284 ***	1662	11190	0.9	0.1 *	12 ± 2 (286)	7 ± 2
anl1	Globular	Globular	40931	80717 ***	764 **	52555	0.7	1.9 **	6 ± 1 (210) *	5 ±2

transport and because auxin is vital in regulating plant growth and seed growth [26]

3. Materials and Methods

3.1. Plant material

A. thaliana T-DNA (homozygous) insertion lines in the Col-0 ecotype are as follows: (*tt4-12*) GABI_304D03.02, (*tt6*) SALK_068963.53.50, (*tt14/tt19*) SALK_105779, (*anl1*) SALK_049338.56.00, and (*tt10*) GABI _146E10.02. T-DNA insertion lines were provided by the Nottingham Arabidopsis Stock Centre (NASC), UK. Columbia-0 (Col2x and Col4x) seeds were kindly provided by Prof. Rod Scott (University of Bath), UK.

3.2. Seed germination and plant growth

Seeds were immersed in 0.1% electrophoresis grade agarose (Invitrogen, UK) and incubated at 4 °C for 2–3 days. Seeds were germinated in trays that included Levingtons F2 + S (compost with sand; Scotts, UK). Trays (35 cm × 25 cm) were watered from the base with tap water accompanied by a surface area treatment with 0.2 g/L of insecticide (Intercept 70 WG; Scotts). Trays were in that case covered with a plastic cover and positioned in a Gallenkamp environment chamber under a 16 h/8 h light/dark cycle. Temperatures were 22 °C in the day and 18 °C at night, with 70% humidity. Plastic covers were removed after 1 week.

3.3. Crosses and controlled pollination

Emasculation and pollination were performed according to Scott *et al.* (1998) for developing and mature seeds [7]. The developing seeds were collected at 5 and 7 DAP to permit a study of confocal microscopy.

3.4. Image capture and treatment of homozygous t-DNA lines

Photos of the seeds were obtained utilising a Coolpix 4500 digital camera (Nikon). Images of dry seeds were captured using a Nikon SM2 1500 with a photonic PL2000 light source using NIS-Elements F2.30 software. Mean individual seed weight was calculated as follows.

$$\text{Mean individual seed weight} = \frac{Total\ weight - mean\ weight\ of\ weighing\ boat}{seed\ number}$$

On the basis of differentiating morphology and size of mature seeds, the seeds were classified into two classes predicated on their viability: a) 'plump and burst' seed phenotypes into the rescue category and b) 'shrivelled' seed phenotype into the lethal non-viable category.

3.5. Confocal laser scanning microscopy

The sample size in seed advancement at 5 and 7 DAP was between eight to ten seeds. The planning of specimens, including Feulgen staining, was performed as described by Braselton *et al.* [27], and images were taken with an argon-ion laser—488 nm excitation and 515-530 nm emission—by utilising a Nikon C1 confocal microscope system with a 90i Eclipse microscope and EZ-C1 software, 20x lens (Nikon UK). The images were saved as TIFF files after that prepared using Adobe Photoshop Elements (Adobe, USA). Maximum cross-sectional areas of the embryo sac and chalazal endosperm were measured as well as the number of nodules present in the central peripheral endosperm.

3.6. Statistical analysis

Data were analysed using non-parametric tests: the Kruskal–Wallis and then Mann–Whitney tests ($P < 0.05$ was set as significant) using the SPSS software package version 21 (IBM, USA).

4. Conclusions

This study showed that seed survival in 2x × 4x interploidy crosses is heavily influenced by the genetic background and by some maternal FBP mutations in *A. thaliana*. Further research should investigate the role of a putative signalling molecule in endosperm cellularisation and also whether auxin is a factor in endosperm cellularisation due to its role in regulating plant growth and seed growth. Future work will focus on the link between seed auxin and the FBP.

Author Contributions: All authors contributed to the study conception and design. Material preparation, data collection and analysis were performed by Maha Aljabri, James Doughty and Rod J. Scott. The first draft of the manuscript was written by Maha Aljabri and all authors commented on previous versions of the manuscript. All authors read and approved the final manuscript.

Funding: This research was funded by the Ministry of Higher Education of Saudi Arabia, and the Biotechnology and Biological Sciences Research Council [grant number BBD0012341].

Acknowledgments: I would like to sincerely thank Dr. Baoxiu Qi for academic and technical support. This research paper is a part of a PhD thesis.

Conflicts of Interest: The authors declare no conflict of interest.

References

[1] J. Doughty, M. Aljabri and R. J. Scott. Flavonoids and the regulation of seed size in Arabidopsis. *Biochem. Soc. Trans.* **2014**, 42, 364-369. 10.1042/BST20140040

[2] J. Li and F. Berger. Endosperm: food for humankind and fodder for scientific discoveries. *New Phytol*. **2012**, 195, 290-305. 10.1111/j.1469-8137.2012.04182.x

[3] M. Gehring, Y. Choi and R. L. Fischer. Imprinting and seed development. *Plant Cell*. **2004**, 16, S203- S213. DOI: https://doi.org/10.1105/tpc.017988

[4] S. Park and J. J. Harada, Arabidopsis embryogenesis. In Plant Embryogenesis. Springer Verlag, Humana Press, Totowa, **2008**, pp. 3-16.

[5] I. Debeaujon, K. M. Leon-Kloosterziel and M. Koornneef. Influence of the testa on seed dormancy, germination, and longevity in *Arabidopsis*. *Plant Physiol*. **2000**, 122, 403-414. https://doi.org/10.1104/pp.122.2.403

[6] D. Garcia, J. N. Fitz Gerald and F. Berger. Maternal control of integument cell elongation and zygotic control of endosperm growth are coordinated to determine seed size in Arabidopsis. *Plant Cell.* **2005**, 17, 52-60. 10.1105/tpc.104.027136

[7] R. J. Scott, M. Spielman, J. Bailey and H. G. Dickinson. Parent-of-origin effects on seed development in *Arabidopsis thaliana*. *Development.* **1998**, 125, 3329-3341.

[8] B. P. Dilkes, M. Spielman, R. Weizbauer, B. Watson, D. Burkart-Waco, R. J. Scott and L. Comai. The maternally expressed WRKY transcription factor TTG2 controls lethality in interploidy crosses of Arabidopsis. *PLoS Biol.* **2008**, 6, 2707-2720. https://doi.org/10.1371/journal.pbio.0060308

[9] R. J. Scott, J. Tratt and A. Bolbol. Seed development in interploidy hybrids. Polyploid and Hybrid Genomics: ed. / Z Jeffrey Chen; James A Birchler. Oxford, UK: Wiley, **2013**, pp. 271-290. http://dx.doi.org/10.1002/9781118552872.ch17

[10] T. Beeckman, R. De Rycke, R. Viane and D. Inze. Histological study of seed coat development in *Arabidopsis thaliana*. *J. Plant Res*. **2000**, 113, 139-148. 10.1007/PL00013924

[11] M. L. Falcone Ferreyra, S.P. Rius and P. Casati. Flavonoids: biosynthesis, biological functions, and biotechnological applications. *Front Plant Sci.* **2012**, 3, 222. 10.3389/fpls.2012.00222

[12] J. A. Moise, S. Han, L. Gudynaite-Savitch, D. A. Johnson, and B. L. A. Miki. Seed coats: Structure, development, composition, and biotechnology. *In Vitro Cell. Dev. Biol., Plant*. **2005**, 41, 5, 620-644. 10.1079/IVP2005686

[13] S. M. Nabavi, D. Samec, M. Tomczyk, L. Milella, D. Russo, S. Habtemariam, I. Suntar, L. Rastrelli, M. Daglia, J. Xiao and F. Giampieri. Flavonoid biosynthetic pathways in plants: Versatile targets for metabolic engineering. *Biotechnol adv.* **2018**, 38,107316. 10.1016/j.biotechadv.2018.11.005

[14] P. de S. Leonardo, K. Garbowicz, Y. Brotman, T. Tohge and R. F. Alisdair. The acetate pathway supports flavonoid and lipid biosynthesis in Arabidopsis. *Plant Physiol.* **2019**, 182, 857-869. 10.1104/pp.19.00683

[15] S. Yan, M. Xie, Y. Wang, Q. Xiao, N. Ding and Y. Li. Semi-synthesis of a series natural flavonoids and flavonoid glycosides from scutellarin. *Tetrahedron.* **2020**, 130950. *10.1016/j.tet.2020.130950*

[16] J. Zhu, Q. Xu, S. Zhao, X. Xia, X. Yan, Y. An, X. Mi, L. Guo, L. Samarina and C. Wei. Comprehensive co-expression analysis provides novel insights into temporal variation of flavonoids in fresh leaves of the tea plant (*Camellia sinensis*). Plant Sci. **2020**, 290, 110306. 10.1016/j.plantsci.2019.110306

[17] C. Bushell, M. Spielman and R. J. Scott. The Basis of Natural and Artificial Postzygotic Hybridization Barriers in *Arabidopsis* Species. *Plant Cell*. **2003**. 15, 1430-1442. https://doi.org/10.1105/tpc.010496

[18] C. Kohler, O. Mittelsten Scheid and A. Erilova. The impact of the triploid block on the origin and evolution of polyploid plants. *Trends Genet.* **2010**, 26, 142-148. 10.1016/j.tig.2009.12.006

[19] M. Aljabri. Maternal control of seed development mediated by the flavonoid biosynthesis pathway, **2016**, PhD thesis. University of Bath, UK.

[20] I. Debeaujon, N. Nesi, P. Perez, M. Devic, O. Grandjean, M. Caboche and L. Lepiniec. Proanthocyanidin-accumulating cells in Arabidopsis testa: regulation of differentiation and role in seed development. *Plant Cell*. **2003**, 15, 2514-2531. https://doi.org/10.1105/tpc.014043

[21] I. R. Baxter, J. C. Young, G. Armstrong, N. Foster, N. Bogenschutz, T. Cordova, W. A. Peer, S. P. Hazen, A. S. Murphy and J. F. Harper. A plasma membrane H+-ATPase is required for the formation of proanthocyanidins in the seed coat endothelium of *Arabidopsis thaliana*. *Proc Natl Acad Sci USA.* **2005**, 102, 2649-2654. 10.1073/pnas.0406377102

[22] H. Kubo, N. Nawa and S. A. Lupsea. Anthocyaninless1 gene of *Arabidopsis thaliana* encodes a UDP-glucose: flavonoid-3-O-glucosyltransferase. *J Plant Res.* **2007**, 120, 445-449. 10.1007/s10265-006-0067-7

[23] L. C. David, J. Dechorgnat, P. Berquin, J. M. Routaboul, I. Debeaujon, F. Daniel-Vedele and S. Ferrario-Mery. Proanthocyanidin oxidation of Arabidopsis seeds is altered in mutant of the high-affinity nitrate transporter NRT2.7. *J. Exp. Bot*. **2014**, 65, 885-893. 10.1093/jxb/ert481

[24] J. Zhao and R. A. Dixon. The 'ins' and 'outs' of flavonoid transport. Trends Plant Sci. **2010**, 15: 72-80. 10.1016/j.tplants.2009.11.006

[25] [25] A. A. Bolbol. Genetic analysis of postzygotic hybridisation barriers in *Arabidopsis thaliana*. **2010**, PhD thesis. University of Bath, UK.

[26] A. Locascio, I. Roig-Villanova, J. Bernardi and S. Varotto. Current perspectives on the hormonal control of seed development in Arabidopsis and maize: a focus on auxin. *Front Plant Sci.* **2014**, 5, 412. 10.3389/fpls.2014.00412

[27] J. P. Braselton, M. J. Wilkinson and S. A. Clulow. Feulgen staining of intact plant tissues for confocal microscopy. Biotech. Histochem. 1996, 71, 84-87. 10.3109/10520299609117139

Journal of Umm Al-Qura University
for Applied Science

journal homepage: https://uqu.edu.sa/en/jas/87823

The Vibration of a Viscothermoelastic Gold Nanobeam Induced by Different Types of Thermal Loading

Eman A. N. Al-Lehaibi [a].

[a] *Mathematics Department, Al-Lith University College, Umm Al-Qura University, Al-Lith, Saudi Arabia Arabia.*

A R T I C L E I N F O

Article History:
Submission date: 11/10/2019
Accepted date: 12/4/2020

Keywords:
Vibration; Viscothermoelastic, Golden Nanobeam, Golden, Ramp-type heat, Harmonic heat, Fourier law.

A B S T R A C T

In the present work, the numerical solutions have been carried out for viscothermoelastic homogeneous isotropic nanobeam. A generalized model of one relaxation time has been used, under simply supported conditions for fixed aspect ratios. Laplace transform has been applied for the governing equations. The inverse of the Laplace transform has been calculated by applying the Tzou method. The numerical results have been validated for a viscothermoelastic rectangular nanobeam of gold as a particular case when it is subjected to ramp-type and harmonic-type heating. The numerical results have been illustrated in figures to stand on the impact of the viscothermoelastic parameters, the ramping heat parameter, and the harmonic heat parameter on all the studied functions. The viscothermoelastic parameters, the ramping heat parameter, and the harmonic heat parameter have significant effects on the temperature increment, the lateral vibration, the deformation, the stress, and the stress-strain energy distributions.

1. Introduction

Tzou constructed and studied the heat conduction by using different mathematical models such as dual-phase lag (DPL) [1,2]. The temperature gradient and heat flux have been considered through this model. Many authors have used this model to solve heat transfer problems [3-8]. The coupled theory of thermoelasticity is the kind of heat conduction based on the equation of motion, and the equation of energy conservation, depending on Fourier's law of heat conduction [9-12]. Lord and Shulman modified the classical Fourier's law of heat conduction by inserting the lag time (relaxation time) for an isotropic case [13]. Within this model, the heat conduction law has been modified to include the heat flux as an unknown function with its time derivative, which is called Cattaneo's law (non-Fourier) of heat conduction. The heat equation is a hyperbolic type in this theory, which eliminates the defect of infinite speed propagation of the thermal wave [14]. Many mathematical models and applications based on micro and nano-electromechanical beam resonators have been solved and discussed in [15-18].

The vibration of nanobeam is the most important and essential of the micro/nanobeam resonators. Alghamdi [9] studied the thermal damping of vibration of beam resonator with voids by dual-phase-lag generalized thermoelasticity theory. Youssef and Elsibai solved a problem of gold nanobeam by using state-space approach [19]. Youssef solved a problem of gold nanobeam with variable thermal conductivity by using the state-space approach [20]. Sharma and Grover discussed the thermal transfer and vibrations of an isotropic homogenous and thermoelastic micro/nanoscale thin beam resonators with voids [21]. Sun and Saka discussed the thermal damping vibration for microplate out-of-plane circular plate resonators [22]. They added a new factor based on Poisson's ratio in the formula of thermoelastic damping which is different from the Lifshitz and Roukes formula [23]. Some authors discussed the vibration and the heat transfer process of thermoelastic nanobeams [24-28]. Eman and Youssef studied the vibration of gold nanobeam due to thermal shock [25]. Kiawa studied the effects of internal and external damping on transverse vibrations of a nanobeam due to a moving heat source by using the Green function properties [27]. Boley discussed the vibrations of a simply supported rectangular nanobeam subjected to a thermal shock distributed through its span [26]. A discussion of the thermally induced vibration of nano-beams structures has been done by Manolis and Beskos; they used a numerical method of analysis to the thermal of the elastic dynamic response of beam structure to thermal loading [28]. Al-Huniti et al. introduced an investigation of the thermally induced displacements and stresses of a heated rod by a high-power moving laser beam, and he studied the dynamical beheviour of the heated rod using the Laplace transforms technique [24].

Recently, the study of the viscoelastic materials and its relaxation times effects has become essential and vital in thermomechanics. The viscothermoelasticity theory and its variational principles in thermodynamics has been studied by Biot [29,30]. Drozdov [31] derived the constitutive model for the viscothermoelasticity behavior of polymer materials at finite strain. At the same time, Ezzat and El-Karmany [32] applied a new model of viscothermoelasticity for isotropic media to study the lag times impact of volume properties of viscothermoelasticity materials. Carcione et al. applied a new algorithm for wave simulations in an elastic medium by using the Kelvin–Voigt mechanical model [33]. Grover studied transverse vibrations in micro-scale viscothermoelastic beam resonators [34-36]. Sharma and Grover discussed the closed-form definition for the transverse vibrations of a homogenous thermoelastic fine beam with voids in micro/nanoscale [21]. Grover and Seth [37] studied viscothermoelastic micro-beam resonators based on the dual-phase-lag model.

2. Basic Equations

We assume an isotropic homogenous thermally conducting, Kelvin–Voigt type viscothermoelastic solid material in the Cartesian coordinate system. Initially, it is considered unstained and at the reference temperature T_0 everywhere. The essential governing partial differential equations of the motion and heat conduction have been assumed in the context of generalized thermoelasticity.

The displacement components $U(x,y,z;t)=(u,v,w)$ and absolute temperature $T(x,y,z;t)$, without body forces and heat sources, are given by [36]:

$$\sigma_{ij,j}=\rho\ddot{u}_i \tag{1}$$

* **Corresponding Author**
Mathematics Department, Al-Lith University College, Umm Al-Qura University, Al-Lith, Saudi Arabia.
E-mail address: ealehaibi@uqu.edu.sa

$$\sigma_{ij} = \lambda\delta_{ij}e_{kk} + 2\mu e_{ij} - \beta\delta_{ij}\left(T - T_0\right) \tag{2}$$

$$KT_{,ii} = \left(\frac{\partial}{\partial t} + \tau_0\frac{\partial^2}{\partial t^2}\right)\left(\rho C_\upsilon T + \beta T_0\delta_{ij}e_{ij}\right) \tag{3}$$

$$e_{ij} = \frac{1}{2}\left(u_{i,j} + u_{j,i}\right) \tag{4}$$

where $i, j = x, y, z$, ρ is the density, α_T is the coefficient of linear thermal expansion, λ, μ Lamè's parameter, K is the thermal conductivity, τ_0 is the thermal relaxation time, and C_υ is the specific heat at constant strain.

For viscothermoelastic materials, Lamè's parameters have been considered in the form:

$$\lambda = \lambda_0\left(1 + \lambda_1\frac{\partial}{\partial t}\right),\ \mu = \mu_0\left(1 + \mu_1\frac{\partial}{\partial t}\right),\ \beta = \left(3\lambda + 2\mu\right)\alpha_T \tag{5}$$

where λ_1, μ_1 are the viscoelastic relaxation times and λ_0, μ_0 Lamè's parameter in the usual case.

3. Formulation of the problem

A small flexural deflection of a thin viscothermoelastic nanobeam of length ℓ, width b, and thickness h has been considered. The x, y, and z-axes are defined along the longitudinal $\left(0 \le x \le \ell\right)$, width $\left(-b/2 \le y \le b/2\right)$, thickness $\left(-h/2 \le z \le h/2\right)$, and directions of the beam, respectively.

In a state of equilibrium, the beam is undeformed, unstressed, without a damping mechanism, and the temperature is T_0 everywhere [6].

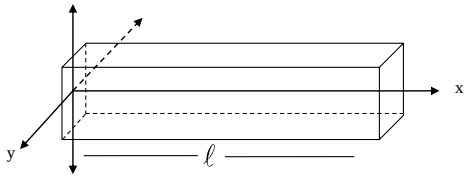

Figure 1: The rectangular beam in the Cartesian coordinate system

The usual Euler–Bernoulli assumption [34] has been considered, then, the cross-section of any plane, initially perpendicular to the x-axis remains plane and perpendicular to the x-axis during bending. Therefore, the displacements are given by:

$$u = -z\frac{\partial w(x,t)}{\partial x},\ v = 0\ ,\ w(x,y,z,t) = w(x,t) \tag{6}$$

Where $w(x,t)$ is the lateral deflection.

The flexural moment of the cross-section is given by

$$M(x,t) + \rho A\frac{\partial^2 w(x,t)}{\partial t^2} = 0 \tag{7}$$

where $M_T(x,t)$ is defined as the thermal moment of the beam and is given by:

$$M_T(x,t) = b\int_{-h/2}^{h/2}\theta(x,z,t)\,z\,dz \tag{8}$$

and $M(x,t)$ is given by:

$$M(x,t) = -b\int_{-h/2}^{h/2}\sigma_{xx}(x,t,z)\,z\,dz = \left(\lambda + 2\mu\right)I\frac{\partial^2 w(x,t)}{\partial x^2} + \beta M_T(x,t) \tag{9}$$

Where I is the moment of inertia of the cross-section about the x-axis and is given by $I = \left(bh^3/12\right)$ Hence, the differential equation of thermally induced lateral vibration of the beam may be expressed in the form [34]:

$$\left(\lambda + 2\mu\right)I\frac{\partial^4 w(x,t)}{\partial x^4} + \rho A\frac{\partial^2 w(x,t)}{\partial t^2} + \beta\frac{\partial^2 M_T(x,t)}{\partial x^2} = 0 \tag{10}$$

where the area of the beam cross-section is $A = (hb)$ and $\theta(x,z,t) = \left(T(x,z,t) - T_0\right)$ is the temperature increment of the beam.

The non-Fourier heat conduction equation has the following form [34]:

$$\left(\frac{\partial^2}{\partial x^2} + \frac{\partial^2}{\partial z^2}\right)\theta(x,z,t) = \left(\frac{\partial}{\partial t} + \tau_o\frac{\partial^2}{\partial t^2}\right)\left(\frac{\rho C_\upsilon}{k}\theta(x,z,t) + \frac{(3\lambda + 2\mu)\alpha_T T_0}{k}e(x,z,t)\right) \tag{11}$$

where $e(x,z,t)$ is the volumetric strain which is given by:

$$e(x,z,t) = \frac{\partial u}{\partial x} + \frac{\partial v}{\partial y} + \frac{\partial w}{\partial z} \tag{12}$$

By using the forms in [6], we obtain that:

$$e(x,z,t) = -z\frac{\partial^2 w(x,t)}{\partial x^2} \tag{13}$$

From the relations in [5], we have the following:

$$\lambda + 2\mu = \left(\lambda_0 + 2\mu_0\right)\left(1 + \beta_1\frac{\partial}{\partial t}\right),\ \left(3\lambda + 2\mu\right) = \left(3\lambda_0 + 2\mu_0\right)\left(1 + \beta_2\frac{\partial}{\partial t}\right) \tag{14}$$

where $\beta_1 = \frac{(\lambda_0\lambda_1 + 2\mu_0\mu_1)}{(\lambda_0 + 2\mu_0)}$, $\beta_2 = \frac{(3\lambda_0\lambda_1 + 2\mu_0\mu_1)}{(3\lambda_0 + 2\mu_0)}$ are called the aggregation of the viscoelastic relaxation times parameters.

Because there is no heat source or heat flow across the upper and lower surfaces of the beam, $\frac{\partial}{\partial z}\theta\left(x, \pm\frac{h}{2}, t\right) = 0$. Hence, For a very long and skinny beam, the temperature increment varies in terms of a $\sin(pz)$ function along the thickness direction, gives [38]:

$$\theta(x,z,t) = \vartheta(x,t)\sin(pz) \tag{15}$$

where $p = \pi/h$.

Hence, equations [8], [10], and [15] gives:

$$\left(\lambda_0 + 2\mu_0\right)\left(1 + \beta_1\frac{\partial}{\partial t}\right)\frac{\partial^4 w(x,t)}{\partial x^4} + \frac{12\rho}{h^2}\frac{\partial^2 w(x,t)}{\partial t^2} + \frac{12(3\lambda_0 + 2\mu_0)\alpha_T}{h^3}\left(1 + \beta_2\frac{\partial}{\partial t}\right)\frac{\partial^2\vartheta(x,t)}{\partial x^2}\int_{-h/2}^{h/2} z\sin(pz)\,dz = 0 \tag{16}$$

and equation [11] gives

$$\left(\frac{\partial^2}{\partial x^2} - p^2\right)\vartheta(x,t)\sin(pz) = \left(\frac{\partial}{\partial t} + \tau_o\frac{\partial^2}{\partial t^2}\right)\left(\frac{\rho C_\upsilon}{k}\vartheta(x,t)\sin(pz) - \frac{(3\lambda_0 + 2\mu_0)\alpha_T T_0}{k}\left(1 + \beta_2\frac{\partial}{\partial t}\right)z\frac{\partial^2 w(x,t)}{\partial x^2}\right) \tag{17}$$

By doing the integrations, the equation [16] takes the form

$$\left(\lambda_0 + 2\mu_0\right)\left(1 + \beta_1\frac{\partial}{\partial t}\right)\frac{\partial^4 w(x,t)}{\partial x^4} + \frac{12\rho}{h^2}\frac{\partial^2 w(x,t)}{\partial t^2} + \frac{24(3\lambda_0 + 2\mu_0)\alpha_T}{h\pi^2}\left(1 + \beta_2\frac{\partial}{\partial t}\right)\frac{\partial^2\vartheta(x,t)}{\partial x^2} = 0 \tag{18}$$

In the equation [17], we multiply both sides by "z" and integrating concerning "z" from $-h/2$ to $h/2$, then we obtain

$$\left(\frac{\partial^2}{\partial x^2} - p^2\right)\vartheta(x,t) = \left(\frac{\partial}{\partial t} + \tau_0\frac{\partial^2}{\partial t^2}\right)\left(\varepsilon\vartheta(x,t) - \frac{T_0 h\pi^2(3\lambda_0 + 2\mu_0)\alpha_T}{24k}\left(1 + \beta_2\frac{\partial}{\partial t}\right)\frac{\partial^2 w(x,t)}{\partial x^2}\right) \tag{19}$$

Where $\varepsilon = \frac{\rho C_\upsilon}{k}$.

For simplicity, we will use the following dimensionless variables [19]:

$$\left(x', w', h', \ell'\right) = \varepsilon c_0\left(x, w, h, \ell\right),\ \left(t', \tau_0', \beta_1', \beta_2'\right) = \varepsilon c_0^2\left(t, \tau_0, \beta_1, \beta_2\right),\ \sigma' = \frac{\sigma}{\lambda_0 + 2\mu_0},\ \vartheta' = \frac{\vartheta}{T_0} \tag{20}$$

where $c_0^2 = \frac{\lambda_0 + 2\mu_0}{\rho}$.

Thus, we get

$$\left(1 + \beta_1\frac{\partial}{\partial t}\right)\frac{\partial^4 w(x,t)}{\partial x^4} + \varepsilon_1\frac{\partial^2 w(x,t)}{\partial t^2} = -\varepsilon_2\left(1 + \beta_2\frac{\partial}{\partial t}\right)\frac{\partial^2\vartheta(x,t)}{\partial x^2} \tag{21}$$

and

$$\left[\left(\frac{\partial^2}{\partial x^2}-\varepsilon_3\right)-\left(\frac{\partial}{\partial t}+\tau_o\frac{\partial^2}{\partial t^2}\right)\right]\vartheta(x,t)=-\varepsilon_4\left(1+\beta_2\frac{\partial}{\partial t}\right)\frac{\partial^2 w(x,t)}{\partial x^2} \quad (22)$$

$$\sigma_{xx}(x,z,t)=\left(1+\beta_1\frac{\partial}{\partial t}\right)e(x,,z,t)-\gamma\left(1+\beta_2\frac{\partial}{\partial t}\right)\vartheta(x,t)\sin(pz) \quad (23)$$

where

$\varepsilon_1=\frac{12}{h^2}$, $\varepsilon_2=\frac{24\gamma}{\pi^2 h}$, $\varepsilon_3=p^2$, $\varepsilon_4=\frac{\pi^2 h(3\lambda_0+2\mu_0)\alpha_T}{24k\varepsilon}$, $\gamma=\frac{(3\lambda_0+2\mu_0)\alpha_T T_0}{(\lambda_0+2\mu_0)}$.

(The primes have been dropped for convenience)

3.1. The formulation in the Laplace transform domain

We will apply the Laplace transform for equations [21] and [22], which is defined by:

$$\bar{f}(s)=\int_0^\infty f(t)e^{-st}\,dt \quad (24)$$

Hence, we obtain the following system of ordinary differential equations:

$$(1+\beta_1 s)\frac{d^4\bar{w}}{dx^4}+\varepsilon_1 s^2\bar{w}(x,s)=-\varepsilon_2(1+\beta_2 s)\frac{d^2\bar{\vartheta}}{dx^2} \quad (25)$$

$$\left(\frac{\partial^2}{\partial x^2}-\varepsilon_3-\left(s+\tau_o s^2\right)\right)\bar{\vartheta}=-\varepsilon_4\left(s+\tau_o s^2\right)(1+\beta_2 s)\frac{d^2\bar{w}}{dx^2} \quad (26)$$

$$\bar{\sigma}_{xx}=(1+\beta_1 s)\bar{e}-\gamma(1+\beta_2 s)\bar{\vartheta}\sin(pz) \quad (27)$$

$$\bar{e}=-z\frac{d^2\bar{w}}{dx^2} \quad (28)$$

Within applying the Laplace transform, we used the following initial conditions:

$$\vartheta(x,0)=w(x,0)=\frac{\partial\vartheta(x,0)}{\partial t}=\frac{\partial w(x,0)}{\partial t}=0 \quad (29)$$

We can re-write the above system to be in the forms:

$$\left(D^4+\varepsilon_5\right)\bar{w}=-\varepsilon_6 D^2\bar{\vartheta} \quad (30)$$

and

$$\left(D^2-\varepsilon_7\right)\bar{\vartheta}=-\varepsilon_8 D^2\bar{w} \quad (31)$$

where $D^r=\frac{d^r}{dx^r}$, $\varepsilon_5=\frac{\varepsilon_1 s^2}{(1+\beta_1 s)}$, $\varepsilon_6=\frac{\varepsilon_2(1+\beta_2 s)}{(1+\beta_1 s)}$,

$\varepsilon_7=\varepsilon_3+\left(s+\tau_o s^2\right)$, $\varepsilon_8=\varepsilon_4\left(s+\tau_o s^2\right)(1+\beta_2 s)$.

Eliminating $\bar{w}$ between the equations of the above system, then, we get

$$\left[D^6-LD^4+MD^2-N\right]\bar{\vartheta}=0 \quad (32)$$

Similarly, eliminating $\bar{\vartheta}$ gives:

$$\left[D^6-LD^4+MD^2-N\right]\bar{w}=0 \quad (33)$$

where $L=\varepsilon_7+\varepsilon_6\varepsilon_8$, $M=\varepsilon_5$, $N=\varepsilon_5\varepsilon_7$.

The solutions of the equations [32] and [33] take the forms:

$$\bar{\vartheta}(x,s)=-\varepsilon_8\sum_{i=1}^{3}c_i k_i^2\sinh\left(k_i(\ell-x)\right) \quad (34)$$

and

$$\bar{w}(x,s)=\sum_{i=1}^{3}c_i\left(k_i^2-\varepsilon_7\right)\sinh\left(k_i(\ell-x)\right) \quad (35)$$

Where the parameters $\pm k_1,\pm k_2,\pm k_3$ are the roots of the following characteristic equation:

$$k^6-Lk^4+Mk^2-N=0 \quad (36)$$

To calculate the constants $c_i=c_i(s)$, $i=1,2,3$, we must apply any set of boundary conditions, so we consider that the beam is thermally loaded and simply supported as following:

$$w(0,t)=\left.\frac{\partial^2 w(x,t)}{\partial x^2}\right|_{x=0}=0,\ \vartheta(0,t)=\vartheta_0 g(t) \quad (37)$$

and

$$w(\ell,t)=\left.\frac{\partial^2 w(x,t)}{\partial x^2}\right|_{x=\ell}=\vartheta(\ell,t)=0 \quad (38)$$

Where ϑ_0 is constant.

Apply the Laplace transform, we have:

$$\bar{w}(0,s)=\frac{\partial^2\bar{w}(0,s)}{\partial x^2}=0,\ \ \bar{\vartheta}(0,s)=\vartheta_0\bar{g}(s) \quad (39)$$

and

$$\bar{w}(\ell,s)=\frac{\partial^2\bar{w}(\ell,s)}{\partial x^2}=\bar{\vartheta}(\ell,s)=0 \quad (40)$$

Then, we obtain the following system of linear equations:

$$\sum_{i=1}^{3}c_i k_i^2\sinh\left(k_i\ell\right)=-\frac{\vartheta_0\bar{g}(s)}{\varepsilon_8} \quad (41)$$

$$\sum_{i=1}^{3}c_i\left(k_i^2-\varepsilon_7\right)\sinh\left(k_i\ell\right)=0 \quad (42)$$

and

$$\sum_{i=1}^{3}c_i\left(k_i^2-\varepsilon_7\right)k_i^2\sinh\left(k_i\ell\right)=0 \quad (43)$$

After solving the above system, then, we get the solutions in the Laplace transform domain as follows:

$$\theta(x,s)=\frac{\vartheta_0\bar{g}(s)\sin(pz)}{\varepsilon_7}\left[\begin{array}{l}\frac{(\varepsilon_7-k_2^2)(\varepsilon_7-k_3^2)k_1^2}{(k_1^2-k_2^2)(k_1^2-k_3^2)\sinh(k_1\ell)}\sinh\left(k_1(\ell-x)\right)+\\ \frac{(\varepsilon_7-k_1^2)(\varepsilon_7-k_3^2)k_2^2}{(k_2^2-k_1^2)(k_2^2-k_3^2)\sinh(k_2\ell)}\sinh\left(k_2(\ell-x)\right)+\\ \frac{(\varepsilon_7-k_1^2)(\varepsilon_7-k_2^2)k_3^2}{(k_3^2-k_1^2)(k_3^2-k_2^2)\sinh(k_3\ell)}\sinh\left(k_3(\ell-x)\right)\end{array}\right] \quad (44)$$

$$\bar{w}(x,s)=-\frac{\vartheta_0\bar{g}(s)(\varepsilon_7-k_1^2)(\varepsilon_7-k_2^2)(\varepsilon_7-k_3^2)}{\varepsilon_7\varepsilon_8}\left[\begin{array}{l}\frac{1}{(k_1^2-k_2^2)(k_1^2-k_3^2)\sinh(k_1\ell)}\sinh\left(k_1(\ell-x)\right)+\\ \frac{1}{(k_2^2-k_1^2)(k_2^2-k_3^2)\sinh(k_2\ell)}\sinh\left(k_2(\ell-x)\right)+\\ \frac{1}{(k_3^2-k_1^2)(k_3^2-k_2^2)\sinh(k_3\ell)}\sinh\left(k_3(\ell-x)\right)\end{array}\right] \quad (45)$$

and

$$\bar{e}(x,s)=\frac{z\vartheta_0\bar{g}(s)(\varepsilon_7-k_1^2)(\varepsilon_7-k_2^2)(\varepsilon_7-k_3^2)}{\varepsilon_7\varepsilon_8}\left[\begin{array}{l}\frac{k_1^2}{(k_1^2-k_2^2)(k_1^2-k_3^2)\sinh(k_1\ell)}\sinh\left(k_1(\ell-x)\right)+\\ \frac{k_2^2}{(k_2^2-k_1^2)(k_2^2-k_3^2)\sinh(k_2\ell)}\sinh\left(k_2(\ell-x)\right)+\\ \frac{k_3^2}{(k_3^2-k_1^2)(k_3^2-k_2^2)\sinh(k_3\ell)}\sinh\left(k_3(\ell-x)\right)\end{array}\right] \quad (46)$$

3.2. The Stress and the Strain-Energy

The stress-strain energy through the beam is calculated by [39]:

$$\varpi(x,z,t)=\sum_{i,j=1}^{3}\frac{1}{2}\sigma_{ij}e_{ij}=\frac{1}{2}\sigma_{xx}(x,z,t)e(x,z,t) \quad (47)$$

Hence, we have:

$$\varpi(x,z,t)=\frac{1}{2}\left[L^{-1}\left(\bar{\sigma}_{xx}(x,z,s)\right)\right]\left[L^{-1}\left(\bar{e}(x,z,s)\right)\right] \quad (48)$$

where $L^{-1}[\bullet]$ gives the inversion of Laplace transform.

4. Numerical Inversion of the Laplace Transform

Before we go on the numerical solutions of the problem, we must determine the function of the thermal loading $g(t)$. We consider that the thermal loading will take two different types as follows:

1- Ramp-type heating

$$g(t)=\begin{Bmatrix} 0 & t<0 \\ \dfrac{t}{t_0} & 0<t<t_0 \\ 1 & t\geq t_0 \end{Bmatrix} \tag{49}$$

Where t_0 is called the ramping time parameter

Applying Laplace transform defined in [24], then, we have

$$\bar{g}(s)=\frac{1-e^{-st_0}}{s^2 t_0} \tag{50}$$

2- Harmonic-type heating

$$g(t)=\sin(\omega t) \tag{51}$$

where ω is called the angular thermal moment parameter

By using Laplace transform defined in [24], we get

$$\bar{g}(s)=\frac{\omega}{s^2+\omega^2} \tag{51}$$

The approximation method of Riemann-sum has been used to obtain numerical results. Within this method, any function in the Laplace domain can be inverted to the time-domain as:

$$f(t)=\frac{e^{\kappa t}}{t}\left[\frac{1}{2}\bar{f}(\kappa)+\mathrm{Re}\sum_{n=1}^{N}(-1)^n\bar{f}\left(\kappa+\frac{in\pi}{t}\right)\right] \tag{52}$$

where Re is the real part and i is an imaginary number unit. For faster convergence, numerous numerical experiments have shown that the value of κ satisfies the relation $\kappa t\approx 4.7$ Tzou [2].

5. Numerical Results and Discussion

Now, we will consider a numerical example for which computational results are given. For this purpose, The gold (Au) has been taken as the thermoelastic material for which we take the following values of the different physical constants[39]:

$k=318\ \mathrm{W/(mK)}$, $\alpha_T=14.2(10)^{-6}\ \mathrm{K^{-1}}$,

$\rho=1930\ \mathrm{kg/m^3}$, $T_0=293\mathrm{K}$,

$C_\upsilon=130\ \mathrm{J/(kgK)}$, $\lambda_0=458.33\times10^9\ \mathrm{N/m^2}$,

$\mu_0=62.5\times10^9\ \mathrm{N/m^2}$, $\tau_0=4.32\times10^{-13}\mathrm{s}$,

$\lambda_1=\mu_1=6.89\times10^{-13}\mathrm{s}$.

The aspect ratios of the beam are fixed as $\ell/h=5$ and $b=h/2$. For the nanoscale beam, we will take the range of the beam length $\ell\ (1-100)\times10^{-12}\mathrm{m}$ —the original time t and the relaxation time τ_0 of order 10^{-12} sec and 10^{-14} sec, respectively.

The figures were prepared by using the non-dimensional variables for beam length $\ell=1.0$, $\theta_0=1.0$ $z=h/4$ and $t=1.0$.

Figures 2-6 represent the temperature increment, the lateral vibration, the deformation, the stress, and the stress-strain energy distributions, respectively, for the thermoelastic case and the viscothermoelastic case. It has been noted that the temperature increment almost is the same for the two cases, while the effects of the viscothermoelastic parameters are significant on the lateral vibration, the deformation, the stress, and the stress-strain energy distributions. The peak points of the lateral vibration, deformation, stress, and stress-strain energy distributions are raised in the case of viscothermoelasticity.

Figures 7-11 represent the temperature increment, the lateral vibration, the deformation, the stress, and the stress-strain energy distributions, respectively, with variance values of ramping time parameter $t_0=(0.5,1.0,1.5)$ and the viscothermoelastic case. It has been noted that the temperature increment in the two cases $t_0=0.5$ and $t_0=1.0$ are almost the same, while it is different in the case $t_0=1.5$. The values of the temperature increment, the lateral vibration, the deformation, the stress, and the stress-strain energy decrease when the value of the ramping time parameter increases. The values of the beak points of the lateral vibration, the deformation, the stress, and the stress-strain energy increase when the value of the ramping time parameter decreases.

Figures 12-16 represent the temperature increment, the lateral vibration, the deformation, the stress, and the stress-strain energy distributions, respectively, for variance values of the angular thermal moment parameter $\omega=(\pi/6,\pi/3,\pi/2)$ to stand on the effect of this parameter on all the studied functions. It has been noted that the effect of the angular thermal moment parameter is significant in all the studied functions. When the value of the angular thermal moment parameter increases, the values of the temperature increment, the lateral vibration, the deformation, the stress, and the stress-strain energy distributions increase.

6. Conclusion

In this work, a simply supported viscothermoelastic nanobeam has been thermally loaded by ram-type and harmonic-type heating. The viscothermoelastic parameters, ramping time parameter, and angular thermal moment parameter have significant effects on the temperature increment, the lateral vibration, the deformation, the stress, and the stress-strain energy distributions.

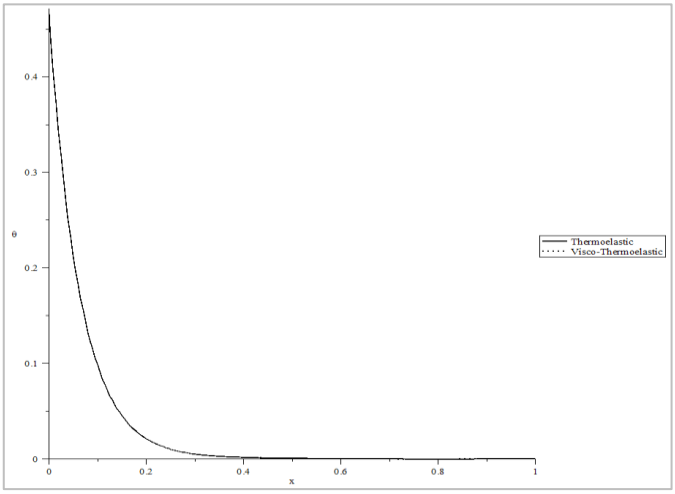

Figure 2: The temperature increment distribution for different models

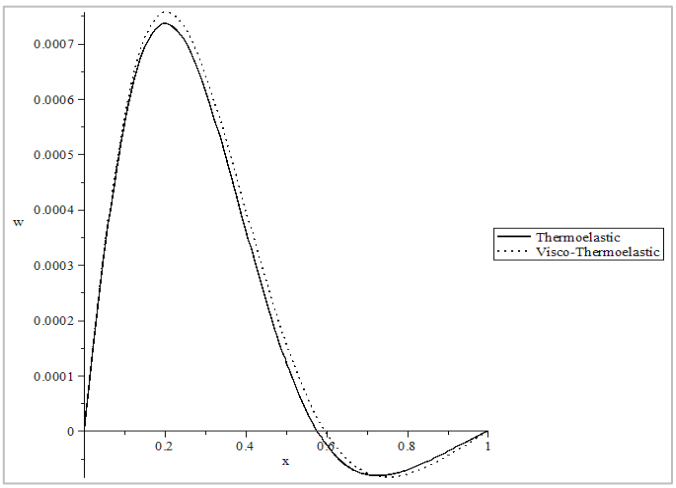

Figure 3: The lateral vibration distribution for different models

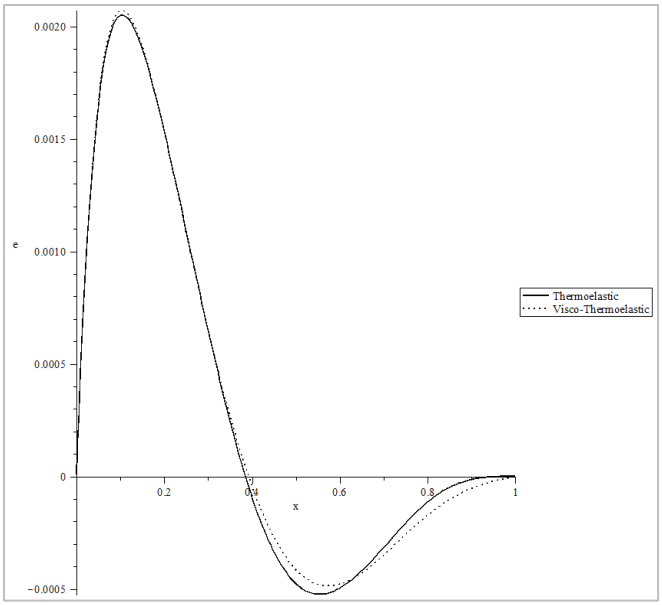

Figure 4: The deformation distribution for different models

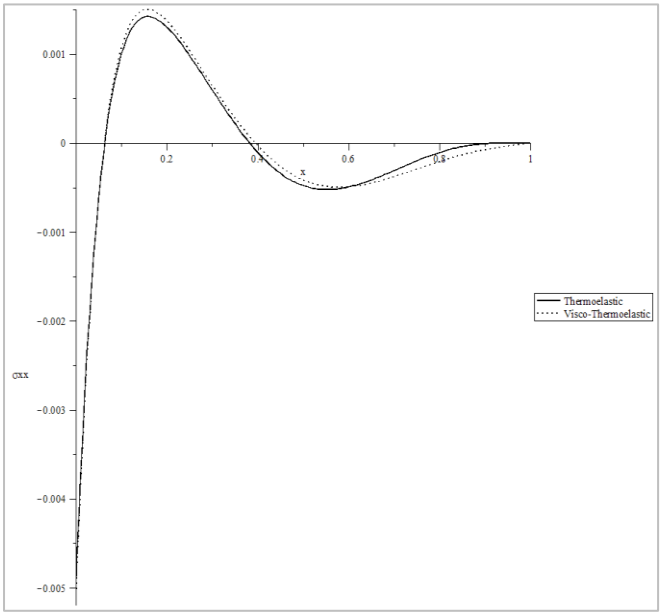

Figure 5: The stress distribution for different models

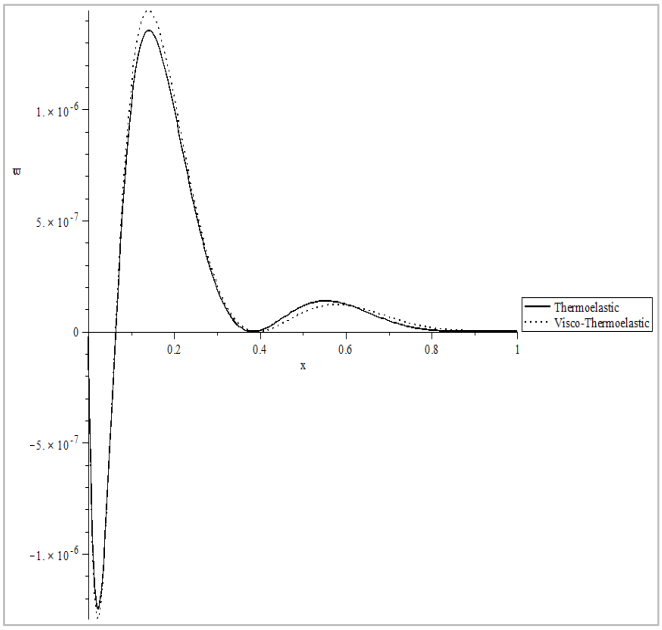

Figure 6: The strain-energy distribution for different models

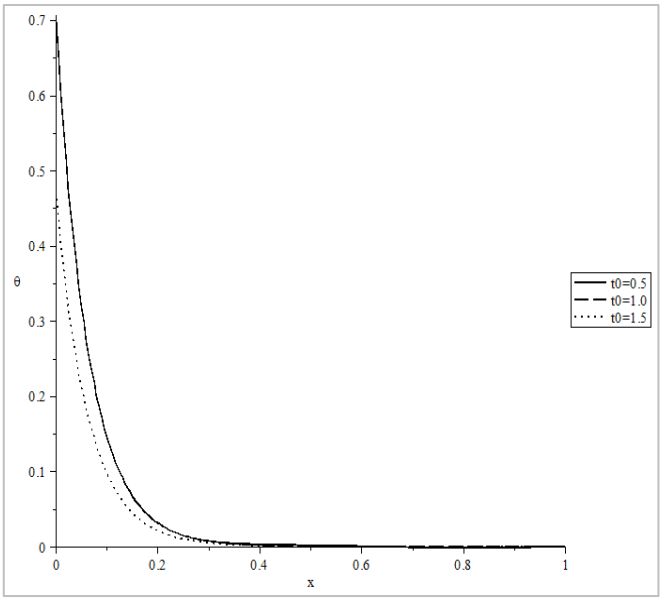

Figure 7: The temperature increments distribution with variance values of ramping time parameter

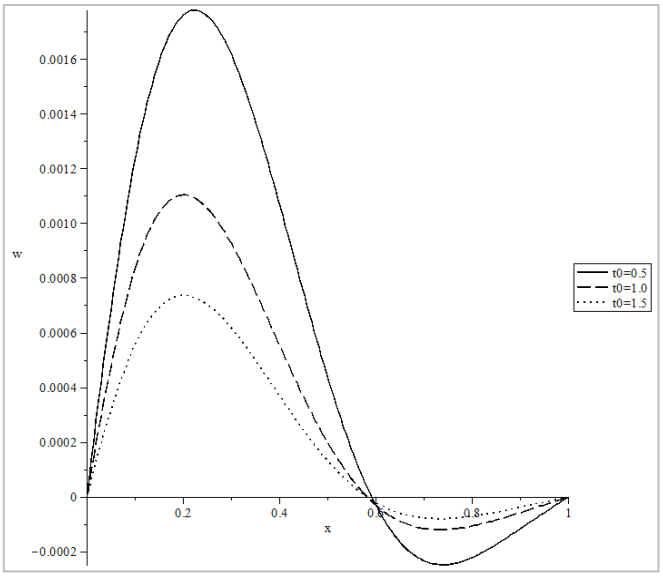

Figure 8: The lateral deflection distribution with variance values of ramping time parameter

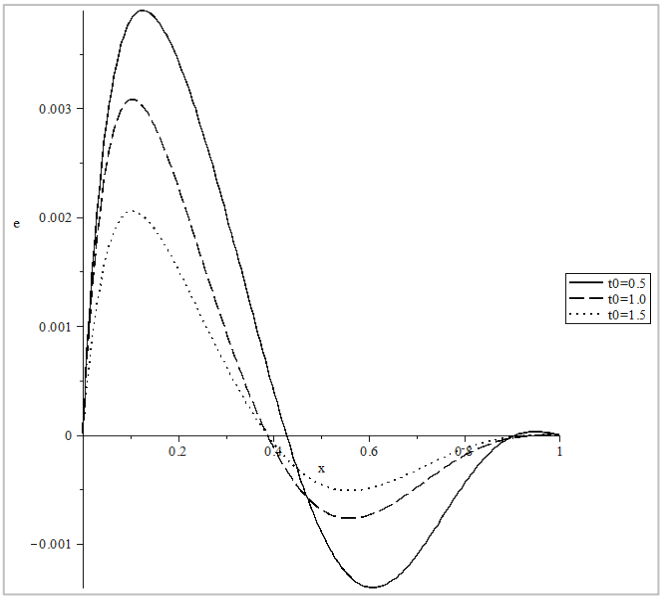

Figure 9: The deformation distribution with variance values of ramping time parameter

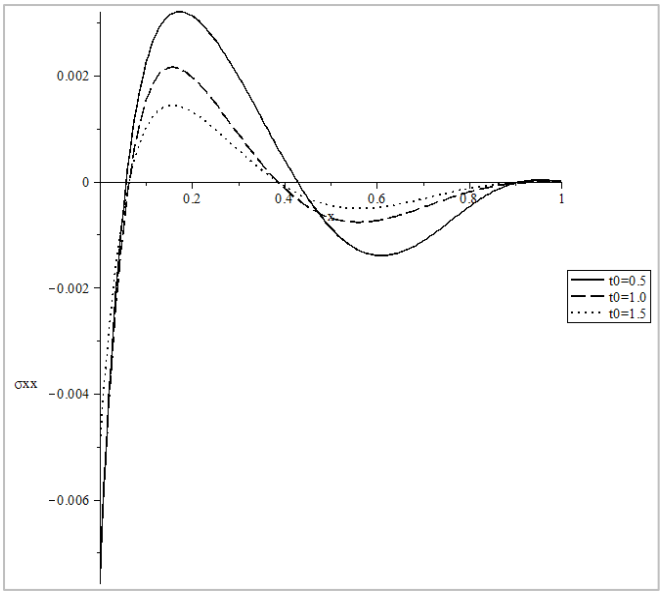

Figure 10: The stress distribution with variance values of ramping time parameter

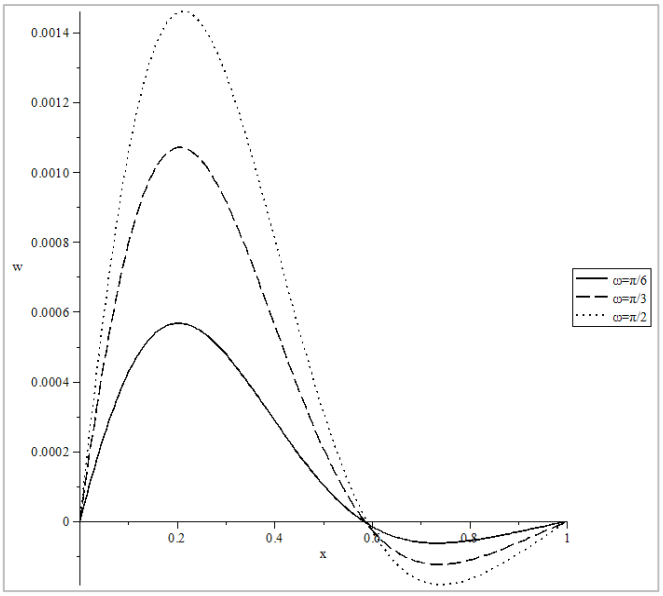

Figure 13: The lateral deflection distribution for variance values of angular thermal moment parameter

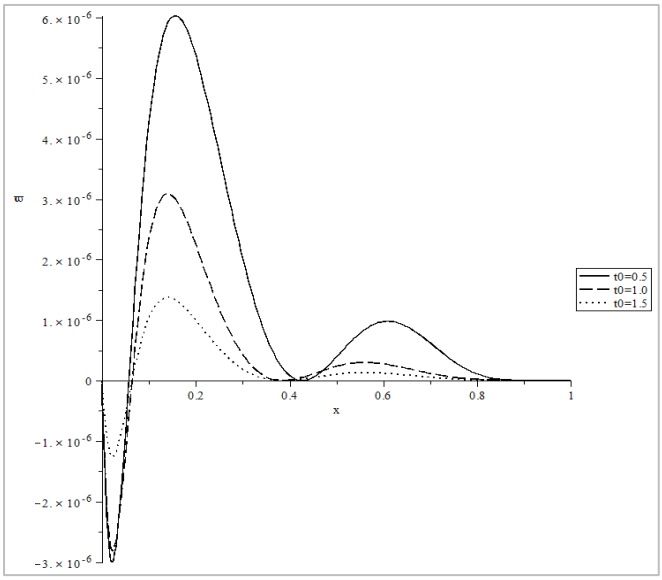

Figure 11: The stress-strain energy distribution with variance values of ramping time parameter

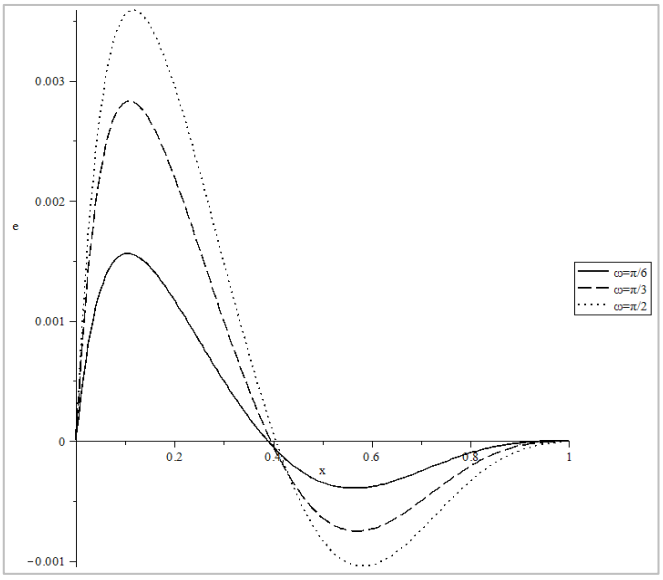

Figure 14: The deformation distribution for variance values of angular thermal moment parameter

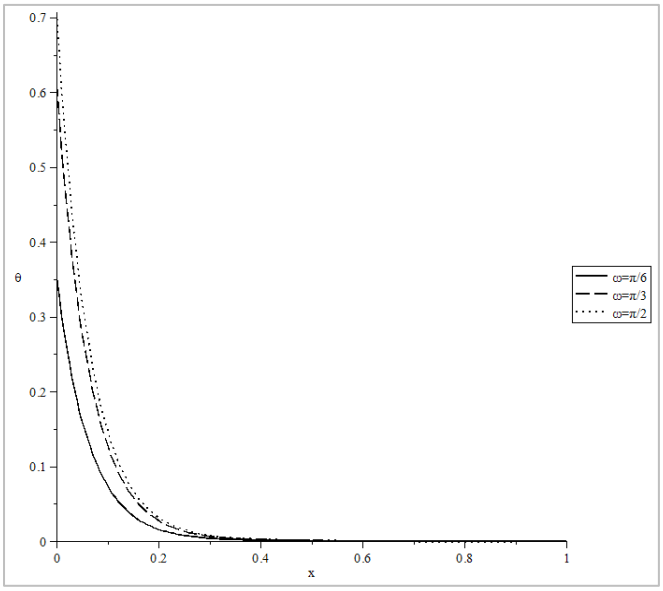

Figure 12: The temperature increments distribution for variance values of angular thermal moment parameter

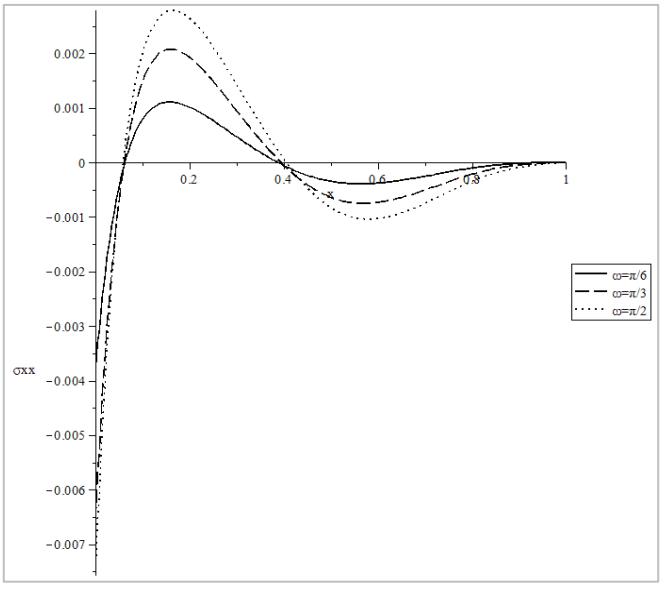

Figure 15: The stress distribution for variance values of angular thermal moment parameter

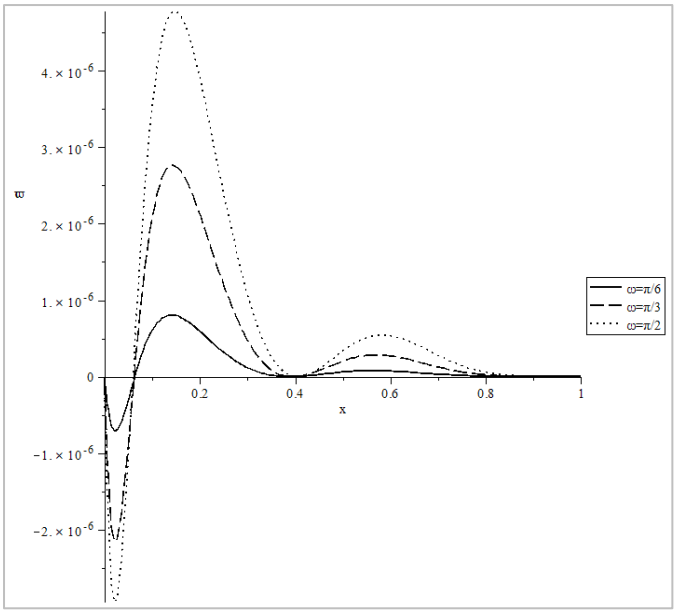

Figure 16: The stress-strain energy distribution for variance values of angular thermal moment parameter

References

[1] D. Tzou, On the thermal shock wave induced by a moving heat source. *J. Heat Transf.*, **1989**, *111*, 232-238. https://doi.org/10.1115/1.3250667

[2] D. Tzou, M.-t.M.H. Transfer, The Lagging Behavior, Taylor Francis, Washington (**1997**).

[3] M. Xu, J. Guo, L. Wang, L. Cheng, Thermal wave interference as the origin of the overshooting phenomenon in dual-phase-lagging heat conduction, *Int. J. Therm. Sci.*, **2011**, *50*, 825-830. https://doi.org/10.1016/j.ijthermalsci.2010.12.006

[4] N.S. Al-Huniti, M. Al-Nimr, Thermoelastic behavior of a composite slab under a rapid dual-phase-lag heating. *J. Therm. Stress.*, **2004**, *27*, 607-623. https://doi.org/10.1080/01495730490466200

[5] J.-R. Ho, C.-P. Kuo, W.-S. Jiaung, Study of heat transfer in multilayered structure within the framework of dual-phase-lag heat conduction model using lattice Boltzmann method. *Int. J. Heat Mass Transf.*, **2003**, *46*, 55-69. https://doi.org/10.1016/S0017-9310(02)00260-0

[6] Y.-M. Lee, T.-W. Tsai, Ultra-fast pulse-laser heating on a two-layered semi-infinite material with interfacial contact conductance. *Int. Commun. Heat Mass Transf.*, **2007**, *34*, 45-51. https://doi.org/10.1016/j.icheatmasstransfer.2006.08.017

[7] K.-C. Liu, Numerical analysis of dual-phase-lag heat transfer in a layered cylinder with nonlinear interface boundary conditions. *Comput. Phys. Commun.*, **2007**, *177*, 307-314. https://doi.org/10.1016/j.cpc.2007.02.110

[8] K. Ramadan, Semi-analytical solutions for the dual phase lag heat conduction in multilayered media. *Int. J. Therm. Sci.*, **2009**, *48*, 14-25. https://doi.org/10.1016/j.ijthermalsci.2008.03.004

[9] N. Alghamdi, Dual-Phase-Lagging Thermoelastic Damping Vibration in Micro-Nano Scale Beam Resonators with Voids. *Int. J. Multidisciplinary and Current Research* 5 (**2017**).

[10] N.A. Alghamdi, H.M. Youssef, Dual-phase-lagging thermoelastic damping in-extensional vibration of rotating nano-ring. *Microsyst. Technol.*, **2017**, *23*, 4333-4343. https://doi.org/10.1007/s00542-017-3294-z

[11] M.A. Biot, Thermoelasticity and irreversible thermodynamics. *J. Appl. Phys.*, **1956**, *27*, 240-253. https://doi.org/10.1063/1.1722351

[12] H. Youssef, N. Alghamdi, Thermoelastic damping in nanomechanical resonators based on two-temperature generalized thermoelasticity theory. *J. Therm. Stresses*, **2015**, *38*, 1345-1359. https://doi.org/10.1080/01495739.2015.1073541

[13] H.W. Lord, Y. Shulman, A generalized dynamical theory of thermoelasticity. *J. Mech. Phys. Solids*, **1967**, *15*, 299-309. https://doi.org/10.1016/0022-5096(67)90024-5

[14] R.S. Dhaliwal, H.H. Sherief, Generalized thermoelasticity for anisotropic media. *Q. Appl. Math.*, **1980**, *38*, 1-8.

[15] C.M. Hoang, Thermoelastic damping depending on vibration modes of nano beam resonator. *Commun. Phys.*, **2015**, *25*, 317. DOI: 10.15625/0868-3166/25/4/6887

[16] A.K. Naik, M. Hanay, W. Hiebert, X. Feng, M.L. Roukes, Towards single-molecule nanomechanical mass spectrometry. *Nat. Nanotechnol.*, **2009**, *4*, 445-450. https://doi.org/10.1038/nnano.2009.152

[17] A.D. O'Connell, M. Hofheinz, M. Ansmann, R.C. Bialczak, M. Lenander, E. Lucero, M. Neeley, D. Sank, H. Wang, M. Weides, Quantum ground state and single-phonon control of a mechanical resonator. *Nature*, **2010**, *464*, 697-703. https://doi.org/10.1038/nature08967

[18] J. Van Beek, R. Puers, A review of MEMS oscillators for frequency reference and timing applications. *J. Micromech. Microeng.*, **2011**, *22*, 013001.

[19] H.Youssef, K.A. Elsibai, Vibration of gold nanobeam induced by different types of thermal loading—a state-space approach. *Nanoscale Microscale Thermophys. Eng.*, **2011**, *15*, 48-69. https://doi.org/10.1080/15567265.2010.549929

[20] H. Youssef, Vibration of gold nanobeam with variable thermal conductivity: state-space approach. *Appl. Nanosci.*, **2013**, *3*, 397-407. DOI 10.1007/s13204-012-0158-9

[21] J. Sharma, D. Grover, Thermoelastic vibrations in micro-/nano-scale beam resonators with voids. *J. Sound Vib.*, **2011**, *330*, 2964-2977. https://doi.org/10.1016/j.jsv.2011.01.012

[22] Y. Sun, M. Saka, Thermoelastic damping in micro-scale circular plate resonators. *J. Sound and Vibration*, **2010**, *329*, 328-337. https://doi.org/10.1016/j.jsv.2009.09.014

[23] R. Lifshitz, M.L. Roukes, Thermoelastic damping in micro-and nanomechanical systems. *Physical Review B*, **2000**, *61*, 5600. https://doi.org/10.1103/PhysRevB.61.5600

[24] N.S. Al-Huniti, M. Al-Nimr, M. Naji, Dynamic response of a rod due to a moving heat source under the hyperbolic heat conduction model. *J. Sound Vib.*, **2001**, *242*, 629-640. https://doi.org/10.1006/jsvi.2000.3383

[25] E.A. Al-Lehaibi, H.M. Youssef, Vibration of gold nanobeam with variable young's modulus due to thermal shock. *World J. Nano Sci. Eng.*, **2015**, *5*, 194. DOI: 10.4236/wjnse.2015.54020

[26] B.A. Boley, Approximate analyses of thermally induced vibrations of beams and plates. *J. Appl. Mech.*, **1972**, *39*, 212-216. https://doi.org/10.1115/1.3422615

[27] J. Kidawa-Kukla, Application of the Green functions to the problem of the thermally induced vibration of a beam. *J. Sound Vibration*, **2003**, *262*, 865-876. https://doi.org/10.1016/S0022-460X(02)01133-1

[28] G. Manolis, D. Beskos, Thermally induced vibrations of beam structures, *Comput. Methods Appl. Mech. Eng.*, **1980**, *21*, 337-355. https://doi.org/10.1016/0045-7825(80)90101-2

[29] M.A. Biot, Theory of stress-strain relations in anisotropic viscoelasticity and relaxation phenomena. *J. Appl. Phys.*, **1954**, *25*, 1385-1391. DOI:10.1063/1.1721573

[30] M.A. Biot, Variational principles in irreversible thermodynamics with application to viscoelasticity. *Physical Review*, **1955**, *97*, 1463. https://doi.org/10.1103/PhysRev.97.1463

[31] A. Drozdov, A constitutive model in finite thermoviscoelasticity based on the concept of transient networks. *Acta Mechanica*, **1999**, *133*, 13-37. https://doi.org/10.1007/BF01179008

[32] M.A. Ezzat, A.S. El-Karamany, The relaxation effects of the volume properties of viscoelastic material in generalized thermoelasticity. *Int. J. Eng. Sci.*, **2003**, *41*, 2281-2298. https://doi.org/10.1016/S0020-7225(03)00108-3

[33] J.M. Carcione, F. Poletto, D. Gei, 3-D wave simulation in anelastic media using the Kelvin–Voigt constitutive equation. *J. Comput. Phys.*, **2004**, *196*, 282-297. https://doi.org/10.1016/j.jcp.2003.10.024

[34] D. Grover, Viscothermoelastic vibrations in micro-scale beam resonators with linearly varying thickness. *Can. J. Phys.*, **2012**, *90*, 487-496. https://doi.org/10.1139/p2012-044

[35] D. Grover, Damping in thin circular viscothermoelastic plate resonators. *Can. J. Phys.*, **2015**, *93*, 1597-1605. https://doi.org/10.1139/cjp-2014-0575

[36] D. Grover, Transverse vibrations in micro-scale viscothermoelastic beam resonators. *Arch. Appl. Mech.*, **2013**, *83*, 303-314. https://doi.org/10.1007/s00419-012-0656-y

[37] D. Grover, R. Seth, Viscothermoelastic micro-scale beam resonators based on dual-phase lagging model. *Microsyst. Technol.*, **2018**, *24*, 1667-1672. https://doi.org/10.1007/s00542-017-3515-5

[38] H. Youssef, N.A. Al-Ghamdi, Vibration of Gold Nano Beam in Context of Two-Temperature Generalized Thermoelasticity without energy dissipation, ICTEA: International Conference on Thermal Engineering, **2017**.

[39] K.A. Elsibai, H.M. Youssef, State-space approach to vibration of gold nanobeam induced by ramp type heating without energy dissipation in femtoseconds scale. *J. Therm. Stresses*, **2011**, *34*, 244-263. https://doi.org/10.1007/BF03353632

Journal of Umm Al-Qura University for Applied Science

journal homepage: https://uqu.edu.sa/en/jas/87823

Approaches of Energy-Saving Facades – Review Article

M. Sabry [a,b].

[a] *Physics department, College of Applied Science, Umm Al-Qura, Makkah, Saudi Arabia.*
[b] *Solar Physics Lab., National Research Institute of Astronomy and Geophysics, Cairo, Egypt*

ARTICLE INFO

Article History:
Submission date: 11/10/2019
Acceptance date: 2/12/2019

Keywords:
Energy-saving façade; smart windows; building-integrated photovoltaic.

ABSTRACT

Energy-saving facades is getting excessive attention nowadays as it is considered a step towards achieving zero-energy environment. Using good management of energy flowing into buildings, the energy consumption could be saved in term of heating, cooling and lighting load. With integration to Photovoltaics, extra electricity could be obtained to support building energy consumption. Overall energy performance of different designs and innovations of building's façades have been introduced and evaluated in many researches. The ability to control energy flow and/or to produce some sort of extra energy is currently known as "Smart Windows". In this article, the basic concepts of performance of the different façade designs, as well as energy-saving and energy-producing emerging technologies to this field were reviewed.

1. Introduction

Fossil fuels in the form of coal, oil and natural gas are the major sources of conventional energy for many countries to meet their requirement for power. The reserves of such fossil fuels are exhausted largely due to its continued use. Besides, it has a very high impact on the globe. Many of the environmental problems we face (climatic change, atmospheric pollution, oil leaks, etc.) result from consumption of such fossil fuels.

Solar energy is one of the most competitive free sources of renewable energy that could be exploited without any limits. It can produce electricity or heat, or both, depending on how they capture solar energy [1–3].

As the world's demand for renewable energy is increasing, great attention is given to the zero, or minimum -emission building [1]. For aiming as such, building need to stop or minimize its energy loss through the building's facades and produce energy from its surroundings. Energy from the sun is the most candidate for such job.

Reaching these goals could achieved by a choosing an appropriate design of the Building's façade, depending on the climatic zone, besides introducing Building integrated photovoltaic (BIPV) systems.

Old-style façade designs regarded the external building's skin as a blocking barrier between the outdoor climate and the highly controlled interior environment. Efficiency of such façade was measured by its ability to isolate the building's interior from the outdoor environment so that the cooling system could operate as efficiently as possible [4]. However, recent concepts of facade designs consider the building facade as a filter between the external and internal environment [5].

The building's façade serves as the interface between the interior and the exterior space and plays an important role in thermal load control, ventilation, noise control, design quality and visual comfort. Fresh air, heat and sunlight can be achieved through building's façade, and they can be dissipated.

For providing the occupier with a comfortable thermal and visual environment, a façade should satisfy many functions, without which additional components must be added to or in the vicinity of such façade [6].

Energy saving smart windows are those windows and façades that can prevent energy from escaping to or from the building. Energy producing smart windows and building integrated photovoltaic (BIPV) systems are those windows that can use such prevented energy to produce electricity by means of solar cells. Such smart windows can utilize solar radiation to produce electrical energy. They may signify a powerful and useful tool for achieving such increasing demand for zero energy and zero emission buildings of the near future

In this review, different façade technologies will be briefly overviewed. Smart windows and their advanced approaches, the latest technology regarding energy-saving and energy-producing windows technologies will be overviewed. Building integrated Photovoltaics will be under focus.

2. Modern Building Design and Façades

At the present time, there is an increasing concern on the development of sustainable building over the world. Energy conservation in buildings is one of the major concerns. Building experts can add to this area by the supervision of the energy consumption of buildings, especially the fully air-conditioned buildings (as in the case of the Middle East, and similar climatic zone over the world), through a refined building design.

Globally, buildings are responsible for approximately 40% of the total world annual energy consumption with the resulting carbon emissions substantially more than those in the transportation sector. Most of this energy is for the provision of lighting, heating, cooling, and air conditioning [7]. In a typical commercial building, air-conditioning system is the largest source of power consumption. It may account for up to 45% of the total power consumption of such buildings. Surplus heat energy is extracted to the outdoor space by air-conditioning system. One of the major thermal loads in the building envelope heat gain is the heat transfer through window glazing of the building façade [8, 9].

Not that the Middle East is alone in its love of the shiny stuff. Across the US, Europe and China, architects have been designing and building glass towers since long time ago. Nevertheless, in most of these markets, temperatures do not reach 40°C for weeks as in the case of Middle East, turning those modern towers into greenhouses [10].

User comfort is an essential demand that characterizes the design of the buildings construction. Different demands on the comfort level are posed for different types of buildings such as residential or office buildings Essential criteria are [11]

- Thermal comfort
- Hygienic comfort
- Acoustic comfort
- Visual comfort

Façades are very eminent architectural and design elements for architects as it gives their designs a unique appearance. Besides

* **Corresponding Author**
Physics department, College of Applied Science, Umm Al-Qura, Makkah, Saudi Arabia.
E-mail address: mmsalaheldin@uqu.edu.sa

affecting the building's indoor thermal and visual comfort that is responsible for satisfaction of the residents or employees [11,12], it also determines the overall consumed energy (including lighting, heating and cooling loads) and the operating costs of a building [13].

Choosing to block sunrays by traditional curtains – for preventing direct sunlight and glare – results in complete or partial darkening of the room and raising the need of using artificial light sources inside the building. On the other hand, choosing not to use curtains will result in allowing direct sunlight with glare to harm the human eyes besides allowing thermal energy to flow to the room resulting in heating up the area, hence, using air conditioners with higher electric load. Blinds are frequently used with such glazing façades or room external windows to control transmitting direct (beam) solar radiation component, but without the use of such valuable blocked energy.

In order to monitor building's energy consumption especially in cooling and air conditioning, different ways have been developed and discussed [14–16].

Because of the increasing demand of new domestic and business constructions using building facade technologies, such demand for high energy-efficiency buildings requires more application of building thermal and visual simulation to examine the energy consumption for the building by selecting the effective façade system considering the availability of material in the region under discussion [17,18].

In this context, BIPVs offer an aesthetic, economic and practical solution for integrating photovoltaics in order to harvesting solar radiation to produce electricity and minimize energy consumption as well. Building integration of photovoltaic cells are installed on sloped or flat roofs. It could also be installed as facades and solar shading systems, BIPV systems can easily replace the outer building envelope, serving as a climate screen and a power source for electricity generation simultaneously [19].

Solar façades could be classified in many different ways according to different scopes or different specific points of interest. They might be classified according to their transparency, type of energy produced, energy consumption, etc. The following is a general classification of the existing façade technologies.

2.1. Type of Energy Generated

Solar façades may utilize solar energy for thermal energy gain like space heating, cooling or ventilation. Electrical energy generation could also be utilized by means of PV. There exist systems that can generate both thermal and electrical energy simultaneously [20].

2.2. Opaque and Transparent

Opaque facades absorb and/or reflect the incident solar radiation but cannot transfer directly solar heat gain into the building, while transparent and translucent facades can absorb, reflect, or transfer the incident solar radiation gain into the building's interior [2].

2.3. Concentrated and Non-Concentrated Solar Energy

Solar concentrators may be used in building façades in order to increase total system collection efficiency. They could be used for both solar thermal as well as PV technology, or a combination of both.

However, regarding their energy generation or consumption, building facades are classified mainly into three categories, passive façades, energy-consuming façades, and energy-producing facades.

3. Passive Building-Integrated Façades

In general, facades are considered passive if they interact with the incident solar radiation but cannot transfer such energy into a useful electrical or thermal energy. They are considered as energy-consuming facades if they consume energy during their operation. Finally, they are considered energy-producing façades if they use such incident energy to generate electricity. Double skin solar façade systems are the simplest amongst all facades. Those systems directly use solar energy to achieve energy gains. They neither use external energy for operation (although internal fans may be used for air circulation and spread)., nor generate energy during operation.

3.1. Heating, Cooling or ventilation due to differential air densities

Using the fact that hot air is less in density than that of cold air hence goes up; facades could be used for purposes of space heating, cooling or just air ventilation depending on the design.

Ventilation of facade elements decrease thermal transfer through the building envelope and reduces the need of the conventional insulation materials usually used in the buildings. Being a two stages protection against wind and rain reduces the occurrence of building defects of the outer layer [21]. Fig. 1 shows different designs for double-skin passive façade. Fig. 1(a) is a monolithic porous façade design for air ventilation that could also be considered to serve for worming process. Transparent or semi-transparent glazing could be used as an envelope of the building exterior in order to transmit thermal energy and choose a proper design to use such energy. Fig. 1(b) is a transparent or semi-transparent glazing façade for space heating by swapping cold air accumulated in the bottom of the room (as it has a higher density) to outside and is then heated up as it elevates to enter the room as a hot air. This design could be considered as a thermal storage wall. Transparent or semi-transparent glazing façade may be used for either space heating and ventilation by rejecting cooler air accumulating in the bottom of the room as shown in Fig. 1(c); or for space cooling and ventilation by rejecting hot air accumulated in the top of the room as in Fig. 1(d). Fig. 1(e) is the traditional double façade that isolates building's interior from interaction with external weather, while Fig. 1(f) is used for thermal energy rejection for reducing thermal energy flowing into the building.

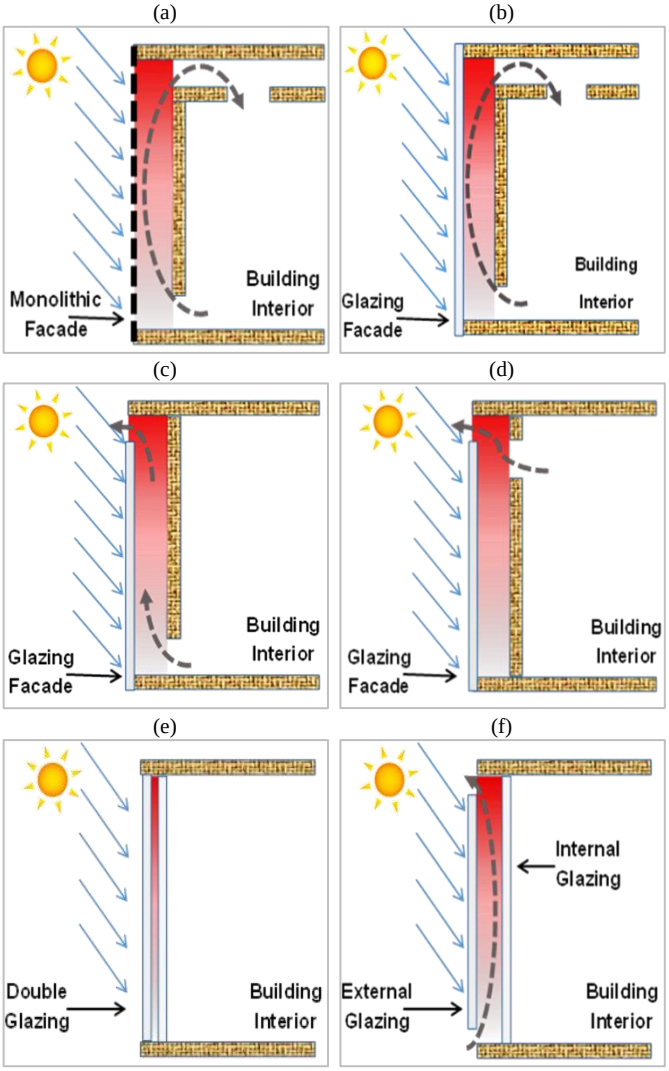

Figure 1: Passive building-integrated façade designs for (a) air ventilation and worming; (b) space heating; (c) space heating and ventilation; (d) space cooling and ventilation (e) thermal insulation, and (f) cooling.

3.2. Low Emissivity Glazing

Low emissivity (Low-E) coatings are spectrally selective films aiming to allow the visible light to pass through it, and block the infrared radiation which generally create heat. Schematic of Low emissivity glazing window is shown in Fig. 2. Because of its high IR-reflectance, this type of glazing has been developed greatly, and many have studied their different properties. Currently there are two existing technologies of low-e coatings, namely, tin oxide based hard coating, and silver based soft coating that has higher IR reflectance and lower transmittance than the former. However, the visible

transmittance of hard coatings can be increased using antireflection property of silicon dioxide [22].

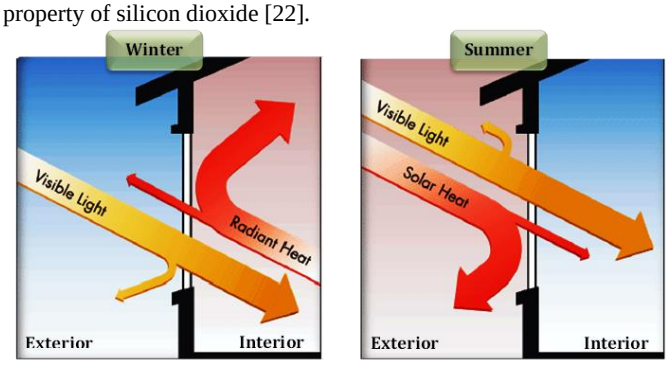

Figure 2: Schematic of Low emissivity glazing window [22].

3.3. Dielectric/metal/dielectric Glazing

Dielectric/metal/dielectric films coated on top of glass substrates show great energy saving effects by reflecting the IR radiation by the metal film and transmitting visible and near IR radiation through the two antireflective dielectric coatings. Design, fabrication and optical properties of dielectric/metal/dielectric films have been studied by many researchers aiming the optimization of such layer. Beside the optimized performance, cost of these films in terms of their material and the fabrication technique is also important [22,23]. Glazing coated with $TiO_2/Cu/TiO_2$ as an example is shown schematically in Fig. 3 along with its optical properties [24].

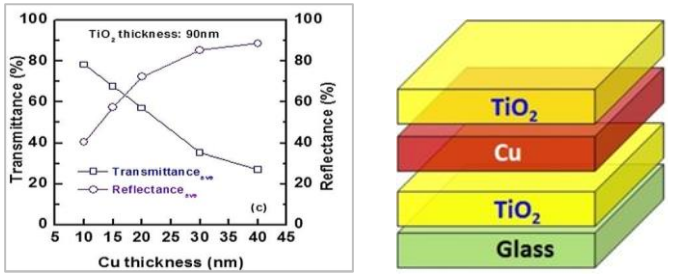

Figure 3: TiO_2 / Cu / TiO_2 deposited on a glass substrate (left), and effect of varying Cu thickness on the transmittance and reflectance (right) [25].

3.4. Thermochromic Glazing

Broadly speaking, thermochromism is the temperature-dependent changes in the optical properties of a material [26]. Thermochromic material shown schematically in Fig. 4 [24] has the ability to control the quantity of solar energy entering the building or escaping from it [27,28], by changing its optical properties hence color upon reaching a characteristic "transition temperature". Thus, reducing cooling or heating loads as appropriate.

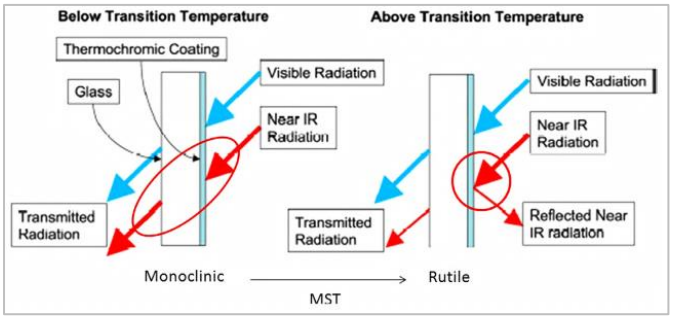

Figure 4: Schematic representation of thermochromic materials applied as an intelligent windows coating [24].

3.5. Thermotropic Glazing

Thermotropics are types chromogenic materials that can show an adjustable change in their optical properties depending on its temperature. These materials are either a combination of two components that show a phase separation at and above a specific temperature or are formed by particles uniformly embedded in a polymer [29] which change its orientation at and above a specific temperature. In other words, a material is considered thermotropic if it can be re-oriented or rotated by changing its operating temperature. At high temperature, such material induces a phase transition: and changes to an isotropic liquid., In contrary, if temperature is too low to support a thermotropic phase, the material will change to glass phase [30], as shown schematically in Fig. 5.

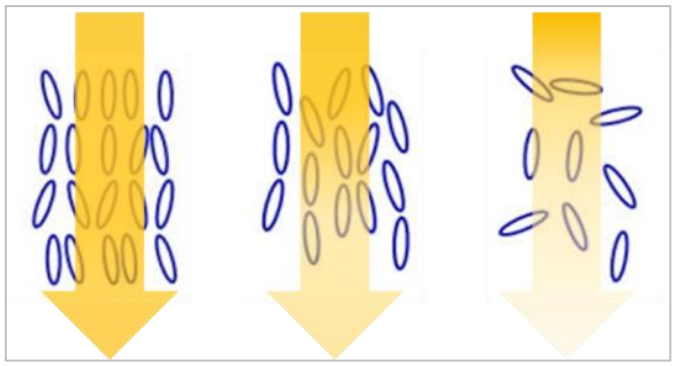

Figure 5: Thermotropic material changes its phase with increasing temperature.

3.6. Photochromic Glazing

Photochromic windows are made from transparent materials that can change their color upon exposing to sunlight, with similar materials used in sunglasses. Such materials response to light intensity, regardless any temperature changes. Cost-effectiveness and durability of such glazing for mass production are not yet commercially available.

4. Energy-Consuming Façades

Flow of energy through façades and windows may be controlled using energy-consuming technologies, by applying external electric power to adjust their optical properties and their transparency as will be reviewed in the next paragraphs.

4.1. Polymer Dispersed Liquid Crystals (PDLCs)

In these glazing or windows, the liquid crystals respond to an electrical charge by aligning parallel and letting light through. When the electrical charge is absent, the liquid crystals in the window are randomly oriented resulting in complete blocking of incident sun light. In PDLCs, the window is either clear or translucent, without any ability to control its transparency. Fig. 6 shows a schematic of PDLC operation method.

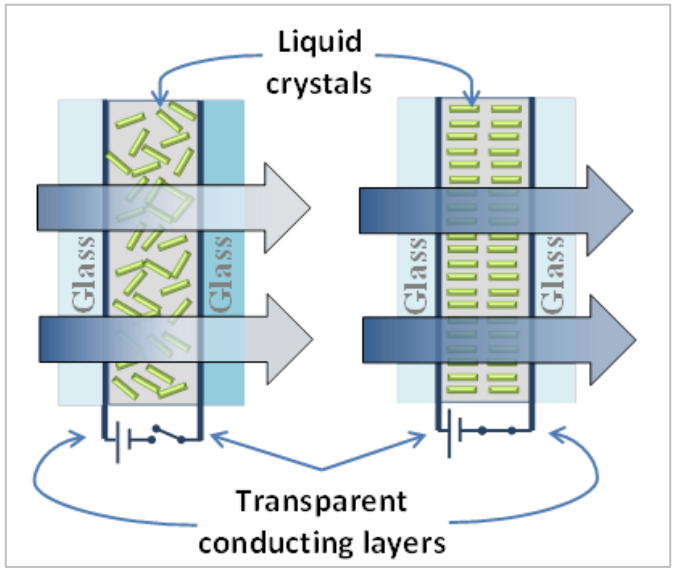

Figure 6: Schematic of PDLC Glazing

4.2. Suspended Particle Display Devices (SPDs)

Whose operation principle is similar to the PDLCs except that the polymer crystals are replaced with smaller particles or to switch from clear to dark. In such window, SPDs are sited between two glass panes coated with a transparent conductive material. When the triggering electric circuit is closed, an electric field is generated between the two glass panes which makes the SPDs to line up in a straight line allowing

light to flow through the window. Once the circuit is disconnected, SPDs disperse back randomly and block light from transmitting through. By controlling the applied voltage, the window's transparency is reduced until it's completely opaque. Fig. 7 shows a schematic of SPD smart windows operation method.

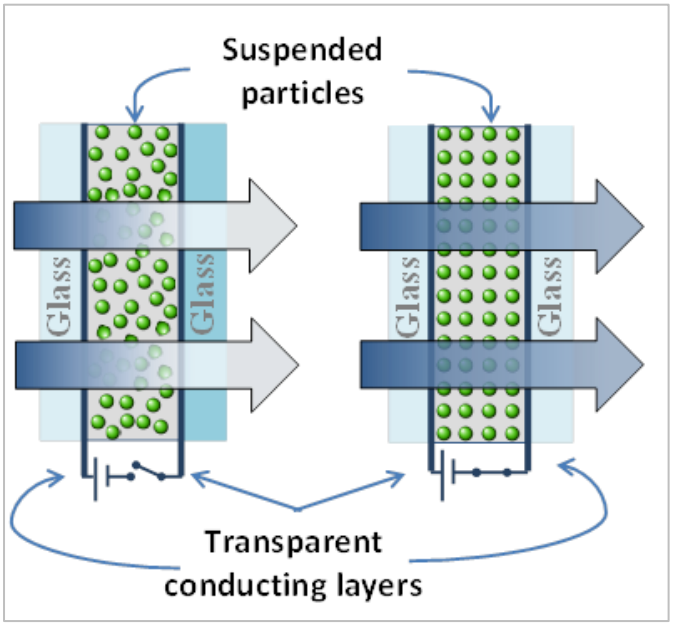

Figure 7: Schematic of SPD Glazing

4.3. Electrochromic Windows

Electrochromic materials have the property of changing their color as affected either by an electron-transfer process or by a sufficient electrochemical potential. Essentially, electricity triggers a chemical reaction in this sort of material. This reaction changes the properties of the material. In this case, the reaction changes the way the material reflects and absorbs light. In some electrochromic materials, the change is between different colors [31]. In electrochromic windows, the material can change its color and transparency as illustrated in Fig. 8.

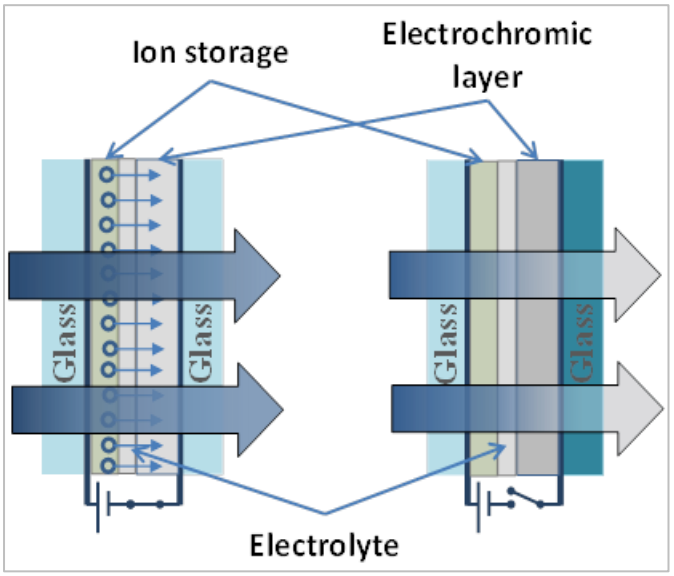

Figure 8: Electrochromic Glazing

5. Energy Producing Façades

Energy could be produced by integrating PV to the building's façades or by fixing to the roof. Building integrated photovoltaic (BIPV) system is defined as photovoltaic cells which can be integrated into the building envelope as part of the building structure, and therefore can replace conventional building materials, rather than being installed afterwards [32]. The PV modules serve a dual function of building skin by replacing conventional building materials and generating power [33]. In the next paragraphs, an overview of the possible technologies of BIPV are presented.

5.1. Façades and Roof-top mounted PV

Many papers have either proposed new ideas or tested existing technologies as will be mentioned below. The most straight forward solutions to build a BIPV is to integrate directly into the building's roof to use the whole building's roof area as shown in Fig. 9. This is most suitable for one story buildings like Airports, Train stations, etc. Such roof-top PVs could be semi-transparent (amorphous PV, or opaque PVs that are arranged in panels with large spacing between the PV units) for daylight utilization.

façades intended for cooling besides generating clean electricity are shown schematically in Fig. 10, in which PV acts as a building façade with an ample spacing with the building's body. Since the operating PV temperature plays a crucial role in its performance [34], this configuration is very effective, as making a channel for air to circulate and remove heat accumulated on the PV back side, hence cooling both building's interior and the PV itself for better performance. In contrast, such heat accumulated could be allowed to emerge into the building's interior acting as a heating source as in Fig. 11.

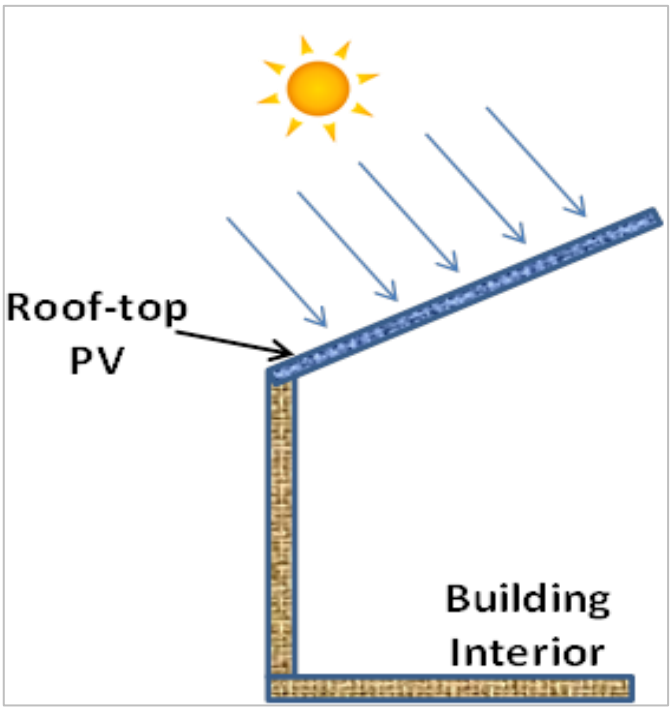

Figure 9: Roof-top integrated PV

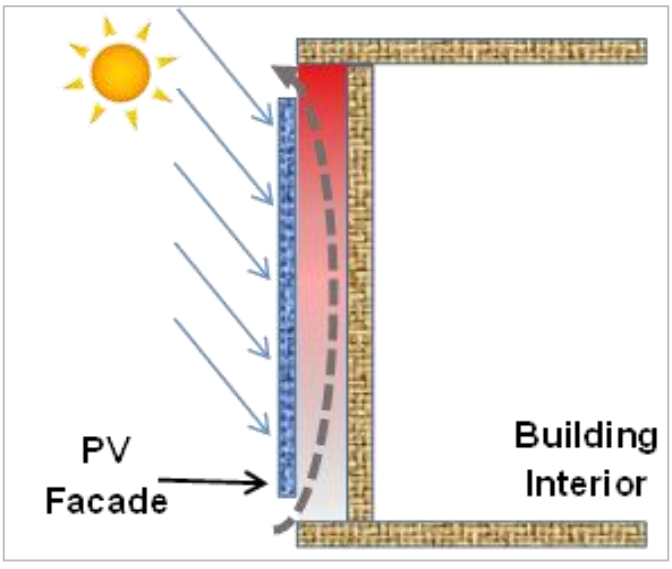

Figure 10: PV integrated façade for electricity production while rejecting accumulated thermal energy behind PV (space cooling)

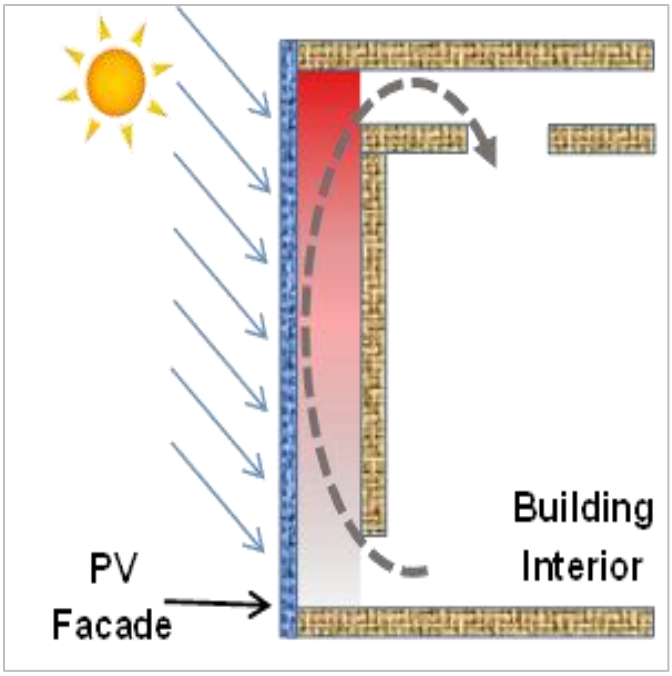

Figure 11: PV-integrated façade for electricity production, while utilizing accumulated thermal energy in space heating,

5.2. Radiation Capturing by Total Internal Reflection Glazing

Concentrated PV can play a role in BIPV in different ways to maximize the use of PV and minimize its cost. Solar radiation could be concentrated with the use of a phenomena called total internal reflection of a light ray that occurs when it strikes a medium boundary at an angle larger than the critical angle with respect to a normal to the surface. This phenomenon could be of use by redirecting solar radiation incident on windows to be collected by means of small area solar cells embedded in such window. This will happen at a specific orientation of such Window based on the design, latitude of the building, and principle of operation.

Transparent acrylic CPC Smart Windows having the absorber (solar cell) inclined with the latitude of the location (i.e. facing sun) has been investigated [35]. Schematic of the investigated system is represented in Fig. 12.

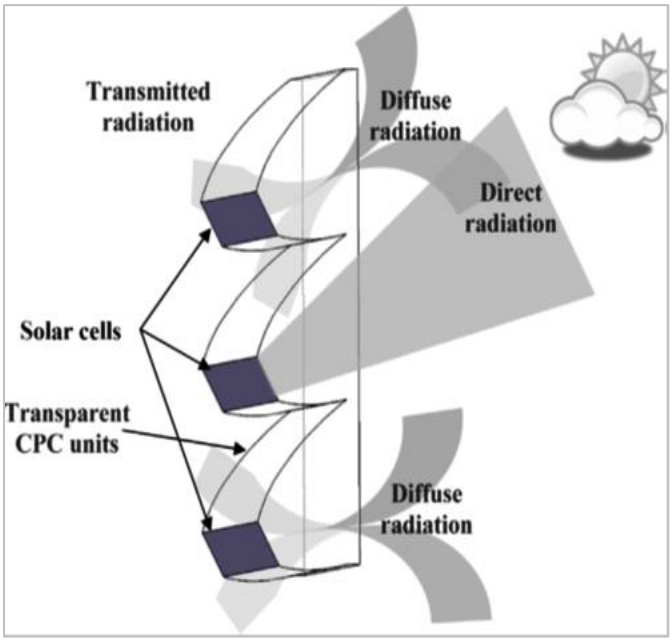

Figure 12: PV-integrated CPC for transparent façades [35].

Another Smart Window consisting of Low-concentration Photovoltaic system in the form of prismatic segmented façade. Prism head angle determines the zenith angle after which direct solar radiation is reflected internally to be collected by solar cell integrated in the window as shown in Fig. 13 [36].

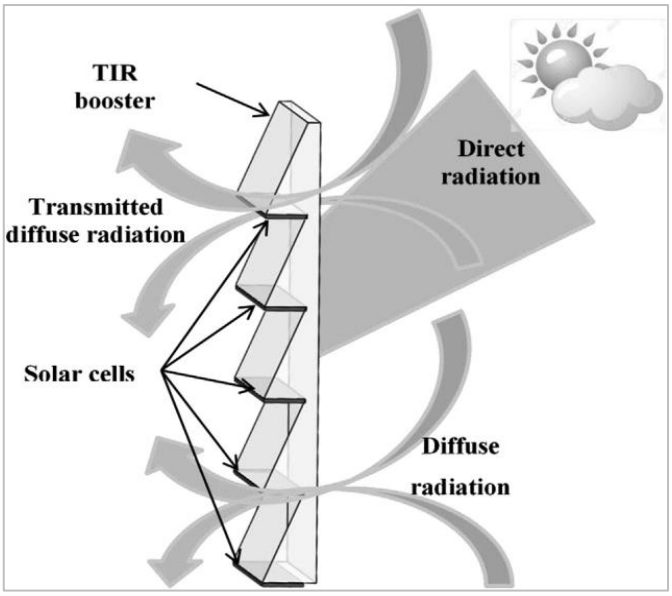

Figure 13: Prismatic low-concentration PV integrated façades [36].

5.3. Thermotropic with built-in PV Glazing

Another approach of energy-producing glazing consists of a thermotropic layer with integrated PVs. This system responds to climatic conditions by varying the percentages of solar energy reflected to the PV for electricity generation and the transmitted the building for light and heat provision [37, 38] as shown in Fig. 14.

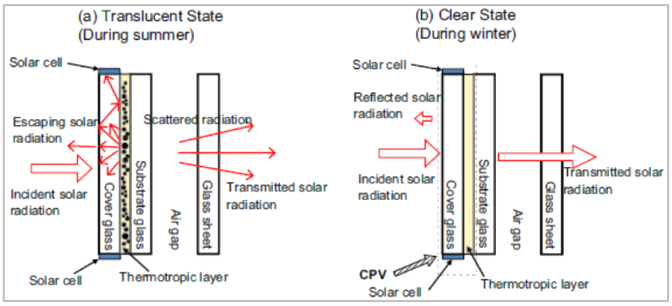

Figure 14: Design and development of a reflective membrane for a Building Integrated Concentrating Photovoltaic [37].

5.4. PV/T Integrated Glazing

Thermal as well as electrical energy could be extracted from a window whose solar cells operate under high concentration ratio. Such system can generate both electricity and hot water or air directly for domestic use inside the building in addition to allowing diffused radiation to penetrate to the building's interior [20] as shown schematically in Fig. 15

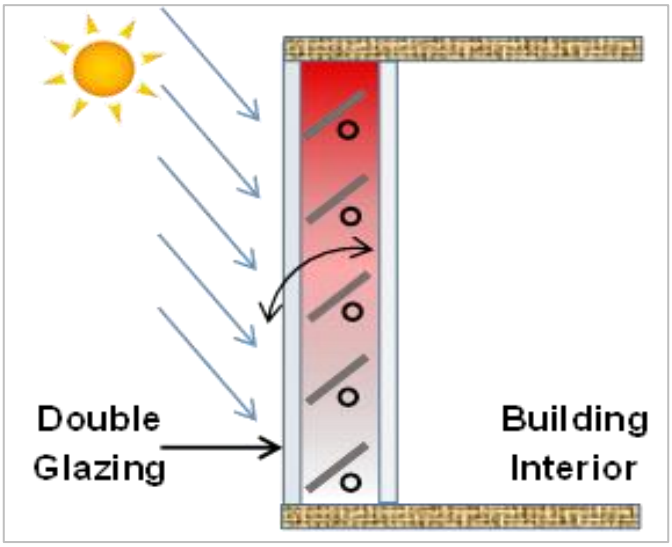

Figure 15: PV/T integrated façade.

6. Conclusions

The ability to control energy flow and/or to produce some sort of extra energy is currently known as "Smart Windows". In this article, the basic concepts of performance of the different façade designs, as well as energy-saving and energy-producing emerging technologies to this field were reviewed. Different types and strategies of Energy-saving facades was adopted in this review, which is considered a step towards achieving zero-energy environment. Accepting a specific type of such reviewed types was based on the appropriateness of accompanying factors, like sky clearness, height of the surrounding buildings, area of the roofs of façades of the building under test, etc. Using good management of energy flowing into buildings, the energy consumption inside the considered building could be saved in term of heating, cooling and lighting loads. This could even produce energy if integrated with Photovoltaics. Extra electricity could be obtained to support building energy consumption.

References

[1] B. P. Jelle. Building Integrated Photovoltaics: A Concise Description of the Current State of the Art and Possible Research Pathways. *Energies*, **2015**, *9*, 21. https://doi.org/10.3390/en9010021

[2] B. P. Jelle, C. Breivik. State-of-the-art Building Integrated Photovoltaics. *Energy Procedia*, **2012**, *20*, 68–77. https://doi.org/10.1016/j.egypro.2012.03.009

[3] B. P. Jelle, C. Breivik. The Path to the Building Integrated Photovoltaics of Tomorrow. *Energy Procedia*, **2012**, *20*, 78–87. https://doi.org/10.1016/j.egypro.2012.03.010

[4] L. Hasanzadeh. *design of living façade for a school building to enhance students' visual comfort*. Eindhoven University of Technologyhttps://pure.tue.nl/ws/files/46912426/749155-1.pdf (**2012**).

[5] E. Zarghami, A. S. Habib Abad. New Technologies in Construction Materials Based on Environmental Approach (Case Study: Double Skin Facades). *Mediterranean J. Social Sci*., **2015**, *6*, 17-24. 2015. DOI: 10.5901/mjss. 2015.v6n6s6p17.

[6] Climate and Energy. In: Façades. Birkhäuser Basel, **2007**, pp. 70–84. DOI: https://doi.org/10.1007/978-3-7643-8281-0_5

[7] A. M. Omer. Energy, environment and sustainable development. *Renewable and Sustainable Energy Reviews*, **2008**, *12*, 2265–2300. https://doi.org/10.1016/j.rser.2007.05.001

[8] A. L. S. Chan, T. T. Chow, K. F. Fong, et al. Investigation on energy performance of double skin façade in Hong Kong. *Energy and Buildings*, **2009**, *41*, 1135–1142. https://doi.org/10.1016/j.enbuild.2009.05.012

[9] N. Hamza. Double versus single skin facades in hot arid areas. *Energy and Buildings*, **2008**, *40*, 240–248. https://doi.org/10.1016/j.enbuild.2007.02.025

[10] O. Crowcroft. Passing facade | ConstructionWeekOnline.com. *constructionweekonline*http://www.constructionweekonline.com /article-11108-passing-facade/1/ (2011, accessed 27 August 2017).

[11] U. Knaack, T. Klein, M. Bilow, et al. (eds). Introduction. In: *Façades: Principles of Construction*. Basel: Birkhäuser Basel, pp. 7–13.

[12] M. E. Ali, S. Mohamed, E. A. Shaawat, N. Ashraf. Comparative study of energy performance of an institutional building for different façade configurations in Saudi Arabia. *Graz, Austria*, **2013**, 1334–1341.

[13] A. Khezri. *Comparative Analysis of PV Shading Devices for Energy Performance and Daylight*. Master Thesis, Norwegian university of science and technology, **2012**.

[14] A. J. Marszal, P. Heiselberg, J. S. Bourrelle, et al. Zero Energy Building – A review of definitions and calculation methodologies. *Energy and Buildings*, **2011**, *43*, 971–979. https://doi.org/10.1016/j.enbuild.2010.12.022

[15] L. Pérez-Lombard, J. Ortiz, J. F. Coronel, et al. A review of HVAC systems requirements in building energy regulations. *Energy and Buildings*, **2011**, *43*, 255–268. https://doi.org/10.1016/j.enbuild.2010.10.025

[16] L. Pérez-Lombard, J. Ortiz, C. Pout. A review on buildings energy consumption information. *Energy and Buildings* 2008; 40: 394–398. https://doi.org/10.1016/j.enbuild.2007.03.007

[17] A. H. Binamu. *Integrating Building Design Properties 'air Tightness' and Ventilation Heat Recovery for Minimum Heating Energy Consumption in Cold Climates*. Tampere University of Technology, **2002**.

[18] N. Ashraf, F. Al-Maziad. Effects of facade on the energy performance of Education Building in Saudi Arabia. Conference: World Sustainable Building **2014** Conference At: Barcelona, Spain. ISBN: 978-84-697-1815-5.

[19] G. Agarwal, A. Agarwal, S. Agarwal. BIPV: Integration of Photovoltaic with the Construction to achieve the concept of Agility. International Conference on Advanced and Agile Manufacturing, ICAM **2014**, Held at Oakland University, Rochester, MI 48309, USA.

[20] M. Sabry, P. C. Eames, H. Singh, et al. Smart windows: Thermal modelling and evaluation. *Solar Energy*, **2014**, *103*, 200–209. https://doi.org/10.1016/j.solener.2014.02.016

[21] C. Romila. R. Claudiu. General Principles for the Design and Construction of Ventilated Façades. *Buletinul Institutului Politehnic din lasi Sectia Constructii, Arhitectura* **2013**, *59*, 161.

[22] M. Kamalisarvestani, R. Saidur, S. Mekhilef, et al. Performance, materials and coating technologies of thermochromic thin films on smart windows. *Renewable and Sustain. Energy Reviews*, **2013**, *26*, 353–364. https://doi.org/10.1016/j.rser.2013.05.038

[23] G. Leftheriotis, P. Yianoulis, D. Patrikios. Deposition and optical properties of optimised ZnS/Ag/ZnS thin films for energy saving applications. *Thin Solid Films*, **1997**, *306*, 92–99. https://doi.org/10.1016/S0040-6090(97)00250-2

[24] P. Kiria, G. Hyett, R. Binions. Solid State Thermochromic Materials. *Advanced Materials Letters*, **2010**, *1*, 86–105. DOI: 10.5185/amlett.2010.8147

[25] G. K. Dalapati, S. Masudy-Panah, S. T. Chua, et al. Color tunable low cost transparent heat reflector using copper and titanium oxide for energy saving application. *Sci Rep*., **2016**, *6***,** 20182. https://doi.org/10.1038/srep20182

[26] M. E. A. Warwick, R. Binions. Advances in thermochromic vanadium dioxide films. *J Mater Chem A* **2014**, *2*, 3275–3292. https://doi.org/10.1039/C3TA14124A

[27] G. Kokogiannakis, J. Darkwa, C. Aloisio. Simulating Thermochromic and Heat Mirror Glazing Systems in Hot and Cold Climates. *Energy Procedia*, **2014**, *62*, 22–31. https://doi.org/10.1016/j.egypro.2014.12.363

[28] M. Saeli, C. Piccirillo, I. P. Parkin, et al. Energy modelling studies of thermochromic glazing. *Energy and Buildings*. 2010, 42, 1666–1673. https://doi.org/10.1016/j.enbuild.2010.04.010

[29] A. C. Gladen, J. H. Davidson, S. C. Mantell. Selection of thermotropic materials for overheat protection of polymer absorbers. *Solar Energy*, 2014, 104, 42–51. https://doi.org/10.1016/j.solener.2013.10.026

[30] A. Seeboth, R. Ruhmann, O. Mühling. Thermotropic and Thermochromic Polymer Based Materials for Adaptive Solar Control. *Materials*, **2010**, *3*, 5143–5168.

[31] N. L. Sbar, L. Podbelski, H. M. Yang, et al. Electrochromic dynamic windows for office buildings. *Int. J. Sustain. Built Environ.*, **2012**, *1*, 125–139. https://doi.org/10.1016/j.ijsbe.2012.09.001

[32] A. Henemann,. BIPV: Built-in solar energy. *Renewable Energy Focus*, **2008**, *9*, 14–19. https://doi.org/10.1016/S1471-0846(08)70179-3

[33] M. Debbarma, K. Sudhakar, P. Baredar. Comparison of BIPV and BIPVT: A review. *Resource-Efficient Technologies*, **2017**, *3*, 263–271. https://doi.org/10.1016/j.reffit.2016.11.013

[34] M. Sabry, A. E. Ghitas. Influence of temperature on methods for determining silicon solar cell series resistance. *J. Sol. Energy Eng.*, **2007**, *129*, 331–335. https://doi.org/10.1115/1.2735350

[35] M. Sabry, Y. A. Abdel-Hadi, A. Ghitas. PV-integrated CPC for transparent façades. *Energy and Buildings*, **2013**, *66*, 480–484. https://doi.org/10.1016/j.enbuild.2013.07.059Get rights and content

[36] M. Sabry. Prismatic TIR (total internal reflection) low-concentration PV (photovoltaics)-integrated façade for low latitudes. *Energy*, **2016**, *107*, 473–481.

[37] K. Connelly, Y. Wu, J. Chen, et al. Design and development of a reflective membrane for a novel Building Integrated Concentrating Photovoltaic (BICPV) 'Smart Window' system. *Applied Energy*, **2016**, *182*, 331–339. https://doi.org/10.1016/j.apenergy.2016.07.125

[38] Y. Wu, K. Connelly, Y. Liu, et al. Smart solar concentrators for building integrated photovoltaic façades. *Solar Energy*, **2016**, *133*, 111–118. https://doi.org/10.1016/j.solener.2016.03.046

Journal of Umm Al-Qura University for Applied Science 6 (2020) 21-24

Journal of Umm Al-Qura University for Applied Science

journal homepage: https://uqu.edu.sa/en/jas/87823

Effect of Fast Neutron Irradiation on Optical Properties of Lead Borate Glass

Y. A. El-Gammam [a].

[a] *Department of physics, Common first year deanship, Umm al-Qura University.*

ARTICLE INFO

Article History:
Submission date: 6/9/2019
Accepted date: 5/12/2019

Keywords:
Fast neutron irradiation, Lead borate glass, optical properties, samarium oxide.

ABSTRACT

Lead borate glass samples in the system $50B_2O_3$-$45PbO$-$5Al_2O_3$-$(100-x)$ Sm_2O_3, where x = 0, 0.42, 0.85, 1.7, 2.5 and 4.1 mole%, were prepared using the normal melt quench technique. The effect of fast neutron irradiation on optical properties of the prepared glasses was examined by measuring their optical density. The compositional dependence of the optical density, were measured and then were used to calculate and discuss some optical parameters such as: absorption coefficient (α), direct and indirect optical energy gap (E_{ogd} and E_{ogind}), Urbach's energy (E_u), Fermi energy (E_f), and steepness parameter (S). From the calculated optical parameters, it was found that E_f and E_u increase while E_{ogd} and E_{ogind} decrease with increasing neutron irradiation dose. Furthermore, the dependence of aforementioned parameters on the samarium oxide (Sm_2O_3) concentration has been interpreted on the light of band structure transition theory due to Sm^{+3} ions.

1. Introduction

Recently, interest in radiation effects on glass, generally, has been renewed as glass and used in different technology applications. Rare-earth doped glasses have been paid much more attention because of their high potential use for optical applications such as fibers, amplifiers, lasers and sensors [1]. They are also candidates for developing LED devices [2].

B_2O_3, which forms a network structure related to the silicates, creates a glass with higher melting point and greater ability to withstand temperature changes. For these reasons, their higher chemical durability and mechanical strength, borate glasses are often used as a host for Lanthanides ions. However, the emissive properties of Ln ions in this host suffer due to large phonon vibrational energy (~1300 cm^{-1}) [3].

Al_2O_3 has received significant consideration as the most likely matrix composition due to its high solubility of rare-earth ions [4].

Radiation creates a variety of defects in glass, which may be either permanent or temporary [5]. The effect of irradiation on glass is believed to depend on the type and energy of the irradiation, glass composition and sample parameters [6].

Neutron irradiation affects the structure of the glass matrix, resulting in changes in the optical, mechanical, chemical resistance and electrical properties [5–10]. Neutrons being uncharged interact with mater quite differently than the charged particles or the electromagnetic radiation. As neutrons pass through matter, they lose energy by a series of collisions, in scattering or capture events. In scattering process, a neutron collides with a nucleus but because the nucleus is incredibly small, the probability of a collision is low. The most dominant type of collisions is elastic scattering. In this type, a neutron collides with a nucleus and imparts a portion of its energy to the target nucleus. During this elastic scattering, no gamma radiation is given off by the nucleus. This recoil nucleus can cause excitation and ionization events. In the case of inelastic scattering type, the neutron is absorbed by the target nucleus, with a gamma ray and a less energetic neutron emitted from the target. After a neutron has lost a significant portion of its kinetic energy through the scattering events, it may be absorbed by a target nucleus in a capture event. The result of this event is that the new atom has its mass number increased by one, and as such will undergo one of many possible nuclear events. The result is often the emission of ionizing radiations, which result in the production of defects in the material via electron and hole productions [11]. Although neutrons are not directly ionizing radiation, they often produce secondary events that produce various forms of ionizing radiation i.e. radiation damage is not due to neutrons but is mainly from gamma radiation.

When ionizing radiation, such as gamma radiation, impinges on the glass electrons, they are initially excited from the valence band if the incident energy is greater than the band gap. The excess energy is converted to kinetic energy and as these electrons travel through the material, they will either recombine the positively charged holes, becoming trapped to form color centers, or produce a secondary electron cascade by knock-on collision with other bound electrons. Additional bound electrons are ionized by the secondary electrons through Coulomb interactions. The secondaries lose approximately 20 eV for each ionization. Finally, when the electrons energy becomes too low to ionize other electrons, they will either be trapped or recombine with holes. Therefore, in amorphous materials, radiation gives rise to optical absorption bands. These bands are associated with radiation-induced intrinsic and extrinsic defects. Vacancies and self-interstitials cause intrinsic defects. These defects can be introduced by ionization, atomic displacement mechanisms or via the activation of the preexisting defects [12]. Extrinsic defects are related to impurities such as alkali, alkaline earth and transition metals in the glass because they increase radiation- induced defects [13]. Materials which have such defects absorb photons at particular wavelengths, result in a modified absorption spectrum of the materials. The difference between the absorption spectra before and after irradiation is an important characteristic and is called the induced absorption spectrum.

The purpose of this work is to study the optical absorption spectrum of prepared lead borate glasses doped with samarium oxide before and after fast neutrons irradiation, to investigate induced transitions and to get information about the band structure and energy gap of this glass.

2. Experimental procedure

2.1. Preparation of glass samples

Glasses with the molar composition $(B_2O_3)_{50}$ $(PbO)_{45}$ $(Al_2O_3)_5$ $(Sm_2O_3)_x$,where x = 0, 0.42, 0.85, 1.7, 2.5 and 4.1, were prepared using the normal melt quench technique from AR grade chemicals of B_2O_3, PbO, Al_2O_3 and Sm_2O_3 . The composition of the glass samples is shown in Table 1. The chemical patches of every composition were mixed in porcelain crucibles, and then heated at 950°c for two hours under normal atmospheric conditions. The melt was stirred from time to time to promote complete mixing and finally poured into preheated molds made of stainless steel of radius 1.3 cm. All samples were properly annealed at 350°c in a muffle furnace to eliminate mechanical and thermal stresses. The samples were highly polished using alpha

* **Corresponding Author**
Department of physics, Common first year deanship, Umm al-Qura University.
E-mail address: yaahmed@uqu.edu.sa (Y. A. El-Gammam).

alumina polishing suspension to obtain optical flatness. The thickness of each sample was measured with micrometer.

The amorphous nature of these glasses was examined using Philips (X'pert MPD) diffractometer while applying the Bragg-Brentano para-focusing technique. Highly monochromated Cu-radiation (wavelength λ= 1.54051Å) was used. The step scan mode was applied in the 2θ-range (4-157.4612°). The step size (Δ2θ= 0.04°) and the counting time was 10 sec. for each reading. The corresponding accessible maximum scattering vector magnitude, K, was 8.0 Å-1. The air scattering was avoided by a suitable applied arrangement of XRD system. The receiving and divergence slits were properly chosen in both small and large 2θ-ranges, in order to improve the qualities of the data collected as it possibly could. The X-ray diffraction spectra of four samples (with x = 0, 0.42, 1.7 and 4.1) showed the diffused bands characteristic of the x-ray diffraction pattern of amorphous materials; the spectra did not show any sharp peaks and confirms that the glass samples are amorphous in nature.

Table 1. Composition of the glass samples

Sample no.	Glass composition (mol %)			
	PbO	B_2O_3	Al_2O_3	Sm_2O_3
Base	45	50	5	-
Sm1	45	50	5	0.42
Sm2	45	50	5	0.85
Sm3	45	50	5	1.7
Sm4	45	50	5	2.5
Sm5	45	50	5	4.1

2.2. UV-visible absorption measurements

The Optical properties of highly polished samples were measured at room temperature before and after each neutron irradiation dose using a UV/VIS spectrophotometer type JASCO, Corp., V–500, Japan, in the wavelength range 190–1100 nm.

2.3. Fast neutron irradiation

Prepared glass samples were irradiated with neutron beam from an Am–Be neutron source of 5 Ci activity, which has a neutron yield of $1.1x10^7$ n s^{-1}. Three irradiation dose of 3.229 $x10^{10}$, 5.045 $x10^{10}$ and $1.7x10^{11}$ n cm^{-2} were used.

3. Results and discussion

The measured UV-visible absorption spectra of the studied glasses are shown in Figure 1. From this figure, optical absorption spectra can be divided into three particular regions. The first region is the weak absorption tail, which originates from defects and impurities in the glass structure. The second region, found in the middle, exhibits exponential absorption edge that is strongly related to the structural randomness of the glass. The last region is the high absorption region that determines the optical energy gap. Study of these regions is a useful method for the investigation of optically induced transitions and for getting information about the band structure and energy gap of materials.

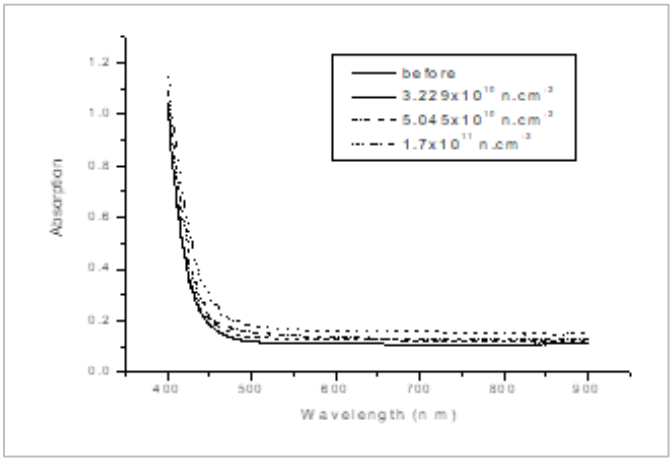

Fig. 1. UV–VIS spectra of sample free from Sm_2O_3 before and after neutron irradiation for 3 doses.

3.1. Glass Fermi energy

It is known that, the imaginary refractive index, *k*, can be represented by Fermi-Dirac distribution function [14]:

$$k = \frac{1}{1 + e^{\left(\frac{E_F - E}{K_B T}\right)}}, \quad (1)$$

where *E* is the energy of the incident photon, *T* is the temperature in Kelvin, E_B is Boltzmann constant and E_F is the Fermi energy. The Fermi energy is defined as the highest occupied energy level when electron configuration is in its ground state. Equation (1) can be written as

$$K_B T \ln(-1) = E_F - E \quad (2)$$

Linear fitting of the last equation is used to determine the glass Fermi energy and presented in Table 2. The calculated fermi energies reveal that E_F increases with increasing neutron irradiation dose.

3.2. Optical band energies

The optical absorption of an optical medium can be quantified in terms of optical density (O.D.), which is sometimes called *absorbance*, *A*. In terms of absorption, *I*, *absorbance* is defined as:

$$A = -\log 10 (I / Io), \quad (3)$$

and according to Beer's law, it can be write:

$$I = I_o e^{-\alpha x}, \quad (4)$$

Where α is the absorption coefficient and can be obtained from the relation

$$\alpha = 2.303 (A / x), \quad (5)$$

where *I* and I_o are optical intensities at thickness *x* and *x* = 0 respectively.

The optical absorption coefficient changes rapidly for photon energies comparable to that of the band gap, E_g [15].

According to Mott and Davis [14], the absorption of light by amorphous solid depends on the photon energy *E* of the incident photon and on the optical gap of the material. It is found that [16] this behavior may be represented by an equation of the form:

$$\alpha E = B (E - E_g)^r \quad (6)$$

where α is the absorption coefficient of the glass material, B is a constant and *r* is an index which assumes the values 1/2, 3/2, 2 and 3 depending on the nature of the electronic transition responsible for the absorption. In the present case *r* is taken equal to 1/2, for allowed direct transition and equal to 2, for allowed indirect transition [17]. The direct optical band gap energy, E_{ogd}, can be obtained by plotting $(\alpha E)^2$ versus the photon energy *E*. The indirect optical band gap energy, E_{ogind}, can be obtained by plotting $(\alpha E)^{1/2}$ versus the photon energy *E* extrapolating the linear portion of the curve to intersect the energy axis. The obtained optical band gap energies for the studied glasses are listed in Table 2. As Shawn in Table (2), one can notice a small decrease in E_{ogd} and E_{ogind} with increasing neutron irradiation dose.

Table 2. Calculated optical parameters of studied glasses doped with different concentrations of Sm_2O_3 irradiated with different neutron doses.

Sample no.	Dose ($n.cm^{-2}$)	E_F (eV)	E_{ogd} (eV)	E_{ogind} (eV)	E_u	*S*
Base	0	5.186	3.293	2.963	0.182	0.142
	$3.229x10^{10}$	5.219	3.225	2.769	0.201	0.128
	$5.045x10^{10}$	5.245	3.219	2.765	0.215	0.120
	$1.7x10^{11}$	5.312	3.153	2.754	0.247	0.105
Sm1	0	5.413	3.223	2.793	0.266	0.097
	$3.229x10^{10}$	5.521	3.159	2.691	0.232	0.111
	$5.045x10^{10}$	5.497	3.175	2.782	0.241	0.107
	$1.7x10^{11}$	5.572	3.091	2.742	0.263	0.098
Sm2	0	5.844	3.187	2.682	0.285	0.091
	$3.229x10^{10}$	5.913	3.149	2.583	0.301	0.086
	$5.045x10^{10}$	5.902	3.112	2.597	0.316	0.082
	$1.7x10^{11}$	6.153	3.045	2.542	0.328	0.079
Sm3	0	6.362	3.193	2.671	0.331	0.078
	$3.229x10^{10}$	6.883	3.091	2.543	0.358	0.072
	$5.045x10^{10}$	7.594	3.093	2.573	0.451	0.057
	$1.7x10^{11}$	7.465	3.066	2.510	0.413	0.063
Sm4	0	6. 272	3.180	2.869	0.312	0.083
	$3.229x10^{10}$	6.299	3.132	2.767	0.354	0.073
	$5.045x10^{10}$	6.382	3.111	2.752	0.371	0.070
	$1.7x10^{11}$	6.571	3.073	2.739	0.405	0.064
Sm5	0	6.123	3.284	2.892	0.22	0.118
	$3.229x10^{10}$	6.153	3.251	2.821	0.263	0.098
	$5.045x10^{10}$	6.234	3.258	2.745	0.243	0.106
	$1.7x10^{11}$	6.417	3.198	2.768	0.301	0.086

3.3. Urbach energy and Steepness parameter

In the exponential region (the middle region) of the absorption dependence on the photon energy curve, the absorption coefficient, α , is given by the relation:

$$\alpha = C \exp(E/\Delta E), \quad (7)$$

where C is a constant, E is the energy of the incident photon and ΔE characterizes the slope of the exponential edge (Urbach's energy, E_u) region and it is the width of the band tails of the localized states. The existence of the long tails of the localized states is attributed to the amorphous nature of the material. To calculate this width, ΔE, of the energy tail, a model proposed by Urbach (1953) can be used:

$$\ln(\alpha) = \ln(C) + (E / \Delta E),$$

$$\text{or} \quad \ln(\alpha) = \ln(C) + (E / Eu), \quad (8)$$

Thus, E_u can be obtained from the linear plot of ln(α) as a function of photon energy. The steepness parameter, S, which characterizes the broadening of the optical absorption edge due to electron-photon or excitation-photon interaction at room temperature, T = 300 °K can be written as [17]:

$$S = K_B T / E_u, \quad (9)$$

The calculated values of E_u and S are listed in table (2). These values reveal that E_u increases, while S decreases with increasing neutron fluence.

3.4. Neutron irradiation effect

From the above results and discussion, it is clear that, the successive neutron irradiation doses caused changes in all optical parameters listed in Table (2). These changes can be attributed to the compositional changes in the glass matrix result from the collision of energetic neutrons with atoms dissipating their energy through the solid. This collisions cause displacement of atoms from their normal positions [18]. The neutron irradiation may also cause densified structural changes in glass or compact state which may refer to some bond angles becoming smaller, change in density and refractive index, and induced color centers. Induced color centers are responsible for induced absorption bands. However, this decrease in the optical band gap may be due to the fact that, in neutron irradiation, the electrons leave their normal positions and move through the glass network [19] that results in redistribution of the electrons in the glass matrix. The increase of Urbach's energy indicates an enhancement of the conduction and valence level electrons to the forbidden energy gap and may causes an increase in the conductivity of the glass due to neutron irradiation.

3.5. Sm_2O_3 concentration effect

From Table (2) it may be noticed that E_{ogd}, E_{ogind} and S decrease with increasing Sm_2O_3 content for the first three samples, then tend to increase with increasing Sm_2O_3 concentration in the other three samples. In contrast, E_F and E_u increase with increasing Sm_2O_3 concentration for the first three samples then tend to decrease with increasing Sm_2O_3 concentration in the other three samples. Figure 2 illustrates the change of E_f with Sm_2O_3 concentration before and after irradiation with 1.7×10^{11} (n.cm^{-2}) dose. These changes can be attributed to the fact that, when an oxide of a multivalent metal is dissolved in a glass, equilibrium is established between the different valence states of the metal. In case of samarium, the 3+ charge state is much more stable than the 2+ charge state [20]. As mentioned above, radiation damage, is not mainly due to the neutrons but due to gamma radiation that is responsible for most of it. Eugenia Malchukova *et al.* [21] suggested that gamma radiation is effective for reducing Sm^{3+} to Sm^{2+} ions. Sm^{2+}/Sm^{3+} ratio estimation demonstrates strong influence of both irradiation dose and dopant content on reduction of Sm^{3+}. In some studies, [21–23] it has been observed that increasing Sm_2O_3 content reveals interesting behavior with the value of 2–3 wt% concentration.

4. Conclusion

From the above study, it is clear that neutron irradiation has considerable effect on the investigated optical parameters of the studied glasses. It was found that the values of E_f and E_u increase while E_{ogd}, E_{ogind} and S decrease with increasing neutron irradiation dose. These changes may be attributed to the structural changes and redistribution of the electrons taking place in the glass matrix due to the collision of energetic neutrons. In addition, increasing Sm_2O_3 concentration affects the optical parameters for the glasses with low samarium content, an opposite trend takes place for the glasses doped with high content of Sm_2O_3 .

Fig. 2. The variation of E_f (eV) with Sm_2O_3 concentration before and after 1.7×10^{11} n.cm^{-2} dose.

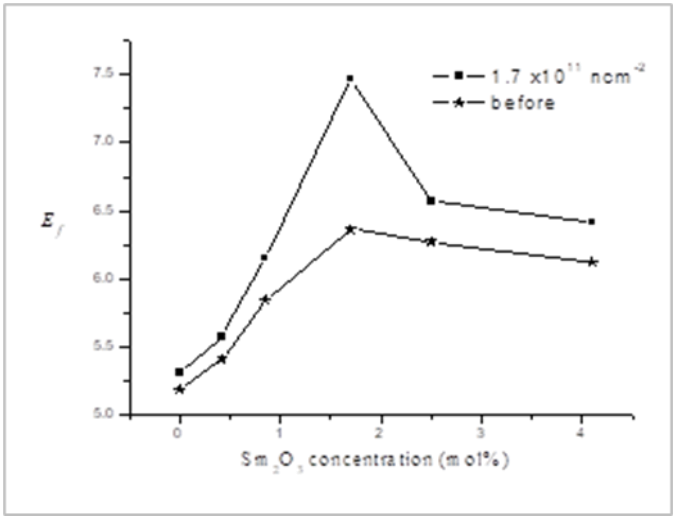

References

[1] M. Nogami, T. Hagiwara, G. Kawamura, E. Ghaith, T. Hayakawa, Redox equilibrium of samarium ions doped in Al_2O_3–SiO_2 glasses. *J. Lumin.*, **2007**, *124*, 291–296. https://doi.org/10.1557/JMR.2002.0304

[2] C. Zhu, X. Liang, Y. Yang, G. Chen, Luminescence properties of Tb doped and Tm/Tb/Sm co-doped glasses for LED applications. *J. Lumin.*, **2010**, *130*, 74–77. https://doi.org/10.1016/j.jlumin.2009.07.023

[3] Y. Dwivedi, A. Bahadur, Spectroscopic study of Sm:Ce ions co-doped in barium fluoroborate glass. *Journal of Non-Crystalline Solids*, **2010**, *356*, 1650–1654. https://doi.org/10.1016/j.jnoncrysol.2010.06.013

[4] K. Arai, H. Namikawa, K. Kumata, T. Honda, Y. Ishii, T. Handa, Aluminum or phosphorus co-doping effects on the fluorescence and structural properties of neodymium-doped silica glass. *J. Appl. Phys.*, **1986**, *59*, 3430. https://doi.org/10.1063/1.336810

[5] N.A. El-Alaily, R.M. Mohamed, Effect of irradiation on some optical properties and density of lithium borate glass. *Mater. Sci. Eng. B.*, **2003**, *98*, 193-203. https://doi.org/10.1016/S0921-5107(02)00587-1

[6] M. Rajaram, E.J. Friebele, Effects of radiation on the properties of low thermal expansion coefficient materials: A review. *J. Non-Cryst. Solids*, **1989**, *108*, 1-17. https://doi.org/10.1016/0022-3093(89)90327-X

[7] H.A. El-Batal, H. Farouk, F.M. Ez-Eldin, Electric and dielectric properties of some gamma-irradiated cabal glasses. *Radiat. Phys. Chem.*, **1996**, *47*, 811-814. https://doi.org/10.1016/0969-806X(95)00168-W

[8] H.A. El-Batal, F.A. Khalifa, M.A. Azooz, Gamma ray interaction, crystallization and infrared absorption spectra of some glasses and glass-ceramics from the system $Li_2O.B_2O_3.Al_2O_3$, *Ind. J. Pure Appl. Phys.*, **2001**, *39*, 565-573. http://nopr.niscair.res.in/handle/123456789/26685

[9] Z.A. El-Hadi, Gamma Ray Interaction with Some High-Lead Glasses Containing Chromium Ions. *J. Solid State Chem.*, **2002**, *163*, 351-363. https://doi.org/10.1006/jssc.2001.9290

[10] M.I. Abd El-Ati, A.A. Higazy, Electrical conductivity and optical properties of gamma-irradiated niobium phosphate glasses. *J. Mater. Sci.*, **2000**, *35*, 6175-6180. https://doi.org/10.1023/A:1026768925365

[11] A.K. Sandhu, Surinder Singh, O. P. *Pandey / Materials Chemistry and Physics*, **2009**, *115*, 783–788.

[12] A. Agrawal, M. Tomazawa, Correlation of silica glass properties with the infrared spectra. *J. Non-Cryst. Solids*, **1997**, *209*, 166-174. https://doi.org/10.1016/S0022-3093(96)00542-X

[13] E.J. Friebele, M.E. Gingerich, K.J. Long, Appl. Opt. 21 (1982) 547.

[14] N.F. Mott, E.A. Davis, Electronic Processes in Noncrystalline Materials, Clarendon, Oxford, **1971**.

[15] S.R. Elliott, in: R.W. Cahn, P. Haasen, E.J. Kramer (Eds.), Materials Science and Technology: Glasses and Amorphous Materials, vol. 9, **1991**, p. 420, Published jointly by VCH, Weinheim Germany, and New York, USA.

[16] S. Hasegawa, S. Yazaki, T. Shimizuol, Effects of annealing on gap states in amorphous Si films. *Solid State Commun*., **1978**, *26*, 407-410. https://doi.org/10.1016/0038-1098(78)90515-X

[17] T. C Sabari Girisun and S. Dhanuskodi, Linear and nonlinear optical properties of tris thiourea zinc sulphate single crystals. *Crst. Res. Technol*., **2009**, *44*, 1297-1302. https://doi.org/10.1002/crat.200900351

[18] W. Primak, L.H. Fuchs, R. Day, Effects of Nuclear Reactor Exposure on Some Properties of Vitreous Silica and Quartz. *J. Am. Ceram. Soc.*, **1955**, *38*, 135-139. https://doi.org/10.1111/j.1151-2916.1955.tb14916.x

[19] S. Singh, A. K. Sandhu, S. Prasher, O. P. Pandey, Effect of neutron irradiation on etching, optical and structural properties of microscopic glass slide used as a solid state nuclear track detector. *Radiation Measurements*, 2007, *42*, 1328 – 1331. https://doi.org/10.1016/j.radmeas.2007.02.057

[20] A. Osvet, S. Emelianova, R. Weissmann, V. I. Arbuzov, A. Winnacker. Spectral hole burning in Sm^{2+}-doped alkaliborate glasses and Tb^{3+}-doped silicate and borate glasses. *J. Lumin.*, 2000, *86*, 323-332. https://doi.org/10.1016/S0022-2313(00)00176-9

[21] E. Malchukova, B. Boizot, D. Ghaleb, G. Petite. Optical properties of pristine and γ-irradiated Sm doped borosilicate glasses. *Nuclear Instruments and Methods in Physics Research A*, 2005, *537*, 411–414. https://doi.org/10.1016/j.nima.2004.08.054

[22] E. Malchukova, B. Boizot, G. Petite, D. Ghaleb, Optical properties and valence state of Sm ions in aluminoborosilicate glass under β-irradiation. *J. Non-Crystalline Solids*, 2007, *353*, 2397–2402. https://doi.org/10.1016/j.jnoncrysol.2007.04.003

[23] N. Yaru, L. Chunhua, Z. Yan, Z. Qitu, X. Zhngzi. Study on Optical Properties and Structure of Sm_2O_3 Doped Boron-Aluminosilicate Glass. *J. Rare Earths*, 2007, *25*, 94-98. https://doi.org/10.1016/S1002-0721(07)60532-8

Journal of Umm Al-Qura University for Applied Science 6 (2020) 25-34

Journal of Umm Al-Qura University for Applied Science

journal homepage: https://uqu.edu.sa/en/jas/87823

Quantum Mechanical Stark Broadening for Na VII and Na VIII lines

Haykel Elabidi [a,b].

[a] *Common First Year Deanship, Physics Department, Umm Al-Qura University, Makkah, Saudi Arabia.*
[b] *Laboratory of Molecular Spectroscopy and Dynamics, Sciences Faculty of Bizerte, Carthage University, Tunisia.*

ARTICLE INFO

Article History:
Submission date: 16/9/2019
Accepted date: 22/6/2020

Keywords:
line profiles, atomic data, scattering

ABSTRACT

We theoretically investigated the structure, the collisional and the Stark broadening problems of the two ions Na VII and Na VIII. We used our quantum mechanical method to calculate new electron impact widths for 20 Na VII and 20 Na VIII spectral lines. No line widths for the two ions have been found in the literature, so no comparisons have been done for this part. Results are provided for electron density $N_e = 10^{17}$ cm^{-3} and for electron temperatures from 2×10^5 K to 10^6 K. We also calculate the radiative and the collisional atomic data. These intermediate results are used for the evaluation of the line broadening, and consequently, their examination are primordial for testing our line broadening accuracy. We extensively compared all of our intermediate results with several theoretical and experimental ones. We found in general acceptable agreements between them, which could guarantee the precision of our line broadening calculations since there are no comparisons for them. The presented data are useful for the diagnostics and modelling of laboratory and astrophysical plasmas.

1. Introduction

Atomic data represent an important tool in the diagnostics of the physical properties of plasmas such as temperature and density, and for the interpretation of astronomical spectra. For instance, the Einstein coefficients are calculated in several kinetic processes using radiative decay rates. Radiative decay rates are also used in the evaluation of lifetimes which are measurable quantities. In many works [1], the authors calculated oscillator strengths to include in their models radiative and collisional bound-bound transitions. Another particular use of energy levels is in the Stark broadening evaluation for some methods such as the semiclassical and the semi-empirical ones. Furthermore, the study of the line intensities needs the knowledge of all the excitation/ de-excitation processes contributing to the intensity. Consequently, electron collision strengths are used in the calculations of level population and line intensities. The Stark broadening mechanism is also important in many astrophysical applications. Line broadening data for many ions are missing in the literature, and this lack represents an obstacle for the analysis by means of NLTE model atmospheres. These techniques have been quickly developed and improved so that we can not fulfill their need to the atomic data. On the other side, atomic data and Stark broadening tables of many ions are missing. The lack of line broadening data is noteworthy for heavy and highly charged ions, furthermore, when the data are not calculated for suitable temperatures, the abundance determination will not be sufficiently accurate. To use these data correctly, they should be extrapolated to the desired temperatures. That extrapolation procedure causes also an inaccuracy in the abundance determination, because the relation between line widths and temperature is not well established. In some cases, it is necessary to calculate the line broadening of a large number of species (atoms and their ions). This occurs when calculating the opacity and radiative transfer [2,3]. Recently, it has been shown that we need models that include the opacities of heavy element to analyze white dwarf atmospheres [4]. It has been shown also that Stark broadening contribution dominates that of the Doppler one.

The two ions studied in the present work are the boron-like Na VII and the beryllium-like Na VIII. B-like ions are very important for modelling of astrophysical and laboratory plasmas. Their lines have been observed and studied in the seventeens [5-8]. Recently, many extensive calculations for structure and radiative data have been performed. In the newest work, the multiconfiguration Dirac–Fock (MCDF) method including QED corrections has been applied on many isoelectronic sequence (including B-like) of the ions Nd, Sm, Gd, Dy, Er, and Yb [9]. Another extensive calculations for the Be-like ($Z = 4 - 12$) to the Ne-like ($Z = 10 - 24$) sequences including the Boron isoelectronic one have been performed by Froese Fischer & Tachiev [10]. For the Na VII ion, Jönsson *et al.* [11] have recently presented relativistic configuration interaction (RCI) calculations of lifetimes, energy levels, wavelengths, transitions probabilities, oscillator strengths and relative intensities of lines. Their calculations are based on multiconfiguration Dirac–Hartree–Fock (MCDHF) wave functions. They performed also an extensive comparisons with the available results. A detailed list of the earlier works dedicated to the atomic calculations of B-like ions and specially to the Na VII ion can be found in Jönsson *et al.* [11]. Be-like ions are also of interest in laboratory and astrophysical plasmas because they emit in wide range of wavelengths. Their lines have been observed in solar atmosphere and stellar planetary nebulae. The most complete systematic structure calculations for the beryllium isoelectronic sequence ($10 \leq Z \leq 30$) has been performed by Wang *et al.* [12]. Many other works have been published before but including only configurations with $n \leq 2$ [13-17], and other works where the used configurations include up to $n = 3$ [10,18,19]. In another report [15], the authors have taken into account configurations with n up to 5. The collision problem for B-like ions with atomic number Z from 8 to 92 has been treated in the frame of the relativistic distorted wave approximation [20], where collision strengths and oscillator strengths have been calculated for transitions involving only levels with the same principal quantum number $n = 2$. The same method [20] has been applied on the Be-like ions with $8 \leq Z \leq 92$ [21]. R-matrix calculations for excitation collision strengths have been carried out for B-like ions from carbon to Krypton [22], and for Be-like ions from Boron to Zinc [23]. In the two last works, the results have been presented as effective collision strengths Υ (collision strengths averaged over the Maxwellian energy distribution). In spite of the importance of the two ions studied here, and even though their radiative atomic and collisional data exist, experimental and theoretical Stark broadening data are totally missing.

The atomic data are evaluated in the present work using the SUPERSTRUCTURE code (SST) [24]. The collision part is carried out using the two UCL codes DISTORTED WAVE (DW) [25] and JAJOM [26,27]. A short description of the codes will be given hereafter. We use here our quantum mechanical approach for the Stark broadening calculations. The quantum mechanical expression calculating electron impact broadening has been obtained by Elabidi *et al.* [28,29]. The expression is established in intermediate coupling for the atomic structure and under the impact approximation. We have applied this approach for Be-like ions from carbon to neon [29]. Stark broadening of the Li-like ions from carbon to phosphorus has been

studied [30], where in addition, the influence of fine structure effects on line broadening has been investigated. We have also used our method to investigate some regularities of line widths [31]. Elabidi *et al.* [32] studied the strong collisions and their contributions to line broadening. Quantum Stark broadening data of Ar VII lines have been provided by Aloui *et al.*[33], where extensive analysis and comparisons with semiclassical results have been performed interpreting some discrepancies found between the two approaches. Using our method and a fitting procedure applied on the two ions Ar V and Ar VI, we have proposed a temperature dependence of line widths [34]. We have used an analogous fitting method applied on some N-like ions from sodium to silicon to establish a density dependence of line widths [35]. In another report [36], new Stark broadening data of Ar VIII and Ar IX lines have been provided and the results of Ar VIII have been compared to those of the semiclassical approach [37], and a comparison between the importance of Stark and Doppler broadening in the atmospheric conditions of DO white dwarfs has been performed. In all the above cited works, and in the cases where there are comparisons, our quantum results showed acceptable agreements with the other experimental or theoretical ones. In many other cases, our results are the first to be published and thus contribute to fulfill the lack of line broadening data.

Here we have calculated Stark broadening for 20 Na VII and 20 Na VIII spectral lines. As far as we know, the line widths studied in the present work have not been calculated before. We calculated also all the necessary radiative data (energy levels, lifetimes, radiative decay rates, oscillator strengths and line strengths). We calculated also collision strengths for several electron energies ranging from the excitation threshold region of the corresponding transition to energies far from this threshold. We investigated the convergence of the collision strengths with electron energy. Comparisons have been performed with available results, and acceptable agreements have been found. This conclusion gives us confidence in our intermediate results used in the line broadening calculations. We hope that our work participates with other ones to fill in the lack of line broadening data.

2. Theory

2.1. Atomic structure and radiative data

The SST code starts by calculating the eigenfunctions of the operators L^2, L_z, S^2 and S_z using the Slater state expansion method described by Condon & Shortley [38]. The obtained eigenfunctions are then used to calculate the matrix elements of the non relativistic many–electron Hamiltonian, which provide the term energies and the radiative data between these terms (radiative data in *LS* coupling). The relativistic effects are introduced through the Breit–Pauli Hamiltonian [39], where the same eigenfunctions are used to evaluate the matrix elements of the relativistic operators in the Breit–Pauli Hamiltonian [40,41]. SST takes into account the mass-variation, the one–body Darwin and the two–body fine structure interactions. The two-body non–fine structure effects are neglected. This provides fine structure energy levels (defined by the quantum numbers corresponding to the operators L^2, S^2, J^2 and J_z) and radiative data in intermediate coupling. The calculations include electric dipole/quadripole and magnetic dipole transitions. SST supplies also the term-coupling coefficients (TCC) used in JAJOM code [26,27] to take into account intermediate coupling effects in the collision problem (see next subsection). The radial wave functions are evaluated here within the SST program (there is another option that these functions can be introduced by the user as an input). They are determined by diagonalization of the non relativistic Hamiltonian using orbitals calculated in a scaled Thomas–Fermi–Dirac Amaldi (TFDA) potentials. The potential depends on scaling parameters λ_l that have been obtained by a self–consistent energy minimization on the term energies included in our calculations.

2.2. Electron-ion scattering

The collision strength can be defined as the measure of strength for a binary collision. It contains the information about this collision. It is a dimensionless quantity and is related to the collision cross section σ by the following relationship:

$$\Omega_{if} = \frac{k_i^2 g_i}{\pi a_0^2}\sigma_{if}, \qquad (1)$$

where k_i^2 is the incident electron energy in Ryd and g_i is the statistical weight of the initial level. We can say also that both collision strength and cross section describe the intrinsic probability of collisional excitation and de-excitation in an atomic transition at a particular electron energy, but collision strength is preferred because it is symmetric in the initial and final levels.

The collision study starts by calculating the reactance matrices $\mathfrak{R}$ and collision strengths Ω in *LS* coupling where the distorted wave approximation is assumed. This is done in our work through the code DISTRORTED WAVE [25]. Collision strengths in intermediate coupling, including relativistic effects, are evaluated in the JAJOM code [26,27]. In fact, when the nuclear charge increases and for high ionization stages, the contributions of the relativistic effects become important and hence they have to be taken into account when calculating collision strengths. The basic idea of JAJOM is to transform collision parameters form the *LS* coupling to the intermediate one taking into account these relativistic interactions in the structure study. The adopted procedure in JAJOM consists on calculating, in a first stage, the collision strengths in *LS* coupling from the reactance matrices $\mathfrak{R}^{SL}$ obtained in DISTRORTED WAVE:

$$\Omega(\Gamma_i S_i L_i, \Gamma'_i S'_i L'_i) = \tfrac{1}{2}\textstyle\sum_{SL\pi}\sum_{ll'}(2S+1)(2L+1)|T^{SL\pi}(\Gamma_i S_i L_i ls, \Gamma'_i S'_i L'_i l's)|^2. \qquad (2)$$

T is the transition matrix related to the reactance one by $T = 2i\mathfrak{R}(I - i\mathfrak{R})^{-1}$; I is unit matrix. Capital letters refer to the quantum numbers of the emitter, l and s refer to those of the scattered electron and $\pi = (-1)^{\Sigma l}$ is the parity of the hole system (emitter+electron). Γ is a configuration parameter. In a second step, the reactance matrices $\mathfrak{R}^{SL}$ are transformed into JK coupling schema defined by: L_j+S_j=J_j, J_j+l=K_j, K_j+s=J. The reactance matrices in JK coupling are given by (Saraph 1972)[26]:

$$\mathfrak{R}^{J\pi}(\Gamma_i S_i L_i J_i lK; \Gamma'_i S'_i L'_i J'_i l'K'; \varepsilon) = \textstyle\sum_{SL} C(SLJ; S_i L_i J_i; lK)\mathfrak{R}^{SL\pi}(\Gamma_i S_i L_i ls; \Gamma'_i S'_i L'_i l's; \varepsilon) C(SLJ; S'_i L'_i J'_i; l'K'), \qquad (3)$$

where C are the re-coupling coefficients of Racah (1943) [42]. Finally, the matrices $\mathfrak{R}^{J\pi}$ are then transformed into intermediate coupling $\mathfrak{R}^{IC}$. The last transformation needs the TCC: $f_{J_i}(\Delta_i, \Gamma_i S_i L_i)$ defined in the previous reports [24,26] and obtained in SST:

$$\mathfrak{R}^{IC}(\Delta_i J_i lK, \Delta'_i J'_i l'K') = \textstyle\sum_{S_i L_i}\sum_{S'_i L'_i} f_{J_i}(\Delta_i, \Gamma_i S_i L_i)\mathfrak{R}^{J\pi} f_{J'_i}(\Delta'_i, \Gamma'_i S'_i L'_i J'_i). \qquad (4)$$

The parameters Δ_i replace the set of the quantum numbers $\Gamma_i S_i L_i$. The collision strengths are then obtained from $\mathfrak{R}^{IC}$ in the same way as in (2):

$$\Omega(\Delta_i J_i - \Delta'_i J'_i) = \textstyle\sum_{ll'KK'}\sum_{J\pi}\frac{(2J+1)}{2}\left|T^{J\pi}_{ic}(\Delta_i J_i lK; \Delta'_i J'_i l'K')\right|^2. \qquad (5)$$

During this procedure, it is assumed that the reactance matrices are independent of energy. The obtained parameters will be used later in the line broadening evaluation.

2.3. Line broadening calculations

Our quantum mechanical line broadening method used here is a combination between the line broadening and the collision theories. Our line broadening method has three stages: the structure and collision calculations are the the two first stages and represent the start-up step of the line broadening treatment. In the third stage, the parameters obtained from the two first ones (energy levels, reactance matrices, scattering matrices,..) are adequately arranged and adapted to be used in the line broadening calculations through the codes JAJPOLARI (Dubau, unpublished results) and RtoS (Elabidi & Dubau, unpublished results). JAJPOLARI is a transformed version of JAJOM, it extracts the reactance matrices $\mathfrak{R}$ from JAJOM. These matrices which will be used to calculate the real and imaginary parts of scattering matrices $\mathbb{S}$ through the code RtoS:

$$\mathbb{S} = \frac{I+i\mathfrak{R}}{I-i\mathfrak{R}}, \qquad (6)$$

and

$$Re\ \mathbb{S} = (I-\mathfrak{R}^2)(I+\mathfrak{R}^2)^{-1}, Im\ \mathbb{S} = 2\mathfrak{R}(I+\mathfrak{R}^2)^{-1}. \qquad (7)$$

The original expression of the quantum full width corresponding to a transition $i \longrightarrow f$ under the assumption of the impact approximation has been given by the following equation [43]:

$$W = 2N_e\int_0^\infty vf(v)\left(\textstyle\sum_{i'\neq i}\sigma_{ii'}(v) + \sum_{f'\neq f}\sigma_{ff'}(v) + \int\left|f_i(\theta,v) - f_f(\theta,v)\right|^2 \mathrm{d}\Omega\right)dv, \qquad (8)$$

where N_e is the electron density and v is the velocity of the perturbing electron. σ are the inelastic cross sections connecting the levels i and f involved in the transition to their perturbing ones. The integral over the scattering angle θ represents the elastic part of the collision. $d\Omega$ is the element of solid angle and $f(v)$ is the Maxwellian electron velocity distribution given by:

$$\text{with} \qquad f(v) = 4\pi\left(\frac{m}{2\pi k_B T_e}\right)^{\frac{3}{2}} v^2 \exp\left(-\frac{mv^2}{2k_B T_e}\right); \qquad (9)$$
$$\int f(v)dv = 1,$$

m is the electron mass, T_e the electron temperature and k_B the Boltzmann constant.

The expression of the quantum mechanical full Stark width in intermediate coupling has been derived in the previous reports [28,29]. The principal assumption in our method is the impact approximation:

$$W = \qquad (10)$$
$$2N_e\left(\frac{\hbar}{m}\right)^2\left(\frac{2m\pi}{k_B T_e}\right)^{\frac{1}{2}}\int_0^\infty \Gamma_w(\varepsilon)\exp\left(-\frac{\varepsilon}{k_B T_e}\right)d\left(\frac{\varepsilon}{k_B T_e}\right),$$

where

$$\Gamma_w(\varepsilon) = \sum_{J_i^T J_f^T l K_i K_f} \frac{[K_i,K_f,J_i^T,J_f^T]}{2}\begin{Bmatrix} J_i & K_i & l \\ K_f & J_f & 1\end{Bmatrix}^2\begin{Bmatrix} K_i & J_i^T & s \\ J_f^T & K_f & 1\end{Bmatrix}^2 \qquad (11)$$
$$\times\left[1-\left(\mathrm{Re}\,(\mathbb{S}_i)\mathrm{Re}\,(\mathbb{S}_f)+\mathrm{Im}\,(\mathbb{S}_i)\mathrm{Im}\,(\mathbb{S}_f)\right)\right].$$

Uppercase letters refer to the quantum operators of the emitter (the considered ion), the lowercase ones refer to those of the incident electron and letters with the superscript T are the operators of the emitter+electron system. $\mathrm{Re}\,(\mathbb{S})$ and $\mathrm{Im}\,(\mathbb{S})$ are the real and the imaginary parts of the scattering matrix which are expressed in the intermediate coupling schema. The terms in braces represent the 6–j symbols and the notation $[K_i,K_f,J_i^T,J_f^T]$ means $(2K_i+1)\times(2K_f+1)\times(2J_i^T+1)\times(2J_f^T+1)$. The scattering matrices $\mathbb{S}$ and their real and imaginary parts calculated in RtoS are arranged in an adequate order as input data suitable for the formula (11). Finally, we obtain the line width when the sum in (11) and the integral in (10) are performed.

3. Results and discussions

3.1. Atomic structure and collision data

We recall that the lifetime τ for a level j is given by:

$$\tau_j = \frac{1}{\sum_i A_{ji}} \qquad (12)$$

where A_{ji} is the radiative decay rates from the level j to all the possible lower levels i. The radiative decay rates and the absorption oscillator strengths are related to the line strength $S^{[E1]}$ for electric dipole transitions by:

$$\text{and } A_{ji} = 2.6774\times10^9\frac{(\Delta E)^3}{g_j}S^{[E1]}, \qquad (13)$$
$$f_{ij} = \frac{\Delta E}{3g_i}S^{[E1]}, \qquad (14)$$

here $S^{[E1]}$ is expressed in power of Bohr radii a_0 and A_{ji} is given in units inverse to the Rydberg time $\tau_0 = 4.838\times10^{17}$ s. ΔE is the transition energy in Rydbergs and g_i and g_j are the statistical weights of the lower (i) and upper (j) levels, respectively.

For the B-like sodium (Na VII), we have included in the calculations 8 configurations: 1s^2 [2s^{2}2p, 2s2p^2, 2p^3, 2s^{2}3s, 2s^{2}3p, 2s^{2}3d, 2s2p3s, 2s2p3p]. This set of configurations gives rise to 23 terms and 45 fine structure levels. The energies of the 45 fine structure levels are presented along with their lifetimes in Tables 1 and 2. Extensive comparisons have been performed for all the data presented here. Energies are compared to the NIST [44] values, to the RCI ones of Jönsson *et al.* [11], and to other relativistic (Koc) results [45]. The averaged agreement is acceptable and doesn't exceed 2 per cent. We note that some of our levels are inverted regarding to those from the database NIST. In almost all these cases, the inversion is between ^{2}D$_{3/2}$ and ^{2}D$_{5/2}$ levels. The lifetimes have been compared to the experimental results of Buchet *et al.* [46], Tordoir *et al.*[47] when available, otherwise, they are compared to the relativistic configuration interaction (RCI) results of Jönsson *et al.* [11]. The two comparisons show an agreement of about 20 per cent over all the levels.

Table 1: Our energy levels E in cm^{-1} and lifetimes τ in s for Na VII are compared to the Relativistic Configuration Interaction (RCI) calculations [11], to other relativistic (Koc) results (Koc 2003) [44] and to those of NIST [44] database. Lifetimes are compared also to the experimental results of Buchet *et al.* (1978) [46], Tordoir *et al.* [47]. Levels marked by (∗) are inverted regrading to the NIST ones. aE−b means $a\times10^{-b}$.

Index	Conf.	Level	E	NIST	RCI	Koc	τ	τ_{RCI}	τ_{Koc}	τ_{exp}
1	2s^{2}2p	^{2}P$^o_{1/2}$	0	0	0	0	–	–	–	–
2	2s^{2}2p	^{2}P$^o_{3/2}$	2195.	2134.61	2134	2138	–	–	–	–
3	2s2p^2	^{4}P$_{1/2}$	109481.	114995	114856	114878	–	–	–	–
4	2s2p^2	^{4}P$_{3/2}$	110258.	115728	115572	115618	–	–	–	–
5	2s2p^2	^{4}P$_{5/2}$	111520.	116798	116652	116668	–		–	–
6 *	2s2p^2	^{2}D$_{3/2}$	210887.	205448	205485	205681	6.397E−10	7.146E−10	7.111E−10	6.90E−10
7 *	2s2p^2	^{2}D$_{5/2}$	210918.	205412	205444	205617	6.597E−10	7.384E−10	7.350E−10	7.00E−10
8	2s2p^2	^{2}S$_{1/2}$	269062.	264400	264501	264760	1.303E−10	1.618E−10	1.615E−10	1.55E−10
9	2s2p^2	^{2}P$_{1/2}$	297759.	283869	283975	284147	7.181E−11	8.355E−11	8.335E−11	7.30E−11
10	2s2p^2	^{2}P$_{3/2}$	299236.	285189	285291	285465	7.142E−11	8.311E−11	8.283E−11	–
11	2p^3	^{4}S$^o_{3/2}$	365953.	367308	367189	367240	8.245E−11	9.249E−11	9.242E−11	9.50E−11
12 *	2p^3	^{2}D$^o_{3/2}$	424125.	412311	412321	412533	2.355E−10	2.859E−10	2.856E−10	–
13*	2p^3	^{2}D$^o_{5/2}$	424175.	412395	412407	412641	2.346E−10	2.850E−10	2.852E−10	2.80E−10

Table 2: Same as in Table 1 but without experiemntal lifetimes τ.

Index	Conf.	Level	E	NIST	RCI	Koc	τ	τ_{RCI}	τ_{Koc}
14	2p^3	^{2}P$^o_{1/2}$	478851.	465017	465155	465406	9.420E−11	1.162E−10	1.163E−10
15	2p^3	^{2}P$^o_{3/2}$	479005.	465111	465247	465509	9.458E−11	1.167E−10	1.167E−10
16	2s^{2}3s	^{2}S$_{1/2}$	968044.	951350	951183	951067	2.008E−11	2.024E−11	2.027E−11
17	2s^{2}3p	^{2}P$^o_{1/2}$	1027578.	–	1007786	1007696	1.162E−10	2.217E−10	2.244E−10
18	2s^{2}3p	^{2}P$^o_{3/2}$	1028071.	1008420	1008332	1008252	1.155E−10	2.227E−10	2.238E−10
19 *	2s2p(^{3}P)3s	^{4}P$^o_{1/2}$	1073881.	1077270	1077041	1077012	2.757E−11	1.684E−11	1.690E−11
20	2s2p(^{3}P)3s	^{4}P$^o_{3/2}$	1074631.	1078000	1077762	1077755	2.762E−11	1.681E−11	1.692E−11
21	2s2p(^{3}P)3s	^{4}P$^o_{5/2}$	1075911.	1079330	1079074	1079036	2.772E−11	1.674E−11	1.678E−11
22 *	2s^{2}3d	^{2}D$_{3/2}$	1081549.	1060580	1060482	1060463	3.343E−12	3.782E−12	3.778E−12
23	2s^{2}3d	^{2}D$_{5/2}$	1081705.	1060700	1060612	1060592	3.354E−12	3.793E−12	3.793E−12
24	2s2p(^{3}P)3s	^{2}P$^o_{1/2}$	1107474.	1103220	1103068	1103087	2.215E−11	2.249E−11	2.258E−11
25	2s2p(^{3}P)3s	^{2}P$^o_{3/2}$	1108915.	1104620	1104508	1104513	2.190E−11	2.211E−11	2.218E−11
26 *	2s2p(^{3}P)3p	^{4}D$_{1/2}$	1123574.	–	1128784	1128823	1.140E−09	1.042E−10	8.522E−11
27	2s2p(^{3}P)3p	^{4}D$_{3/2}$	1124068.	–	1129158	1129197	1.831E−09	1.500E−10	1.543E−10
28	2s2p(^{3}P)3p	^{4}D$_{5/2}$	1124880.	–	1129813	1129855	4.550E−09	4.708E−09	4.425E−09
29	2s2p(^{3}P)3p	^{4}D$_{7/2}$	1125993.	–	1130955	1130933	4.569E−09	4.682E−09	1.426E−07
30 *	2s2p(^{3}P)3p	^{2}P$_{1/2}$	1130928.	1126810	1126639	1126672	1.182E−11	1.120E−11	1.145E−11
31	2s2p(^{3}P)3p	^{2}P$_{3/2}$	1131222.	1127430	1127284	1127330	1.301E−11	1.094E−11	1.089E−11
32	2s2p(^{3}P)3p	^{4}S$_{3/2}$	1133377.	–	1140057	1140089	1.281E−10	1.689E−09	1.619E−09
33	2s2p(^{3}P)3p	^{4}P$_{1/2}$	1145469.	–	1147812	1147867	1.451E−09	1.389E−09	1.382E−09
34	2s2p(^{3}P)3p	^{4}P$_{3/2}$	1145988.	–	1148361	1148413	1.485E−09	1.372E−09	1.364E−09
35	2s2p(^{3}P)3p	^{4}P$_{5/2}$	1146726.	–	1149037	1149084	1.286E−09	1.020E−09	1.091E−09
36	2s2p(^{3}P)3p	^{2}D$_{3/2}$	1156419.	1154780	1154694	1154774	9.707E−12	9.812E−12	9.802E−12
37	2s2p(^{3}P)3p	^{2}D$_{5/2}$	1157737.	1156180	1156079	1156142	9.677E−12	9.833E−12	9.809E−12
38	2s2p(^{3}P)3p	^{2}S$_{1/2}$	1174037.	1172340	1172268	1172334	8.178E−12	9.622E−12	9.611E−12
39	2s2p(^{1}P)3s	^{2}P$^o_{1/2}$	1212639.	1198290	1198244	1198340	1.957E−11	1.062E−11	1.067E−11
40	2s2p(^{1}P)3s	^{2}P$^o_{3/2}$	1212762.	1198290	1198282	1198372	1.983E−11	1.046E−11	3.980E−11
41	2s2p(^{1}P)3p	^{2}D$_{3/2}$	1265078.	1251670	1251929	1252070	8.401E−11	6.156E−11	8.552E−11
42	2s2p(^{1}P)3p	^{2}D$_{5/2}$	1265315.	1252010	1252084	1252215	8.219E−11	6.131E−11	5.133E−09
43	2s2p(^{1}P)3p	^{2}P$_{1/2}$	1268598.	1253350	1253401	1253544	1.690E−11	1.957E−11	3.830E−11
44	2s2p(^{1}P)3p	^{2}P$_{3/2}$	1269044.	1253780	1253800	1253937	1.677E−11	1.957E−11	1.212E−10
45	2s2p(^{1}P)3p	^{2}S$_{1/2}$	1284069.	1258880	1258410	1259323	5.128E−11	1.963E−11	5.661E−11

The radiative data (radiative decay rates, oscillator strengths and line strengths) are presented in Table 3 and compared to the RCI Jönsson *et al.* [11], to the MCHF [10] and to the NIST [44] results. We remark that the agreements are better for transitions involving lower levels ($i \leq 16$) than those involving higher levels.

Table 3: Present Na VII radiative decay rates (A_{ij}) and weighted oscillator strengths (gf) including the first 20 levels compared to the RCI results [11] and to the MCHF ones [10]. Transitions with A_{ij} above 10^6 s $^{-1}$ are presented.

		A_{ij} (s^{-1})			gf		S	
Trans.	Present	RCI	NIST	Present	RCI	NIST	Present	MCHF
6 −1	1.331E+09	1.193E+09	1.170E+09	1.794E−01	1.694E−01	1.667E−01	0.28011	0.27100
6 −2	2.325E+08	2.065E+08	2.040E+08	3.202E−02	2.994E−02	2.951E−02	0.05051	0.04816
7 −2	1.516E+09	1.354E+09	1.330E+09	3.130E−01	2.946E−01	2.904E−01	0.49371	0.47690
8 −1	2.961E+09	2.542E+09	2.520E+09	1.226E−01	1.089E−01	1.079E−01	0.15005	0.13560
8 −2	4.714E+09	3.638E+09	3.700E+09	1.985E−01	1.584E−01	1.611E−01	0.24485	0.19830
9 −1	8.878E+09	7.499E+09	7.410E+09	3.003E−01	2.787E−01	2.761E−01	0.33197	0.32290
9 −2	5.047E+09	4.470E+09	4.230E+09	1.732E−01	1.687E−01	1.596E−01	0.19296	0.19750
10 −1	2.315E+09	1.986E+09	2.030E+09	1.550E−01	1.463E−01	1.496E−01	0.17058	0.16880
10 −2	1.169E+10	1.005E+10	9.880E+09	7.943E−01	7.512E−01	7.396E−01	0.88036	0.87270
10 −3	2.052E+09	1.829E+09	1.840E+09	1.871E−01	1.722E−01	1.734E−01	0.24015	0.22430
11 −4	4.067E+09	3.624E+09	3.640E+09	3.730E−01	3.432E−01	3.451E−01	0.48026	0.44850
11 −5	6.010E+09	5.359E+09	5.390E+09	5.568E−01	5.119E−01	5.152E−01	0.72042	0.67260
12 −6	3.087E+09	2.509E+09	2.710E+09	4.072E−01	3.512E−01	5.689E−01	0.62865	0.55820
12 −7	4.170E+08	3.360E+08	2.100E+08	5.502E−02	4.703E−02	4.436E−02	0.08495	0.07473
12 −9	6.325E+08	5.543E+08	6.170E+08	2.375E−01	2.014E−01	3.436E−01	0.61884	0.51590
12 −10	1.041E+08	9.337E+07	9.290E+07	4.002E−02	3.463E−02	3.715E−02	0.10550	0.08962
13 −6	2.563E+08	2.091E+08	3.380E+08	5.068E−02	4.396E−02	4.732E−02	0.07823	0.06980
13 −7	3.298E+09	2.677E+09	2.500E+09	6.523E−01	5.624E−01	3.556E−01	1.00694	0.89420
13 −10	7.074E+08	6.224E+08	6.170E+08	4.077E−01	3.468E−01	3.436E−01	1.07422	0.89800
14 −6	6.252E+09	5.026E+09	5.060E+09	2.611E−01	2.235E−01	2.254E−01	0.32074	0.28310
14 −8	8.870E+08	6.846E+08	6.920E+08	6.043E−02	5.097E−02	5.164E−02	0.09483	0.08324
14 −9	2.392E+09	2.005E+09	2.010E+09	2.187E−01	1.831E−01	1.832E−01	0.39759	0.33260
14 −10	1.085E+09	8.901E+08	8.970E+08	1.009E−01	8.247E−02	8.318E−02	0.18485	0.15080
15−6	6.843E+08	5.459E+08	5.470E+08	5.708E−02	4.851E−02	4.875E−02	0.07009	0.06133
15−7	5.422E+09	4.356E+09	4.390E+09	4.524E−01	3.869E−01	3.908E−01	0.55558	0.48990
15 −8	1.124E+09	9.413E+08	9.310E+08	1.529E−01	1.400E−01	1.387E−01	0.23983	0.22950
15 −9	4.638E+08	3.602E+08	3.700E+08	8.467E−02	6.571E−02	6.761E−02	0.15379	0.11920
15 −10	2.878E+09	2.366E+09	2.380E+09	5.341E−01	4.380E−01	4.395E−01	0.97817	0.80050
16−1	1.641E+10	1.639E+10	1.640E+10	5.250E−02	5.433E−02	5.420E−02	0.01786	0.01878
16 −2	3.318E+10	3.301E+10	3.290E+10	1.066E−01	1.099E−01	1.096E−01	0.03635	0.03803
17 −6	8.274E+09	3.609E+09	–	3.720E−02	1.681E−02	–	0.01499	–
17 −16	2.734E+08	2.554E+08	–	2.313E−01	2.390E−01	–	1.27902	–
18 −6	8.382E+08	3.541E+08	–	7.528E−03	3.294E−03	–	0.00303	–
18 −7	7.494E+09	3.213E+09	–	6.730E−02	2.989E−02	–	0.02712	–
18−16	2.797E+08	2.631E+08	–	4.656E−01	4.829E−01	–	2.55328	–
19 −3	6.025E+09	9.923E+09	–	1.942E−02	3.214E−02	–	0.00663	–
19 −4	3.024E+10	4.944E+10	–	9.766E−02	1.604E−01	–	0.03337	–
20 −3	1.500E+10	2.482E+10	–	9.656E−02	1.605E−01	–	0.03294	–
20 −4	4.818E+09	7.879E+09	7.910E+09	3.106E−02	5.103E−02	5.117E−02	0.01061	0.01752
20 −5	1.638E+10	2.678E+10	2.670E+10	1.059E−01	1.738E−01	1.734E−01	0.03619	0.05929

We recapitulate the results of the comparisons in the Table 4, where the three first columns are for the relative errors for the radiative decay rates and the second last ones for oscillator strengths and line strengths:

Table 4: Averaged relative errors for Ar VII radiative data

Method→	RCI	MCHF	NIST	RCI	MCHF
$i-j\downarrow$					
$i \leq 16$	15	14	16	11	11
$i \geq 17$	38	56	28	38	55
All	25	28	19	23	25

where it is shown that for transitions $i-j$ for which $1 \leq i \leq 16$, the relative error between our results and the three approaches is about 15 % for the radiative decay rates and 10 % for the oscillator strengths and line strengths. The agreement becomes less for transitions involving the levels 20 and higher and the relative error (averaged over the the results of the three approaches) reaches 40 %. These levels arise from the configuration 2s2p3s. If we take into account all the transitions presented in Table 3, the averaged agreement is between 20 % and 25 %. In the line broadening calculations (next subsection), we will not consider transitions involving levels arising from the 2s2p3s configuration.

Table 5: Our energy levels (E) in cm $^{-1}$ for Na VIII compared to NIST [44], to the MCHF [10] and to the Many–Body Perturbation Theory (MBPT) approach [12]. Our lifetimes τ are compared to the MCHF [10] and to the MBPT approach [12] .

Index	Conf.	Level	E	NIST	MCHF	MBPT	τ(s)	τ_{MCHF}(s)	τ_{MBPT}(s)
1	2s ^{2}	^{1}S $_0$	0	0	0	0	–	–	–
2	2s2p	^{3}P $^o_0$	126620.	125881	126238.01	125738.9	–	–	–
3	2s2p	^{3}P $^o_1$	127452.	126613	126974.98	126467.2	–	2.183E−05	2.220E−05
4	2s2p	^{3}P $^o_2$	129149.	128219	128587.82	128079.3	–	6.934E+00	7.007E+00
5	2s2p	^{1}P $^o_1$	252488.	243208	243705.76	242685.8	1.976E−10	2.182E−10	2.208E−10
6	2p ^{2}	^{3}P $_0$	331049.	–	328617.11	326963.4	2.700E−10	2.803E−10	2.847E−10
7	2p ^{2}	^{3}P $_1$	331927.	–	329462.71	327806.9	2.682E−10	2.785E−10	2.828E−10
8	2p ^{2}	^{3}P $_2$	333567.	–	330889.08	329220.8	2.652E−10	2.760E−10	2.803E−10
9	2p ^{2}	^{1}D $_2$	369898.	–	362430.49	360243.3	1.485E−09	1.457E−09	1.501E−09
10	2p ^{2}	^{1}S $_0$	460409.	–	447544.50	444922.2	1.347E−10	1.496E−10	1.536E−10
11	2s3s	^{3}S $_1$	1238299.	1239975	1240797.27	1238642.	1.121E−11	1.135E−11	1.145E−11
12	2s3s	^{1}S $_0$	1262669.	1262780	1263577.94	1261224.	2.831E−11	3.546E−11	3.633E−11
13	2s3p	^{1}P $^o_1$	1294165.	1294230	1294894.64	1292685.	4.900E−12	4.936E−12	4.958E−12
14	2s3p	^{3}P $^o_0$	1296268.	–	1297815.73	1295730.	1.010E−09	1.099E−09	1.040E−09
15	2s3p	^{3}P $^o_1$	1296531.	–	1298043.91	1295948.	2.454E−10	3.951E−10	4.139E−10
16	2s3p	^{3}P $^o_2$	1296949.	–	1298451.81	1296359.	9.598E−10	1.034E−09	1.002E−09
17	2s3d	^{3}D $_1$	1327318.	1327230	1327885.95	1325741.	2.516E−12	2.506E−12	2.511E−12
18	2s3d	^{3}D $_2$	1327413.	1327270	1327955.68	1325797.	2.519E−12	2.510E−12	2.515E−12
19	2s3d	^{3}D $_3$	1327554.	1327390	1328078.04	1325934.	2.524E−12	2.516E−12	2.521E−12
20	2s3d	^{1}D $_2$	1351487.	1347740	1348420.34	1345802.	3.827E−12	3.881E−12	3.889E−12

Table 6: Contionued. Levels marked by (+) are evaluated by NIST as "may be not real".

Index	Conf.	Level	E	NIST	MBPT	τ(s)	τ_{MBPT}(s)
21	2p3s	^{3}P $^o_0$	1400160.	1399670	1398104.	1.397E−11	1.521E−11
22	2p3s	^{3}P $^o_1$	1400945.	1400470	1398878.	1.391E−11	1.513E−11
23	2p3s	^{3}P $^o_2$	1402650.	1402200	1400618.	1.381E−11	1.497E−11
24	2p3s	^{1}P $^o_1$	1427627.	1426120	1419970.	1.134E−11	1.265E−11
25	2p3p	^{1}P $_1$	1432513.	1432980	1431483.	7.724E−12	9.352E−12
26 $^+$	2p3p	^{3}D $_1$	1439628.	1439410	1437839.	1.793E−11	1.840E−11
27 $^+$	2p3p	^{3}D $_2$	1440531.	1440260	1438717.	1.830E−11	1.875E−11
28	2p3p	^{3}D $_3$	1442138.	1441880	1440337.	1.816E−11	1.865E−11
29	2p3p	^{3}S $_1$	1452834.	1452400	1450786.	9.445E−12	1.092E−11
30	2p3p	^{3}P $_0$	1461251.	–	1457417.	1.061E−11	1.070E−11
31	2p3p	^{3}P $_1$	1461907.	1459850	1458101.	1.061E−11	1.070E−11
32	2p3p	^{3}P $_2$	1462915.	1460770	1459004.	1.062E−11	1.070E−11
33	2p3d	^{3}F $^o_2$	1467581.	–	1464643.	1.591E−11	6.163E−11
34	2p3d	^{3}F $^o_3$	1469108.	–	1465771.	6.569E−10	7.368E−10
35	2p3d	^{1}D $^o_2$	1469334.	1469150	1467028.	8.991E−12	5.040E−09
36	2p3d	^{3}F $^o_4$	1470388.	–	1467568.	3.202E−09	6.430E−12
37	2p3p	^{1}D $_2$	1481106.	1474580	1472273.	6.571E−12	7.435E−12
38	2p3d	^{3}D $^o_1$	1485631.	1485140	1483407.	2.004E−12	2.089E−12
39	2p3d	^{3}D $^o_2$	1485978.	1485340	1483761.	2.016E−12	2.103E−12
40	2p3d	^{3}D $^o_3$	1486609.	1486080	1484382.	1.999E−12	2.083E−12
41	2p3d	^{3}P $^o_2$	1492779.	1491980	1490287.	3.703E−12	3.874E−12
42	2p3d	^{3}P $^o_1$	1493372.	1492630	1490932.	3.721E−12	3.892E−12
43	2p3d	^{3}P $^o_0$	1493670.	1492980	1491286.	3.744E−12	3.921E−12
44	2p3p	^{1}S $_0$	1511981.	1481510	1497353.	1.834E−11	1.487E−11
45	2p3d	^{1}F $^o_3$	1516888.	1507790	1505345.	1.586E−12	1.776E−12
46	2p3d	^{1}P $^o_1$	1519737.	1513730	1511315.	2.630E−12	3.086E−12
47	2p4s	^{3}S $^o_1$	1649675.	1649480	1647631.	2.688E−11	2.561E−11
48	2p4s	^{1}S $^o_0$	1662154.	1656820	1656380.	2.285E−11	3.161E−11
49	2s4p	^{3}P $^o_0$	1671030.	–	1669537.	7.975E−11	7.487E−11
50	2s4p	^{3}P $^o_1$	1671120.	–	1669609.	7.936E−11	7.213E−11
51	2s4p	^{3}P $^o_2$	1671311.	–	1669794.	8.031E−11	7.547E−11
52	2s4p	^{1}P $^o_1$	1675965.	1673390	1671261.	8.202E−12	9.696E−12
53	2s4d	^{3}D $_1$	1682870.	1683370	1681339.	6.558E−12	6.387E−12
54	2s4d	^{3}D $_2$	1682900.	1683370	1681364.	6.554E−12	6.393E−12
55	2s4d	^{3}D $_3$	1682945.	1683370	1681412.	6.547E−12	6.403E−12
56	2s4d	^{1}D $_2$	1690982.	1689970	1687841.	6.389E−12	8.217E−12

Table 7: Present Na VIII radiative decay rates (A_{ij}) and oscillator strengths (gf) compared to the NIST [44] values taken from Kelleher & Podobedova [48], and to the MBPT results [12]. Only transitions with decay rates above 10^6 s^{-1} are presented.

		A_{ij} (s^{-1})			gf		S	
Trans.	Present	NIST	MBPT	Present	NIST	MBPT	Present	MBPT
5 −1	5.060E+09	4.400E+09	4.528E+09	3.570E−01	3.350E−01	3.450E−01	0.46549	0.46750
6 −3	3.704E+09	3.510E+09	3.512E+09	1.340E−01	1.305E−01	1.307E−01	0.21660	0.21440
7 −2	1.267E+09	1.200E+09	1.200E+09	1.352E−01	1.320E−01	1.319E−01	0.21675	0.21470
7 −3	9.382E+08	8.890E+08	8.899E+08	1.009E−01	9.840E−02	9.852E−02	0.16249	0.16090
7 −4	1.524E+09	1.450E+09	1.445E+09	1.667E−01	1.625E−01	1.626E−01	0.27058	0.26770
8 −3	9.617E+08	9.090E+08	9.099E+08	1.697E−01	1.653E−01	1.655E−01	0.27103	0.26850
8−4	2.809E+09	2.660E+09	2.657E+09	5.039E−01	4.905E−01	4.913E−01	0.81152	0.80320
8 −5	6.681E+08	6.660E+08	6.599E+08	3.633E−01	3.600E−01	3.570E−01	1.01866	0.99900
10 −5	7.425E+09	6.590E+09	6.510E+09	2.575E−01	2.400E−01	2.381E−01	0.44772	0.38720
11 −2	9.863E+09	9.930E+09	9.679E+09	3.590E−02	3.600E−02	3.507E−02	0.01063	0.01036
11−3	2.966E+10	2.980E+10	2.908E+10	1.081E−01	1.083E−01	1.055E−01	0.03204	0.03120
11−4	4.967E+10	4.980E+10	4.858E+10	1.816E−01	1.815E−01	1.768E−01	0.05390	0.05234
12 −5	3.533E+10	2.980E+10	2.753E+10	5.190E−02	4.290E−02	3.969E−02	0.01692	0.01281
13 −1	1.889E+11	1.870E+11	1.911E+11	5.074E−01	5.020E−01	5.132E−01	0.12907	0.13060
13 −9	1.467E+11	1.170E+11	1.007E+10	7.726E−02	6.050E−02	5.195E−02	0.02752	0.01830
13 −12	3.001E+07	3.100E+07	3.092E+07	1.361E−01	1.410E−01	1.403E−01	1.42226	1.46600
14 −11	2.492E+08	–	2.370E+08	1.112E−01	–	1.088E−01	0.63150	0.62670
15−6	2.566E+08	–	2.443E+08	1.238E−03	–	1.168E−03	0.00042	0.00040
15−7	1.800E+08	–	1.736E+08	8.700E−04	–	8.310E−04	0.00030	0.00028
15 −8	2.875E+08	–	2.828E+08	1.394E−03	–	1.358E−03	0.00048	0.00046
15 −11	2.488E+08	–	2.381E+08	3.300E−01	–	3.252E−01	1.86577	1.86700
16−7	2.057E+08	–	1.917E+08	1.656E−03	–	1.529E−03	0.00057	0.00052
16 −8	5.775E+08	–	5.479E+08	4.665E−03	–	4.382E−03	0.00159	0.00149
16 −11	2.583E+08	–	2.453E+08	5.630E−01	–	5.508E−01	3.15998	3.13800
17−2	2.209E+11	2.230E+11	2.214E+11	6.893E−01	6.940E−01	6.898E−01	0.18899	0.18900
17−3	1.655E+11	1.670E+11	1.658E+11	5.171E−01	5.220E−01	5.175E−01	0.14189	0.14190
17 − 4	1.101E+10	1.110E+11	1.104E+10	3.451E−02	3.475E−02	3.453E−02	0.00948	0.00948
18 −3	2.978E+11	3.000E+11	2.983E+11	1.551E+00	1.560E+00	1.551E+00	0.42541	0.42530
18−4	9.909E+10	9.990E+10	9.924E+10	5.173E−01	5.200E−01	5.175E−01	0.14213	0.14210
19 −4	3.961E+11	3.990E+11	3.966E+11	2.895E+00	2.915E+00	2.895E+00	0.79518	0.79460
19 −16	2.893E+07	–	2.611E+07	3.242E−01	–	3.126E−01	3.48731	3.47600
20 − 5	2.611E+11	2.540E+11	2.569E+11	1.621E+00	1.563E+00	1.579E+00	0.48546	0.47070
20−13	1.946E+08	1.630E+08	1.588E+08	4.439E−01	4.260E−01	4.209E−01	2.54941	2.60600
21 −7	7.079E+10	6.920E+10	6.502E+10	9.300E−02	9.030E−02	8.490E−02	0.02866	0.02608
21 −11	7.815E+08	7.500E+08	7.346E+08	4.472E−02	4.410E−02	4.320E−02	0.09097	0.08911
21 −17	1.505E+07	1.040E+07	9.513E+06	4.251E−03	2.979E−03	2.718E−03	0.01921	0.01235
22−6	2.369E+10	2.330E+10	2.185E+10	9.309E−02	9.090E−02	8.534E−02	0.02864	0.02618
22−7	1.759E+10	1.720E+10	1.615E+10	6.921E−02	6.750E−02	6.318E−02	0.02132	0.01940
22 −8	2.973E+10	2.900E+10	2.725E+10	1.174E−01	1.135E−01	1.069E−01	0.03620	0.03286
22 −11	7.907E+08	7.610E+08	7.434E+08	1.344E−01	1.329E−01	1.299E−01	0.27213	0.26660

For the Na VIII ion, we have used 12 configurations: 1s ^{2} [2s ^{2}, 2s2p, 2s3s, 2s3p, 2s3d, 2p3s, 2p3p, 2p3d, 2s4s, 2s4p, 2s4d]. The energy levels are presented in Tables 5 and 6, and compared with NIST [44], with the MCHF [10], with the Relativistic Many–Body [18] results (RMB) and with the Many–Body Perturbation Theory (MBPT) approach [12]. Lifetimes are compared with the MCHF results [10] and with the MBPT ones [12]. The energies agree well with all the other results within 2 %. Our radiative data for Na VIII are presented in Table 7 and they agree better with the other results than those of Na VII. The relative difference is about 8 % for the radiative decay rates and 6 % for the oscillator strengths and line strengths.

Collision strengths in intermediate coupling (between fine structure levels) have been also calculated. We have included in JAJOM partial partial wave of the scattered electron l up to 29. For high l, the collision strengths of allowed transitions have been calculated using the Coulomb–Bethe formulation [49] and for forbidden transitions, it is assumed that collision strengths follow geometric series behaviour with partial wave [50,51]. We present some of our collision strengths in Tables 8 and 9 with the relativistic distorted wave calculations [20] for Na VII and in Tables 10 and 11 some of the Na VIII collision strengths with the relativistic distorted wave calculations [21]. For each ion we divide the results of the collision strengths in two tables depending on whether the values are high ($\Omega > 1$) or low ($\Omega < 1$). This is will be discussed in details in the second paragraph. The calculations have been performed at four incident electron energies; we use the same energies (displayed in Tables 7−10) as in Zhang & Sampson (1992, 1994)[20,21] to perform the comparisons. Zhang & Sampson (1992, 1994) [20,21] included in their work three configurations for each ion: 1s ^{2}2s ^{2}2p, 1s ^{2}2s2p ^{2}, 1s ^{2}2p ^{3} for Na VII and 1s ^{2}2s ^{2}, 1s ^{2}2s2p, 1s ^{2}2p ^{2} for Na VIII. We present also in these tables the relative errors for each transition at each energy.

Even though the averaged agreement –over all the transitions– between our results and those of Zhang & Sampson (1992, 1994) [20,21] is acceptable (11 % for Na VII and 18 for Na VIII), there are some details that have to be discussed. In fact, we note that the behaviour of this agreement for transitions with low collision strengths ($\Omega < 1$) is different from that of transitions with high collision strengths ($\Omega > 1$). So, we divide the two Tables 4 and 5 in two groups of transitions: the first group with low collision strengths ($\Omega < 1$) and the second one with high collision strengths ($\Omega > 1$). This remark and the following discussions are applicable for the two ions. The first group presents an excellent agreement: 5 % with Zhang & Sampson (1994) [20] for Na VII and 11 % with Zhang & Sampson (1992)[21] for Na VIII. Furthermore, the difference between the two results –for almost all transitions of this group– is decreasing with the electron energy (from 10 % to 5 % for Na VII and from 20 % to 8 % for Na VIII). For the second group of transitions, the agreement is worse and the difference is increasing with energy: for Na VII, it increases from 8 % to 56 % with an average of 28 %, and for Na VIII, it increases from 8 % to 79 % with an average of 39 %. Since this behaviour depends on electron energy, and in order to investigate its potential origin, we select two transitions of each ion and for illustration, we

Table 8: Present Na VII collision strengths at four electron energies ε in Ryd compared to the relativistic distorted wave calculations (ZS94) of Zhang & Sampson (1994). E_{ij} is the energy difference of the transition, $\Delta = 100 \times \frac{|\text{Present}-\text{ZS94}|}{\text{ZS94}}$ (%) and "**Avg.**" is the average of Δ values in a column.

Trans.	$\varepsilon_1 = E_{ij} + 11.77$			$\varepsilon_2 = E_{ij} + 24.71$			$\varepsilon_3 = E_{ij} + 47.06$			$\varepsilon_4 = E_{ij} + 82.36$		
$i-j$	Present	ZS94	Δ	Present	ZS94	Δ	Present	ZS94	Δ	Present	ZS94	Δ
1 −2	1.81E−01	1.80E−01	1	1.37E−01	1.40E−01	2	1.20E−01	1.24E−01	3	1.14E−01	1.20E−01	5
1 −3	1.82E−02	1.73E−02	5	8.96E−03	9.13E−03	2	4.00E−03	4.18E−03	5	1.84E−03	1.90E−03	3
1 −4	2.62E−02	2.48E−02	5	1.28E−02	1.30E−02	2	5.59E−03	5.82E−03	4	2.42E−03	2.51E−03	4
1 −5	1.52E−02	1.43E−02	6	7.51E−03	7.38E−03	2	3.23E−03	3.36E−03	4	1.40E−03	1.45E−03	4
1 −7	2.91E−02	2.69E−02	8	1.44E−02	1.41E−02	2	6.34E−03	6.35E−03	0	2.76E−03	2.74E−03	1
1−12	5.45E−03	5.69E−03	4	6.44E−03	6.60E−03	2	7.21E−03	7.41E−03	3	7.61E−03	7.96E−03	5
1 −13	4.15E−03	4.39E−03	6	4.37E−03	4.53E−03	4	4.64E−03	4.83E−03	4	4.81E−03	5.09E−03	6
1 −15	2.84E−03	3.05E−03	7	3.10E−03	3.28E−03	6	3.38E−03	3.58E−03	6	3.55E−03	3.82E−03	8
2−3	1.14E−02	1.08E−02	5	5.62E−03	5.75E−03	2	2.53E−03	2.67E−03	6	1.16E−03	1.26E−03	9
2 −4	3.27E−02	3.09E−02	6	1.59E−02	1.62E−02	2	7.01E−03	7.29E−03	4	3.06E−03	3.18E−03	4
2 −5	7.32E−02	6.94E−02	5	3.58E−02	3.66E−02	2	1.58E−02	1.65E−02	4	6.96E−03	7.35E−03	6
2 −6	2.87E−01	3.10E−01	8	2.85E−01	3.43E−01	20	2.65E−01	3.84E−01	45	3.21E−01	4.26E−01	33
2 −11	1.45E−03	1.84E−03	27	6.70E−04	7.44E−04	11	2.40E−04	2.43E−04	1	4.80E−05	6.35E−05	19
2 −12	5.83E−03	6.17E−03	6	6.24E−03	6.48E−03	4	6.71E−03	6.98E−03	4	6.98E−03	7.39E−03	6
2 −13	1.28E−02	1.34E−02	5	1.46E−02	1.51E−02	3	1.61E−02	1.68E−02	4	1.69E−02	1.80E−02	7
2 −14	3.08E−03	3.28E−03	6	3.83E−03	3.53E−03	4	3.70E−03	3.86E−03	4	3.88E−03	4.12E−03	6
3−4	1.37E−01	1.25E−01	9	6.74E−02	6.57E−02	3	3.48E−02	3.49E−02	0	2.14E−02	2.19E−02	2
3 −5	1.11E−01	1.12E−01	1	1.04E−01	1.07E−01	3	1.04E−01	1.08E−01	4	1.06E−01	1.11E−01	5
3 −6	5.15E−02	4.62E−02	10	2.15E−02	2.07E−02	4	8.11E−03	7.93E−03	2	3.04E−03	2.88E−03	5
3 −7	3.08E−02	2.74E−02	11	1.32E−02	1.27E−02	4	5.15E−03	5.07E−03	2	1.99E−03	1.96E−03	2
3 −8	1.07E−02	9.70E−03	9	3.88E−03	3.85E−03	1	1.26E−03	1.21E−03	4	3.79E−04	3.91E−04	3
3 −9	3.49E−03	2.88E−03	17	1.39E−03	1.30E−03	6	5.37E−04	5.30E−04	1	2.17E−04	2.19E−04	1
3 −10	8.06E−03	7.07E−03	12	3.34E−03	3.27E−03	2	1.29E−03	1.30E−03	1	5.01E−04	5.04E−04	1
3 −12	1.92E−02	1.74E−02	9	9.57E−03	9.11E−03	5	4.14E−03	4.09E−03	1	1.75E−03	1.77E−03	1
3 −13	2.14E−03	1.90E−03	11	1.04E−03	9.90E−04	5	4.49E−04	4.43E−04	1	1.89E−04	1.91E−04	1
3 −14	4.97E−03	4.36E−03	12	2.35E−03	2.25E−03	4	1.01E−03	1.01E−03	0	4.41E−04	4.57E−04	4
3 −15	2.94E−03	2.58E−03	12	1.37E−03	1.31E−03	4	5.77E−04	5.73E−04	1	2.44E−04	2.40E−04	2
4−5	2.90E−01	2.79E−01	4	2.06E−01	2.08E−01	1	1.71E−01	1.76E−01	3	1.58E−01	1.66E−01	5
4 −6	8.02E−02	7.17E−02	11	3.36E−02	3.22E−02	4	1.27E−02	1.25E−02	2	4.79E−03	4.62E−03	4
4 −7	8.47E−02	7.60E−02	10	3.59E−02	3.48E−02	3	1.38E−02	1.36E−02	1	5.26E−03	5.19E−03	1
4 −8	2.05E−02	1.90E−02	7	7.67E−03	7.49E−03	2	2.48E−03	2.40E−03	3	7.39E−04	6.83E−04	8
4 −9	7.60E−03	6.42E−03	16	3.08E−03	2.91E−03	6	1.19E−03	1.16E−03	3	4.73E−03	4.38E−03	7
4 −10	1.62E−02	1.40E−02	14	6.66E−03	6.44E−03	3	2.57E−03	2.57E−03	0	1.00E−03	1.01E−03	1
4 −12	2.56E−02	2.32E−02	9	1.28E−02	1.22E−02	5	5.60E−03	5.58E−03	0	2.42E−03	2.52E−03	4
4 −13	1.68E−02	1.52E−02	10	8.36E−03	7.98E−03	5	3.62E−03	3.59E−03	1	1.54E−03	1.57E−03	2
4 −14	7.48E−03	6.53E−03	13	3.52E−03	3.33E−03	5	1.49E−03	1.46E−03	2	6.31E−04	6.13E−04	3
4 −15	8.98E−03	7.87E−03	12	4.28E−03	4.08E−03	5	1.88E−03	1.86E−03	1	8.56E−04	8.78E−04	3
Avg.			10			4			3			5

Table 9: Continued.

Trans.	$\varepsilon_1 = E_{ij} + 11.77$			$\varepsilon_2 = E_{ij} + 24.71$			$\varepsilon_3 = E_{ij} + 47.06$			$\varepsilon_4 = E_{ij} + 82.36$		
$i-j$	Present	ZS94	Δ	Present	ZS94	Δ	Present	ZS94	Δ	Present	ZS94	Δ
1 −6	1.38E+00	1.52E+00	10	1.47E+00	1.79E+00	22	1.42E+00	2.07E+00	46	1.30E+00	2.32E+00	79
1 −8	6.73E−01	6.69E−01	1	7.46E−01	7.89E−01	6	7.44E−01	9.13E−01	23	6.89E−01	1.03E+00	49
1 −9	1.42E+00	1.47E+00	4	1.61E+00	1.75E+00	9	1.64E+00	2.03E+00	24	1.53E+00	2.31E+00	51
1 −10	7.35E−01	7.58E−01	3	8.27E−01	8.97E−01	8	8.38E−01	1.04E+00	24	7.83E−01	1.18E+00	51
1 −14	4.14E−03	2.18E−03	47	4.11E−03	2.05E−03	50	4.02E−03	1.98E−03	51	3.94E−03	1.95E−03	51
2−7	2.47E+00	2.71E+00	10	2.60E+00	3.17E+00	22	2.49E+00	3.66E+00	47	2.27E+00	4.10E+00	81
2 −8	1.10E+00	1.10E+00	0	1.22E+00	1.30E+00	7	1.21E+00	1.50E+00	24	1.12E+00	1.69E+00	51
2 −9	8.37E−01	8.58E−01	3	9.41E−01	1.02E+00	8	9.55E−01	1.18E+00	24	8.92E−01	1.34E+00	50
2 −10	3.79E+00	3.91E+00	3	4.27E+00	4.64E+00	9	4.34E+00	5.38E+00	24	4.06E+00	6.11E+00	50
3−11	1.10E+00	1.16E+00	5	1.22E+00	1.37E+00	12	1.21E+00	1.58E+00	31	1.12E+00	1.78E+00	59
4−11	2.20E+00	2.31E+00	5	2.44E+00	2.73E+00	12	2.42E+00	3.16E+00	31	2.24E+00	3.56E+00	59
5−11	3.29E+00	3.47E+00	5	3.66E+00	4.09E+00	11	3.64E+00	4.73E+00	23	3.36E+00	5.34E+00	37
Avg.			8			15			31			56

plot their collision strengths as a function of the electron energy. In Fig 1, we plot the Na VII collision strengths for the transitions $2s2p\ ^2{}^2D_{3/2} - 2s\ ^2 2p\ ^2P^o_{1/2}$ (6–1) and $2p^3\ ^4S^o_{3/2} - 2s2p^2\ ^4P_{5/2}$ (5–11), and those of the Na VIII transitions $2s2p\ ^1P^o_1 - 2s^2\ ^1S_0$ (5–1) and $2p^2\ ^3P_2 - 2s2p\ ^3P^o_2$ (8–4). We see that the collision strengths of Zhang & Sampson (1992, 1994)[20,21] do not converge at high energies, in contrast to ours which decrease to converge toward the infinite energy Born limit. This (and the difference in the configurations used in the calculations) maybe the origin of the high disagreement between the two calculations for these transitions.

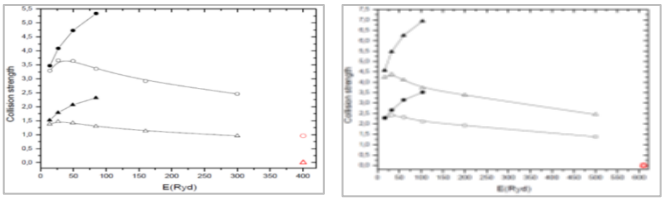

Figure 1: Collision strength Ω as a function of the incident electron energy, open symbols are for the present results. Left: the two Na VII transitions: $2s2p\ ^2{}^2D_{3/2} - 2s\ ^2 2p\ ^2P^o_{1/2}$ (△) and $2p^3\ ^4S^o_{3/2} - 2s2p^2\ ^4P_{5/2}$ (∘), solid symbols: results of ZS94. Right: the two Na VIII transitions: $2p^2\ ^3P_2 - 2s2p\ ^3P^o_2$ (△) and $2s2p\ ^1P^o_1 - 2s^2\ ^1S_0$ (∘), solid symbols: results of ZS92.The two separated points represent the infinite energy Born limit of collision strengths.

Table 10: Same as in Table 7 but for the Na VIII ion. ZS92 is the relativistic distorted wave calculations of Zhang & Sampson (1992). $\Delta = 100 \times \frac{|\text{Present}-\text{ZS92}|}{\text{ZS92}}$ (%).

Trans.	$\varepsilon_1 = E_{ij} + 14.45$			$\varepsilon_2 = E_{ij} + 30.44$			$\varepsilon_3 = E_{ij} + 57.80$			$\varepsilon_4 = E_{ij} + 101.2$		
$i-j$	Present	ZS92	Δ	Present	ZS92	Δ	Present	ZS92	Δ	Present	ZS92	Δ
1 −2	5.80E−03	5.29E−03	9	2.74E−03	2.68E−03	2	1.17E−03	1.18E−03	1	4.98E−04	5.04E−04	1
1 −3	1.75E−02	1.60E−02	9	8.38E−03	8.21E−03	2	3.68E−03	3.73E−03	1	1.69E−03	1.73E−03	2
1 −4	2.89E−02	2.64E−02	9	1.36E−02	1.33E−02	2	5.83E−03	5.87E−03	1	2.48E−03	2.50E−03	1
1 −6	1.82E−04	2.00E−04	10	7.70E−05	7.93E−05	3	2.70E−05	2.73E−05	1	1.00E−05	1.00E−05	0
1 −7	5.36E−04	5.90E−04	10	2.24E−04	2.29E−04	2	7.50E−05	7.37E−05	2	2.30E−05	2.23E−05	3
1 −8	9.02E−04	9.79E−04	9	3.92E−04	3.87E−04	1	1.48E−04	1.33E−04	10	6.30E−05	4.92E−05	22
1 −9	1.61E−02	9.99E−03	38	1.88E−02	1.16E−02	38	2.07E−02	1.29E−02	38	2.15E−02	1.36E−02	37
1 −10	3.33E−03	2.06E−03	38	3.39E−03	2.01E−03	41	3.36E−03	1.98E−03	41	3.31E−03	1.96E−03	41
2−3	5.79E−02	4.97E−02	14	2.53E−02	2.39E−02	6	1.03E−02	9.90E−03	4	4.21E−03	4.11E−03	3
2−4	6.06E−02	5.75E−02	5	5.66E−02	5.50E−02	3	5.68E−02	5.55E−02	2	5.77E−02	5.68E−02	2
2 −5	1.28E−02	1.05E−02	18	5.15E−03	4.71E−03	9	1.91E−03	1.77E−03	7	7.12E−04	6.70E−04	6
2 −6	3.45E−03	3.02E−03	12	1.59E−03	1.52E−03	4	6.68E−04	6.64E−04	1	2.80E−04	2.82E−04	1
2 −8	4.67E−03	4.04E−03	13	2.15E−03	2.02E−03	6	9.04E−04	8.87E−04	2	3.79E−04	3.76E−04	1
2 −9	8.57E−03	7.14E−03	17	3.96E−03	3.58E−03	10	1.66E−03	1.57E−03	5	6.97E−04	6.67E−04	4
2 −10	8.43E−04	6.90E−04	18	3.64E−04	3.29E−04	10	1.44E−04	1.35E−04	6	5.70E−05	5.36E−05	6
3 −4	2.09E−01	1.92E−01	8	1.59E−01	1.54E−01	3	1.41E−01	1.38E−01	2	1.35E−01	1.33E−01	1
3 −5	3.84E−02	3.19E−02	17	1.55E−02	1.40E−02	10	5.76E−03	5.43E−03	6	2.17E−03	2.07E−03	5
3 −9	2.66E−02	2.20E−02	17	1.24E−02	1.11E−02	10	5.24E−03	4.98E−03	5	2.39E−03	2.24E−03	6
3 −10	2.63E−03	2.16E−03	18	1.15E−03	1.04E−03	10	4.70E−04	4.51E−04	4	1.98E−04	2.08E−04	5
4−5	6.43E−02	5.30E−02	18	2.59E−02	2.37E−02	8	9.60E−03	9.03E−03	6	3.59E−03	3.40E−03	5
4 −6	4.14E−03	3.66E−03	12	1.91E−03	1.84E−03	4	8.05E−04	8.04E−04	0	3.38E−04	3.41E−04	1
4 −9	5.03E−02	4.16E−02	17	2.58E−02	2.35E−02	9	1.32E−02	1.36E−02	3	7.66E−03	9.51E−03	24
4 −10	4.62E−03	3.77E−03	18	2.00E−03	1.79E−03	11	7.96E−04	7.41E−04	7	3.15E−04	2.95E−04	6
5−6	5.92E−03	4.90E−03	17	2.89E−03	2.72E−03	6	1.36E−03	1.51E−03	11	7.23E−04	1.01E−03	40
5−7	1.78E−02	1.37E−02	23	7.86E−03	6.93E−03	12	3.24E−03	3.08E−03	5	1.37E−03	1.38E−03	1
6−7	7.38E−02	5.49E−02	26	3.03E−02	2.60E−02	14	1.20E−02	1.10E−02	8	4.85E−03	4.60E−03	5
6−8	6.17E−02	5.83E−02	6	5.49E−02	5.55E−02	1	5.46E−02	5.58E−02	2	5.53E−02	5.70E−02	3
6−9	3.91E−02	2.72E−02	30	1.42E−02	1.20E−02	15	5.03E−03	4.59E−03	9	1.82E−03	1.77E−03	3
6 −10	4.36E−03	3.11E−03	29	1.41E−03	1.19E−03	16	4.13E−04	3.79E−04	8	1.19E−04	1.16E−04	3
7−8	2.31E−01	1.99E−01	14	1.61E−01	1.57E−01	2	1.37E−01	1.38E−01	1	1.30E−01	1.34E−01	3
7−9	1.17E−01	8.22E−02	30	4.35E−02	3.64E−02	16	1.55E−02	1.39E−02	10	5.71E−03	5.34E−03	6
7 −10	1.33E−02	9.48E−03	29	4.29E−03	3.61E−03	16	1.26E−03	1.14E−03	10	3.64E−04	3.42E−04	6
8−9	1.95E−01	1.42E−01	93	7.54E−02	6.29E−02	17	2.74E−02	2.46E−02	10	1.05E−02	9.75E−03	7
8 −10	2.27E−02	1.61E−02	29	7.38E−03	6.18E−03	16	2.24E−03	2.00E−03	11	7.23E−04	6.53E−04	10
9 −10	1.53E−01	1.62E−01	6	1.72E−01	1.83E−01	6	1.89E−01	1.99E−01	5	1.98E−01	2.10E−01	6
Avg.			20			10			7			8

Table 11: Continued.

Trans.	$\varepsilon_1 = E_{ij} + 14.45$			$\varepsilon_2 = E_{ij} + 30.44$			$\varepsilon_3 = E_{ij} + 57.80$			$\varepsilon_4 = E_{ij} + 101.2$		
$i-j$	Present	ZS92	Δ	Present	ZS92	Δ	Present	ZS92	Δ	Present	ZS92	Δ
1 −5	2.27E+00	2.29E+00	1	2.42E+00	2.66E+00	10	2.32E+00	3.15E+00	36	2.11E+00	3.52E+00	67
2 −7	1.13E+00	1.22E+00	8	1.17E+00	1.46E+00	25	1.10E+00	1.67E+00	52	9.94E−01	1.85E+00	86
3 −6	1.13E+00	1.22E+00	8	1.32E+00	1.46E+00	11	1.39E+00	1.67E+00	20	1.34E+00	1.85E+00	38
3−7	8.57E−01	9.23E−01	8	8.82E−01	1.10E+00	25	8.05E−01	1.25E+00	52	7.46E−01	1.39E+00	86
2 −8	1.42E+00	1.53E+00	8	1.46E+00	1.83E+00	25	1.37E+00	2.09E+00	53	1.24E+00	2.32E+00	87
4 −7	1.42E+00	1.53E+00	8	1.46E+00	1.82E+00	25	1.37E+00	2.08E+00	52	1.24E+00	2.31E+00	86
4 −8	4.24E+00	4.57E+00	8	4.38E+00	5.47E+00	25	4.11E+00	6.25E+00	52	3.72E+00	6.94E+00	87
5 −10	1.42E+00	1.53E+00	14	1.46E+00	1.83E+00	30	1.37E+00	2.09E+00	58	1.24E+00	2.32E+00	94
Avg.			8			22			47			79

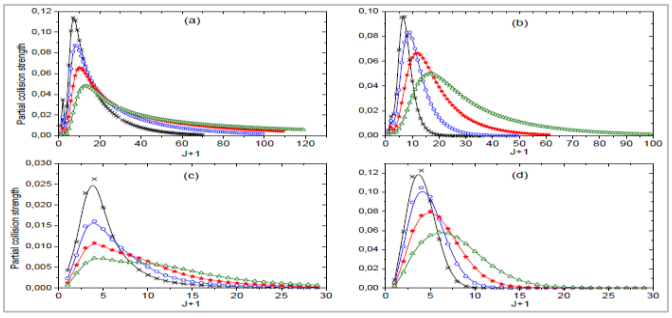

Figure 2: Na VII partial collision strength for the two allowed transitions: 6–1 (a) and 22–1 (b), and for the two forbidden ones: 2–1 (c) and 25–2 (d) at energies 30 Ryd (black-×), 60 Ryd (blue-∘), 120 Ryd (red-⋆) and 240 Ryd (green-△).

Since the collision strengths in intermediate coupling are given by the summation in the equation (5), it is important to ensure that we have included in that summation all the total angular momentum J values that contribute to the collision strengths; i.e. check that the contributions of high J decrease and approximately tend to zero. We have to see also that this convergence is ensured even for high electron energies. We performed this check and the results are displayed in Figs. 2 and 3. In Fig. 2, we present two Na VII allowed transitions $2s2p^2\ {}^2D_{3/2} - 2s\,{}^2 2p\ {}^2P^o_{1/2}$ (a :6–1) and $2s\,{}^2 3d\ {}^2D_{3/2} - 2s\,{}^2 2p\ {}^2P^o_{1/2}$ (b :22–1) and two forbidden ones $2s\,{}^2 2p\ {}^2P^o_{3/2} - 2s\,{}^2 2p\ {}^2P^o_{1/2}$ (c :2–1) and $2s2p(^3P)3s\ {}^2P^o_{3/2} - 2s\,{}^2 2p\ {}^2P^o_{3/2}$ (d :22–2).

We know that, in contrast to the forbidden transitions, the allowed ones do not converge faster with electron energy. We show in Fig. 2 that for the allowed transition (a:6–1), collision strengths converge even for high energy but we have to include higher angular momenta: $J \simeq 40$ at energy $\varepsilon = 30$ Ryd and $J \simeq 120$ at $\varepsilon = 240$ Ryd. The convergence of the allowed transition (b :22–1) is more faster ($J < 90$ at $\varepsilon = 240$ Ryd) because of the high energy difference of the transition (b :22–1): $\Delta_{22-1} \gg \Delta_{6-1}$. The collision strengths of the two forbidden transitions (c :2–1) and (d :22–2) converge very fast at low angular momenta $J = 10 - 20$. Same conclusions can be drawn for the Na VIII results displayed in Fig. 3. The allowed selected transitions are $2s2p\ {}^1P^o_1 - 2s^2\ {}^1S_0$ (a: 5–1), $2s3p\ {}^1P^o_1 - 2s\,{}^2 2p\ {}^2P^o_{1/2}$ (b :13–1) and the forbidden ones are $2s3d\ {}^1D_2 - 2s\,{}^2 2p\ {}^2P^o_{1/2}$ (c :20–1) and $2s3p\ {}^3P^o_2 - 2s\,{}^2 2p\ {}^2P^o_{3/2}$ (d :16–2).

In the light of the above discussions, three important conclusions can be drawn:

Our intermediate results (structural and collisional) agree well with several other calculations and measurements.

Our collision strengths converge for the considered electron energies, even at high energies and for allowed transitions.

The total angular momentum values are sufficiently included, so the collision calculation is complete.

Consequently, we conclude that our intermediate results are sufficiency accurate and complete to be used with confidence in the line broadening calculations.

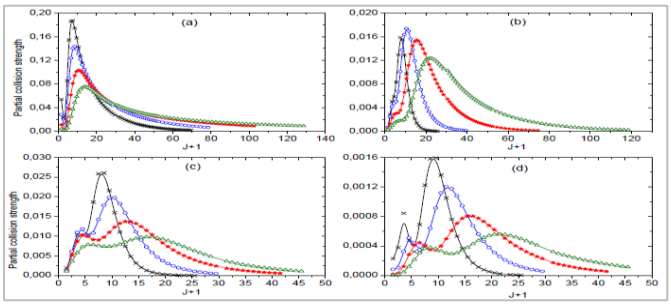

Figure 3: Na VIII partial collision strength for the two allowed transitions: 5–1 (a) and 13–1 (b), and for the two forbidden ones: 20–1 (c) and 16–2 (d) at energies 35 Ryd (black-×), 60 Ryd (blue-∘), 120 Ryd (red-⋆) and 240 Ryd (green-△).

3.2. Stark widths

The method used in the JAJOM code to obtain the reactance matrices in intermediate coupling from those in *LS* coupling has been used long time ago, and it has been shown that it is adequate for ions of interest in our work. This transformation guarantees the introduction of the relativistic effects in the collision calculations. There are two types of relativistic effects [52]:

Corrections due to the motion of the scattered electron and its interaction with the emitter.

Corrections due to the non validity of the *LS* coupling approximation for the emitter.

It has been shown in Walker (1974) [53] that the contributions of the first type of corrections to cross sections do not exceed 10 % for ions with atomic number $Z \leq 25$. Consequently, they can be omitted in the present work. The second type is essential and they have been taken into account in our work. The method used in JAJOM to include these effects is justified by the high velocity of the scattered electrons. In fact, Jones (1974b) [54] showed that, in this case, we can omit the relativistic contribution to the Hamiltonian of the target when studying the collision. Hence, the reactance matrices can be evaluated for *LS* coupling firstly and then, they will be transformed into intermediate coupling using the (TCC) obtained for the atomic structure calculations including the relativistic effects.

We have performed Stark broadening calculations for 20 Na VII and 20 Na VIII lines, displayed respectively in Tables 12 and 13. The results have been presented at electron density $N_e = 10^{17}$ cm $^{-3}$ and for electron temperature ranging from 2×10^5 K to 10^6 K. There are no results in the literature to compare with. The obtained line widths can be useful for astrophysical and laboratory plasma diagnostics. New calculations or measurements of Stark broadeing for these two ions will be welcomed to check our results.

4. Conclusions

We have used in the present paper our quantum mechanical method to provide Stark broadening data for 20 Na VII and 20 Na VIII lines. The results are presented for a large range of electron temperature required for many astrophysical applications. Our method is ab initio, so we have calculated all the parameters needed (structure and collision data) for the line broadening evaluation. Since the accuracy of our line broadening results are related to that of the structure and collision data used in the calculations, it is important to check their accuracy. The structure study has been performed using the SUPERSTRUCTURE code [24]. The energy levels and their lifetimes of Na VII have been compared to the NIST [44] values, to the RCI ones Jönsson *et al.* [11], and to other relativistic (Koc) results [45]. Lifetimes are compared to the experimental values of Buchet *et al.* (1978)[46] and Tordoir *et al.* (1999) [47]. For Na VIII, the energy levels have been compared to the NIST [44], to the MCHF [10], to the Relativistic Many–Body [18] results (RMB) and to the Many–Body Perturbation Theory (MBPT) approach [12]. The agreement is good for the two ions and is less than 2 %. We calculated also radiative decay rates, oscillator strengths and line strengths. Extensive comparisons have been performed with the same references as for the energy levels, and we found an agreement of about 20 % for Na VII and about 7 % for Na VIII. The collision part has been treated using the UCL DISTORTED WAVE [25] and JAJOM [27] codes. We have calculated collision strengths between fine structure levels at four electron energies and we have compared them to the relativistic distorted wave results of Zhang & Sampson (1992, 1994) [20,21]. We found that the averaged agreement for Na VII is about 11 % and about 18 % for Na VIII, but found less agreement for transitions with high collision strengths. We show that for some of these transitions, the results of Zhang & Sampson (1992, 1994) [20,21] do not converge at high energy. This assertion and the difference between the configurations included in our calculations and those used in Zhang & Sampson (1992, 1994) [20,21] may be the origins of the disagreement found exceptionally for these transitions. We investigated also the convergence of our collision strengths with the electron energy, and we show that they converge even for high energies (up to 240 Ryd for Na VII and 300 Ryd for Na VIII). We selected two allowed transitions from each ion to show that their collision strengths converge also but for high total angular momentum J. It is known that collision strengths of this type of transitions do not converge easily with electron energy. The good agreements found between our calculations and all the other results for radiative atomic and collisional data show that our obtained results have high accuracy and hence, our line broadening data can be used with trust. To confirm this conclusion, new measurements or calculations of line widths using other approaches will be welcomed.

Table 12: Stark Widths for 20 Na VII lines at electron density $N_e = 10^{17}$ cm $^{-3}$. T_e is given in 10^5 K.

Transition	T_e	W(pm)	Transition	W(pm)	Transition	W(pm)
	2	1.480−01		6.320−02		1.795−02
$2s2p^2\ ^2D_{3/2} - 2s^2 2p\ ^2P^o_{1/2}$	4	1.097−01	$2p^3\ ^2D^o_{3/2} - 2s2p^2\ ^2P_{1/2}$	4.790−02	$2p^3\ ^2P^o_{3/2} - 2s2p^2\ ^2S_{1/2}$	1.316−02
λ =474.19 Å	6	8.312−02	λ =791.35 Å	4.079−02	λ =476.32 Å	1.109−02
6 −1	8	6.547−02	12−9	3.640−02	15−8	9.855−03
	10	5.337−02		3.329−02		9.002−03
	2	1.204−01		6.499−02		3.691−03
$2s2p^2\ ^2D_{3/2} - 2s^2 2p\ ^2P^o_{3/2}$	4	8.868−02	$2p^3\ ^2D^o_{3/2} - 2s2p^2\ ^2P_{3/2}$	4.922−02	$2s^2 3s\ ^2S_{1/2} - 2s^2 2p\ ^2P^o_{1/2}$	2.620−03
λ =479.17 Å	6	6.731−02	λ =800.71 Å	4.189−02	λ =103.30 Å	2.140−03
6 −2	8	5.321−02	12−10	3.737−02	16−1	1.850−03
	10	4.358−02		3.417−02		1.651−03
	2	9.218−03		6.422−02		3.706−03
$2s2p^2\ ^2S_{1/2} - 2s^2 2p\ ^2P^o_{1/2}$	4	6.953−03	$2p^3\ ^2D^o_{5/2} - 2s2p^2\ ^2P_{3/2}$	4.872−02	$2s^2 3s\ ^2S_{1/2} - 2s^2 2p\ ^2P^o_{3/2}$	2.631−03
λ =371.66 Å	6	5.972−03	λ =800.39 Å	4.151−02	λ =103.54 Å	2.149−03
8 −1	8	5.391E−03	13−10	3.705E−02	16−2	1.858E−03
	10	4.989E−03		3.390E−02		1.658E−03
	2	9.310E−03		1.099E−01		9.404E−03
$2s2p^2\ ^2S_{1/2} - 2s^2 2p\ ^2P^o_{3/2}$	4	7.029E−03	$2p^3\ ^2P^o_{1/2} - 2s2p^2\ ^2D_{3/2}$	7.502E−02	$2s^2 3p\ ^2P^o_{1/2} - 2s2p^2\ ^2D_{3/2}$	5.584E−03
λ =374.72 Å	6	6.042E−03	λ =373.19 Å	5.486E−02	λ =122.45 Å	4.113E−03
8 −2	8	5.457E−03	14−6	4.240E−02	17−6	3.329E−03
	10	5.052E−03		3.412E−02		2.837E−03
	2	7.774E−03		8.719E−02		8.105E−03
$2p^3\ ^4S^o_{3/2} - 2s2p^2\ ^4P^o_{1/2}$	4	5.558E−03	$2p^3\ ^2P^o_{3/2} - 2s2p^2\ ^2D_{3/2}$	5.932E−02	$2s^2 3p\ ^2P^o_{3/2} - 2s2p^2\ ^2D_{3/2}$	4.977E−03
λ =389.91 Å	6	4.602E−03	λ =372.97 Å	4.351E−02	λ =122.37 Å	3.744E−03
11 −3	8	4.034E−03	15−6	3.378E−02	18−6	3.073E−03
	10	3.642E−03		2.735E−02		2.645E−03
	2	7.674E−03		7.595E−02		6.615E−03
$2p^3\ ^4S^o_{3/2} - 2s2p^2\ ^4P^o_{3/2}$	4	5.498E−03	$2p^3\ ^2P^o_{3/2} - 2s2p^2\ ^2D_{5/2}$	5.220E−02	$2s^2 3p\ ^2P^o_{3/2} - 2s2p^2\ ^2D_{5/2}$	4.275E−03
λ =391.09 Å	6	4.559E−03	λ =373.01 Å	3.823E−02	λ =122.38 Å	3.317E−03
11 −4	8	4.002E−03	15−7	2.966E−02	18−7	2.778E−03
	10	3.617E−03		2.403E−02		2.425E−03
	2	7.469E−03		1.802E−02		
$2p^3\ ^4S^o_{3/2} - 2s2p^2\ ^4P^o_{5/2}$	4	5.372E−03	$2p^3\ ^2P^o_{1/2} - 2s2p^2\ ^2S_{1/2}$	1.321E−02		
λ =393.03 Å	6	4.470E−03	λ =476.67 Å	1.113E−02		
11 −5	8	3.933E−03	14−8	9.888E−03		
	10	3.562E−03		9.031E−03		

Table 13: Stark Widths for 20 Na VIII lines at electron density $N_e = 10^{17}$ cm $^{-3}$. T_e is given in 10^5 K.

Transition	T_e	W(pm)	Transition	W(pm)	Transition	W(pm)
	2	1.491E−02		1.627E−03		1.661E−02
2s2p $^1P^o_1 - 2s^2\ ^1S_0$	4	1.099E−02	2s3p $^1P^o_1 - 2s^2\ ^1S_0$	1.147E−03	2s3d $^3D_2 - 2s2p\ ^3P^o_1$	1.105E−02
λ =396.05 Å	6	9.351E−03	λ =77.2 Å	9.356E−04	λ =83.34 Å	8.341E−03
5 −1	8	8.408E−03	13−1	8.095E−04	18−3	6.708E−03
	10	7.767E−03		7.231E−04		5.613E−03
	2	1.341E+00		8.259E−03		1.572E−02
2p $^2\ ^1D_2 - 2s2p\ ^1P^o_1$	4	7.798E−01	2s3p $^1P^o_1 - 2p^2\ ^1D_2$	5.219E−03	2s3d $^3D_2 - 2s2p\ ^3P^o_2$	1.048E−02
λ =851.72 Å	6	5.381E−01	λ =108.19 Å	3.867E−03	λ =83.45 Å	7.930E−03
9 −5	8	4.063E−01	13−9	3.093E−03	18−4	6.393E−03
	10	3.239E−01		2.591E−03		5.360E−03
	2	2.253E−02		4.071E−03		1.232E−02
2p $^2\ ^1S_0 - 2s2p\ ^1P^o_1$	4	1.665E−02	2s3p $^1P^o_1 - 2p^2\ ^1S_0$	2.877E−03	2s3d $^3D_3 - 2s2p\ ^3P^o_2$	8.062E−03
λ =480.95 Å	6	1.422E−02	λ =119.94 Å	2.352E−03	λ =83.44 Å	5.970E−03
10 −5	8	1.281E−02	13−10	2.040E−03	19−4	4.715E−03
	10	1.184E−02		1.826E−03		3.881E−03
	2	2.385E−03		3.147E+00		1.226E−01
2p3s $^3S_1 - 2s2p\ ^3P^o_0$	4	1.693E−03	2s3p $^1P^o_1 - 2s3s\ ^1S_0$	2.519E+00	2p3s $^3P^o_0 - 2s3s\ ^3S_1$	8.614E−02
λ =89.95 Å	6	1.383E−03	λ =119.94 Å	2.172E+00	λ =617.81 Å	6.954E−02
11 −2	8	1.194E−03	13−12	1.934E+00	21−11	5.955E−02
	10	1.062E−03		1.757E+00		5.268E−02
	2	2.387E−03		2.014E−02		6.439E−03
2p3s $^3S_1 - 2s2p\ ^3P^o_1$	4	1.695E−03	2s3d $^3D_1 - 2s2p\ ^3P^o_0$	1.347E−02	2p3s $^1P^o_1 - 2p^2\ ^1D_2$	4.075E−03
λ =90.02 Å	6	1.384E−03	λ =83.28 Å	1.025E−02	λ =94.54 Å	3.043E−03
11 −3	8	1.195E−03	17−2	8.293E−03	24−9	2.456E−03
	10	1.063E−03		6.979E−03		2.075E−03
	2	2.390E−03		2.016E−02		4.438E−03
2p3s $^3S_1 - 2s2p\ ^3P^o_2$	4	1.697E−03	2s3d $^3D_1 - 2s2p\ ^3P^o_1$	1.349E−02	2p3s $^1P^o_1 - 2p^2\ ^1S_0$	3.076E−03
λ =90.16 Å	6	1.387E−03	λ =83.34 Å	1.026E−02	λ =103.39 Å	2.467E−03
11 −4	8	1.197E−03	17−3	8.304E−03	24−10	2.103E−03
	10	1.065E−03		6.988E−03		1.855E−03
	2	3.208E−03		1.685E−02		
2p3s $^1S_0 - 2s2p\ ^1P^o_1$	4	2.276E−03	2s3d $^3D_1 - 2s2p\ ^3P^o_2$	1.128E−02		
λ =98.99 Å	6	1.859E−03	λ =83.46 Å	8.586E−03		
12 −5	8	1.608E−03	17−4	6.960E−03		
	10	1.435E−03		5.867E−03		

Acknowledgments: The author is grateful to Prof. Sylvie Sahal-Bréchot for several fruitful discussions. This work has been supported by the Tunisian Laboratory of Molecular Spectroscopy and Dynamics LR18ES02.

Conflicts of Interest: Declare conflicts of interest or state "The authors declare no conflict of interest."

References

[1] T. Rauch *et al*. Stellar laboratories. IX. New Se V, Sr IV-VII, Te VI, and I VI oscillator strengths and the Se, Sr, Te, and I abundances in the hot white dwarfs G191-B2B and RE 0503-289. *A&A*. **2017**, *606*, A105-132. https://doi.org/10.1051/0004-6361/201730383

[2] M. S. Dimitrijević. Stark broadening in asyrophysics (Applications of Belgrade school results and collaboration with former Soviet republics). *Astronomical & Astrophysical Transactions*. **2003**, *22*, 389-412. https://doi.org/10.1080/1055679031000108167

[3] A. E. Lynas-Gray *et al*. Current State of Astrophysical Opacities : A White Paper. Astronomical Society of the Pacific Conference Series. **2018,** 301-318 (arXiv:1804.06804)

[4] K. Werner, T. Rauch, M. Knörzer and J. W. Kruk. First detection of bromine and antimony in hot stars. *A&A*. **2018,** *614*, A96-100. https://doi.org/10.1051/0004-6361/201832723

[5] D. R. Flower and H. Nussbaumer. On the extreme ultraviolet solar emission of B-like ions: O IV. *A&A*. **1975a**, *45*, 145-150. https://doi.org/10.1051/0004-6361:200811222

[6] D. R. Flower and H. Nussbaumer. On the extreme ultraviolet solar emission of B-like ions: Na VII, Si X and S XII. *A&A*. **1975b**, *45*, 349-352. https://doi.org/10.1051/0004-6361:200811222

[7] D. L. McKenzie, P. B. Landecker, U. Feldman and G. A. Doschek. The solar coronal X-ray spectrum from 5.5 to 12 Å. *ApJ*. **1985**, *289*, 849-857. 10.1086/162949

[8] B. C . Fawcett, K. J. H. Phillips, C. Jordan and J. R. Lemen. New spectral line identifications in high-temperature flares. *MNRAS*. **1987**, *225*, 1013-1023. https://doi.org/10.1093/mnras/225.4.1013

[9] J. P. Marques *et al*. Theoretical determination of K X-ray transition energy and probability values for highly charged (He-through B-like) Nd, Sm, Gd, Dy, Er, and Yb ions. *Radiation Physics and Chemistry*. **2019**, *154*, 17-20. https://doi.org/10.1016/j.radphyschem.2018.02.003

[10] C. Froese Fischer and G. Tachiev. Breit-Pauli energy levels, lifetimes, and transition probabilities for the beryllium-like to neon-like sequences. *At. Data Nucl. Data Tables.* **2004**, *87*, 1-184. https://doi.org/10.1016/j.adt.2004.02.001

[11] P. Jönsson, J. Ekman and E. Träbert. MCDHF Calculations and Beam-Foil EUV Spectra of Boron-Like Sodium Ions (Na VII). *Atoms*. **2015**, *3*, 195-259. https://doi.org/10.3390/atoms3020195

[12] K. Wang *et al*. Systematic calculations of energy of levels and transition rates of be-like ions with Z =10–30 using a combined configuration interaction and many-body perturbation theory approach. *ApJS.* **2015**, *218*, 16-29. https://doi.org/10.1088/0067-0049/218/2/16

[13] A. E. Kingston and A. Hibbert. Breit-Pauli calculations of the energy levels and oscillator strengths of Be-like ions. *J. Phys. B: At. Mol. Opt. Phys.* **2000**, *33*, 693-708. https://doi.org/10.1088/0953-4075/33/4/307

[14] A. E. Kingston and A. Hibbert. Breit-Pauli calculations of the Einstein rate coefficients for magnetic dipole, electric quadrupole and magnetic quadrupole transitions in Be-like ions. *J. Phys. B: At. Mol. Opt. Phys.* **2001**, *34*, 81-98. https://doi.org/10.1088/0953-4075/34/1/307

[15] M. F. Gu. Energies of 1s ^{2}2l ^{q} ($1 \leqslant q \leqslant 8$) states for $Z \leqslant 60$ with a combined configuration interaction and many-body perturbation theory approach. *At. Data Nucl. Data Tables*. **2005a**, *89*, 267-293. https://doi.org/10.1016/j.adt.2005.02.004

[16] M. F. Gu. Wavelengths of 2l-->3l' Transitions in L-Shell Ions of Iron and Nickel: A Combined Configuration Interaction and Many-Body Perturbation Theory Approach. *ApJS.* **2005b**, *156*, 105-110. https://doi.org/10.1086/425915

[17] M. Andersson, Y. Zou, R. Hutton and T. Brage. Hyperfine-dependent lifetimes in Be-like ions. *Phys. Rev. A*. **2009**, *79*, 032501. https://doi.org/10.1103/PhysRevA.79.032501

[18] M. S. Safronova, W. R. Johnson and U. I. Safronova. Relativistic many-body calculations of energies of n = 3 states of Be-like ions. *J. Phys. B: At. Mol. Opt. Phys.* **1997**, *30*, 2375-2393. https://doi.org/10.1088/0953-4075/30/10/012

[19] U. IK. Safronova, A. Derevianko, M. S. Safronova and W. R. Johnson. Relativistic many-body calculations of transition probabilities for the $2l_12l_2$[LSJ]- $2l_33l_4$[L'S'J'] lines in Be-like ions. *J. Phys. B: At. Mol. Opt. Phys.* **1999**, *32*, 3527-3545. https://doi.org/10.1238/Physica.Regular.059a00286

[20] H. L. Zhang and D. H. Sampson. Relativistic Distorted-Wave Collision Strengths and Oscillator Strengths for the 105 Δn = 0 Transitions with n = 2 in the 85 B-Like Ions with 8 <= Z <= 92. *At. Data Nucl. Data Tables.* **1994**, *56*, 41-104. https://doi.org/10.1006/adnd.1994.1002

[21] H. L. Zhang and D. H. Sampson. Relativistic Distorted-Wave Collision Strengths and Oscillator Strengths for the 45 Δn =0 Transitions with n = 2 in the 85 Be-like Ions with 8 <= Z <= 92. *At. Data Nucl. Data Tables*. **1992**, *52*, 143-173. https://doi.org/10.1016/0092-640X(92)90011-6

[22] G. Y. Liang, N. R. Badnell and G. Zhao. R-matrix electron-impact excitation data for the B-like iso-electronic sequence. *A&A.* **2012**, *547*, A87-99. https://doi.org/10.1051/0004-6361/201220277

[23] L. Fernández-Menchero, G. Del Zanna and N. R. Badnel. R-matrix electron-impact excitation data for the Be-like iso-electronic sequence. *A&A.* **2014**, *566*, A104-115. https://doi.org/10.1051/0004-6361/201423864

[24] W. Eissner, M. Jones and H. Nussbaumer. Techniques for the calculation of atomic structures and radiative data including relativistic corrections. *Comput. Phys. Commun.* **1974**, *8*, 270-306. https://doi.org/10.1016/0010-4655(74)90019-8

[25] W. Eissner. The UCL distorted wave code. *Comput. Phys. Commun.* **1998**, *114*, 295-341. https://doi.org/10.1016/S0010-4655(98)00082-4

[26] H. E. Saraph. Fine structure cross sections from reactance matrices. *Comput. Phys. Commun.* **1972**, *3*, 256-268. https://doi.org/10.1016/0010-4655(72)90071-9
[27] H. E. Saraph. Fine structure cross sections from reactance matrices, a more versatile development of the program JAJOM. *Comput. Phys. Commun.* **1978**, *15*, 247-258. https://doi.org/10.1016/0010-4655(78)90095-4
[28] H. Elabidi, N. Ben Nessib and S. Sahal-Bréchot. Quantum mechanical calculations of the electron-impact broadening of spectral lines for intermediate coupling. *J. Phys. B: At. Mol. Opt. Phys.* **2004**, *37*, 63-71. https://doi.org/10.1088/0953-4075/37/1/004
[29] H. Elabidi, N. Bennessib, M. Cornille, J. Dubau and S. Sahal-Bréchot. Electron impact broadening of spectral lines in Be-like ions: quantum calculations. *J. Phys. B: At. Mol. Opt. Phys.* **2008**, *41*, n°025702. https://doi.org/10.1088/0953-4075/41/2/025702
[30] H. Elabidi, N. Ben Nessib and S. Sahal-Bréchot. Quantum Stark broadening of 3s–3p spectral lines in Li-like ions; Z-scaling and comparison with semi-classical perturbation theory. *Eur. Phys. J. D.* **2009**, *54*, 51-64. https://doi.org/10.1140/epjd/e2009-00167-8
[31] H. Elabidi and S. Sahal-Bréchot. Checking the dependence on the upper level ionization potential of electron impact widths using quantum calculations. *Eur. Phys. J. D.* **2011**, *61*, 285-290. https://doi.org/10.1140/epjd/e2010-10298-4
[32] H. Elabidi, S. Sahal-Bréchot and M. S. Dimitrijević. Quantum Stark broadening of Ar XV lines. Strong collision and quadrupolar potential contributions. *Adv. Space Res.* **2014**, *54*, 1184-1189. https://doi.org/10.1016/j.asr.2013.08.017
[33] R. Aloui, H. Elabidi, S. Sahal-Bréchot and M. S. Dimitrijević. Quantum and semiclassical Stark widths for Ar VII spectral lines. *Atoms.* **2018**, *6*, 20-34. https://doi.org/10.3390/atoms6020020
[34] H. Elabidi and S. Sahal-Bréchot. Quantum mechanical Stark widths for Ar V and Ar VI lines: scaling with temperature. *MNRAS.* **2018**, *480*, 697-706. https://doi.org/10.1093/mnras/sty1858
[35] H. Elabidi and S. Sahal-Bréchot. Stark line widths for N-like ions Na V, Mg VI, Al VII and Si VIII. Z–scaling. *MNRAS*. **2019**, *484*, 1072-1078. https://doi.org/10.1093/mnras/stv1970
[36] R. Aloui, H. Elabidi, R. Hamdi and S. Sahal-Bréchot. Quantum Stark broadening data for Ar VIII and Ar IX lines. *MNRAS*. **2019**, *484*, 4801-4810. https://doi.org/10.1093/mnras/stz303
[37] M. S. Dimitrijević and S. Sahal-Bréchot. Stark Broadening Parameter Tables for Ar VIII. *Serb. Astron. J.* **1999**, *160*, 15-20.
[38] E. U. Condon and G. H. Shortley. The theory of atomic spectra. Cambridge University Press. London. **1959**
[39] H. A. Bethe and E. E. Salpeter. Quantum Mechanics of One–and Two–Electron Atoms. Springer, Berlin, Göttingen. **1957**. 10.1007/978-3-662-12869-5
[40] M. Jones. Relativistic corrections to atomic energy levels. *J. Phys. B: At. Mol. Phys.* **1970**, *3*, 1571-1592. https://doi.org/10.1088/0022-3700/3/12/003
[41] M. Jones. Mutual spin-orbit and spin-spin interactions in atomic structure calculations. *J. Phys. B: At. Mol. Phys*. **1971**, *4*, 1422-1439. https://doi.org/10.1088/0022-3700/4/11/006
[42] G. Racah. Theory of Complex Spectra. III. *Phys. Rev.* **1943**, *63*, 367-382. https://doi.org/10.1103/PhysRev.63.367
[43] M. Baranger. General Impact Theory of Pressure Broadening. *Phys. Rev.* **1958**, *112*, 855-865. https://doi.org/10.1103/PhysRev.112.855
[44] A. Kramida *et al.* (accessed July 25, 2018), NIST Atomic Spectra Database (ver. 5.5.6), **2018** , https://physics.nist.gov/ asd
[45] K. Koc. Relativistic MR RCI Calculation of Energy Levels and Transition Probabilities of Boron Isoelectronic Sequence. *Phys. Scr.* **2003**, *67*, 491-499. https://doi.org/10.1238/Physica.Regular.067a00491
[46] J. P. Buchet, M. C. Buchet-Poulizac, and M. Druetta. Mean-life measurements of Na V, Na VI and Na VII levels in the extreme ultraviolet region. *Phys. Scr.* **1978**, *18*, 496-498. https://doi.org/10.1088/0031-8949/18/6/029
[47] X. Tordoir *et al*. Atomic lifetimes and transition probabilities in boron-like (Na VII) and beryllium-like (Na VIII) sodium ions. *Eur. Phys. J. D.* **1999**, *6*, 1-7. https://doi.org/10.1007/PL00021604
[48] D. E. Kelleher and L. I. Podobedova. Atomic Transition Probabilities of Sodium and Magnesium. A Critical Compilation. *J. Phys. Chem. Ref. Data*. **2008**, *37*, 267-706. https://doi.org/10.1063/1.2735328
[49] A. Burgess and V. B. Sheorey. Electron impact excitation of the resonance lines of alkali-like positive ions. *J. Phys. B: At. Mol. Phys.* **1974**, *7*, 2403-2416. https://doi.org/10.1088/0022-3700/7/17/026
[50] M. C. Chidichimo and S. P. Haigh. Electron-impact excitation of quadrupole-allowed transitions in positive ions. *Phys. Rev. A.* **1989**, *39*, 4991-4997. 10.1103/physreva.39.4991
[51] M. C. Chidichimo. Electron-impact excitation of electric octupole transitions in positive ions: Asymptotic behavior of the sum over partial-collision strengths. *Phys. Rev. A.* **1992**, *45*, 1690-1700. https://doi.org/10.1103/PhysRevA.45.1690
[52] M. Jones. Application of the Breit-Pauli approximation to the study of relativistic effects in electron-atom scattering. *J. Phys. B: At. Mol. Phys.* **1974a**, *7*, L284-285. https://doi.org/10.1088/0022-3700/7/9/003
[53] D. W. Walker. Electron impact excitation of hydrogenic ions. *J. Phys. B: At. Mol. Phys.* **1974**, *7*, 97-116. https://doi.org/10.1088/0022-3700/8/5/010
[54] M. Jones, M. Collision strengths for the electron-impact excitation of certain highly-ionized helium-like ions. *MNRAS*, **1974b**, *169*, 211-228. https://doi.org/10.1093/mnras/169.2.211

Journal of Umm Al-Qura University for Applied Science 6 (2020) 35-38

Journal of Umm Al-Qura University for Applied Science

journal homepage: https://uqu.edu.sa/en/jas/87823

X-ray Bright Sources in the Field of Active Galactic Nuclei MKN 205

B. A. Korany[a,b].

[a] *Department of Physics, Faculty of Applied Science, Umm Al-Qura University, Saudi Arabia.*
[b] *Department of Astronomy, National Research Institute of Astronomy and Geophysics (NRIAG), Helwan, Cairo, Egypt.*

ARTICLE INFO

Article History:
Submission date: 9/11/2019
Accepted date: 22/6/2020

Keywords:
X-ray: sources - X-ray: spectra

ABSTRACT

Three bright X-ray non-target sources were detected in the field of the seyfert 1 galaxy MKN 205. These sources were classified as optically Early-type galaxy, BLAGN, and NELG (NED, SIMBAD, and AXIS). The spectrum analysis was made for these objects using thermal models and non-thermal models, modified by interstellar absorption. In some objects, we cannot distinguish between the thermal and non-thermal models of the hard components from the spectrum alone. The presence of intrinsic absorption was tested by photoelectric absorption at the redshift of the sources, and we assumed the flux distribution is affected by the intrinsic absorption in some sources. A black body component used to test the presence of soft excess in some spectra, which has been interpreted as primary emission from the accretion disc or as secondary radiation form the reprocessing of the hard X-ray in the surface layers of the disc.

1. Introduction

MKN 205 is a nearby (z = 0.071) low luminosity radio quiet quasar with an intriguing Fe Kα emission line complex. X-ray emission is an important tool for the investigation of the gravitational evolution of the cosmos. Most of the sources making up the cosmological X-ray background turn out to be different types of Active Galactic Nuclei, AGNs, where the X-ray emission is due to the accretion of matter onto a supermassive Black Hole, the remainder being due to radiation from the hot gas in the deep potential wells of galaxy clusters. Modeling of the X-ray spectrum of the background radiation in terms of these individual sources requires a mixture of objects, displaying different amounts of low energy absorption in their spectra. Highly absorbed objects will thus emit the bulk of their X-ray radiation at energies above 2 keV where the amount of available spectral data is limited. The high sensitivity at energies up to 10 keV, provided by XMM-Newton satellite, will offer the possibility to perform a comprehensive study of the soft and hard X-ray spectra of samples of serendipitous X-ray sources in deep extragalactic fields. This will allow the investigation of the spectral properties of objects, which due to their low flux or hard spectrum could not be observed by previous X-ray instruments. In this work, we study some non-target X-ray sources in MKN 205 which is a nearby

(z= 0.071) low luminosity radio quiet quasar with an intriguing Fe Kα emission line complex [1] field observed by XMM-Newton.

In the present paper, we report on the detection and spectral analysis of X-ray observation of the field of MKN205, taken by XMM-Newton observations. We organized the paper as follows: The X-Ray observations and data reduction are presented in section 2, section 3 is devoted to the spectral analysis, while the results are summarized and concluded in section 4.

2. Observations and Data Reduction

The identifications presented in this paper correspond to the X-ray sources found in XMM-Newton data of MKN 205. The observations with the EPIC MOS [2] and PN [3] detectors were split into 3 parts, each of which was exposed for 17 ksec duration, to test a variety of sub-window modes. Three observations each was made with the MOS 1 and 2 cameras, in Full Window, Partial Window 2 and Partial Window 3 modes. For the PN, two observations were made in Full Window mode and one in Large Window mode. The re-processed data were reduced with the SAS software, using EMCHAIN and EPCHAIN; further filtering was then performed using xmmselect. A light-curve for the observations (PN, MOS1, and MOS2) was created to check for flaring high background periods, which are best visible above 10 keV. Images were extracted in the energy bands 0.2-0.5, 0.5-2.0, 2.0-4.5, 4.5-7.5 and 7.5-12.0 keV with binsize 22 in cases of MOS1 and MOS2, and 82 in PN case. The edetect_chain task was used for the above five energy bands with likelihood threshold =8, and energy conversion factors in units 1011 count. cm^2 erg^{-1} . In order to utilize the $\chi 2$ technique, the X-ray spectra were rebinned to contain at least 20 counts in each spectral bin using grppha command and then simultaneously fitting the spectra from MOS1, MOS2 and PN detectors, with the response functions for each detector, using the XSPEC spectral fitting package. The value of the galactic absorption (NH) was found to be 3×1020 cm^{-2} obtained from FTOOLS NH task. For the search of discrete X-ray sources, the detection metatask edetect_chain is applied to the three EPIC cameras. The above five energy bands were used.

3. Spectral Analysis

To identify the X-ray sources detected in MKN 205 field, a search program was carried out to compare positions of objects in our field with X-ray source positions of objects in several catalogues and archives (eg. SIMBAD, NED, USNO, APM-North, etc.). To improve the reliability of the identifications, the optical magnitude (B and V) are used to calculate the ratio of X-ray flux (fx) to optical flux(fop), which is given by the following relation [4]:

$$log(\frac{f_x}{f_{op}}) = log\,(f_x) + 0.4\,m_{op} + 5.37, \quad (1)$$

where mop is the optical magnitude. The optical magnitudes are given from SIMBAD, USNO and APM-North catalogues.

A spectral analysis for three bright non-target sources in MKN 205 field are performed. These sources are classified as, early-type galaxies (at right ascension & declination 12.338&75.370 (named Obj_12.338_75.370)), broad-line active galactic nuclei (BLAGN) (at right ascension & declination 12.348&75.833 (named Obj_12.348_75.833)) and narrow emission line galaxies (NELG) (at right ascension & declination 12.368&75.438 (named Obj_12.368_75.438)).

In this spectral analysis, three sets of data points and model curves (one for PN and two for MOS) were used. For all in the following plots, the upper curves are for PN data and the lower curves are for the MOSs data.

For the object Obj_12.338_75.370 an X-ray spectrum with a single-temperature thermal plasma model [5] modified by interstellar

* **Corresponding Author**
Department of Physics, Faculty of Applied Science, Umm Al-Qura University, Saudi Arabia.
E-mail address: **badiekorany@yahoo.com**

absorption was fitted to all of the ranges from 0.2 keV to 10.0 keV. The parameters: the plasma temperature, the metal abundance and the normalization were free in the fitting, and the absorption column density is fixed at 3 ×1020 cm^{-2}.

This model failed to reproduce the observed spectrum; it fitted the data well up to 2 keV. The χ^2/odf is 345.5/211, KT is 0.72±0.015 keV and the abundance parameter is 0.16±0.02. By using this model, an excess emission found above the 2 keV (Fig1). A thermal bremsstrahlung model for the hard component to estimate the temperature variation above 2 keV was assumed. The bremsstrahlung model together with Raymond model were then fitted to the same band (0.2 keV - 10.0 keV). The assumption of thermal bremsstrahlung model to this spectrum provides an acceptable fit (Fig 2) the χ^2/odf is 217/209, the reduced chi-square is 1.042 and the null hypothesis probability is 0.323. The output thermal temperature from this fit is KT 0.41±0.01 keV, while the thermal temperature from the bremsstrahlung model is 5.39±1.6 keV. In this fit the abundance parameter is 0.21±0.03.

The broad band spectrum when fitted by Power-law with Raymond model, an acceptable fit was obtained, the χ^2/odf = 220/209 with reduced chi-square is 1.052 and the null hypothesis probability is 0.29, with photon index 1.82±0.19 keV. The thermal temperature from Raymond- Power-law model is 0.40±0.01 keV as from Raymond-Bremsstrahlung model (Fig. 3). Therefore, we cannot distinguish between the two possible thermal and non-thermal models of the hard component from the spectrum alone.

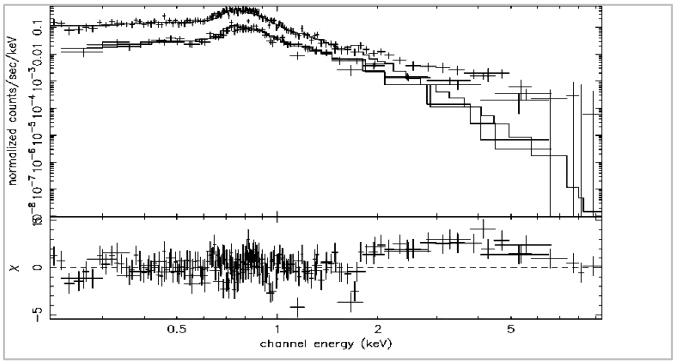

Figure 1: The PN, MOS1 and MOS2 spectra fitted using Raymond thermal model, with χ^2 test.

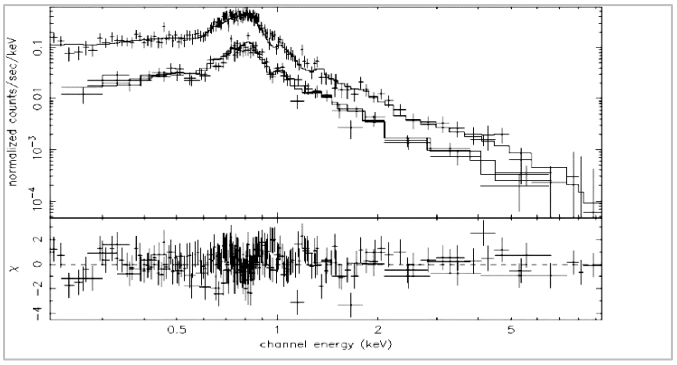

Figure 2: The PN, MOS1 and MOS2 spectra fitted using Raymond thermal model with thermal Bremsstrahlung, with χ^2 test.

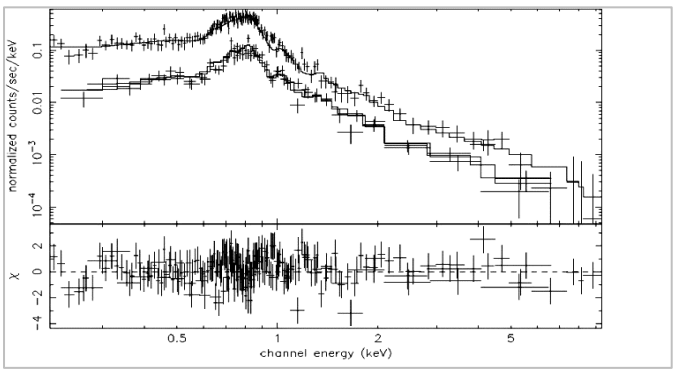

Figure 3: The PN, MOS1 and MOS2 spectra fitted using Raymond thermal model and Power-law model, with χ^2 test.

The two other objects Obj_12.348_75.833 and Obj_12.368_75.438 are classified as BLAGN and NELG respectively. The spectral analysis of these objects started with fitting a single power-law to the background-subtracted spectra. This model has two free parameters, the normalization, and the continuum slope Γ. A fixed photoelectric absorption component was included to account for the effect of the galactic absorption along the line of sight. Fitting this model gives a good reduced χ^2 for the two objects (Figs. 4 and 5) with photon index 1.7±0.04 keV and 1.5±0.03 keV respectively. The fitted parameters are summarized in Table (1).

Table 1: The fit parameters of the power-law model for the two objects

Parameter	Obj_12.348_75.833	Obj_12.368_75.438
Absorption column density (NH)	3×10^{20} cm^{-2} (fixed)	3×10^{20} cm^{-2} (fixed)
Γ	1.7±0.04 keV	1.5±0.03 keV
χ^2	87	153
odf	99	138
Norm	1×10^{-4}	8.3×10^{-5}

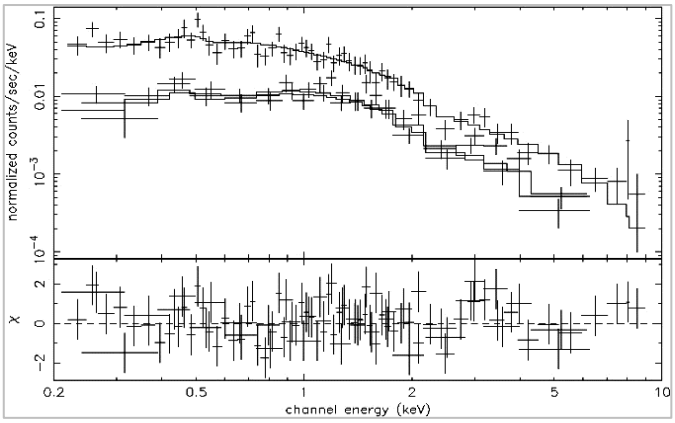

Figure 4: The PN, MOS1 and MOS2 spectra fitted using Power-law model with fixed photoelectric absorption component for Obj_12.348_75.833

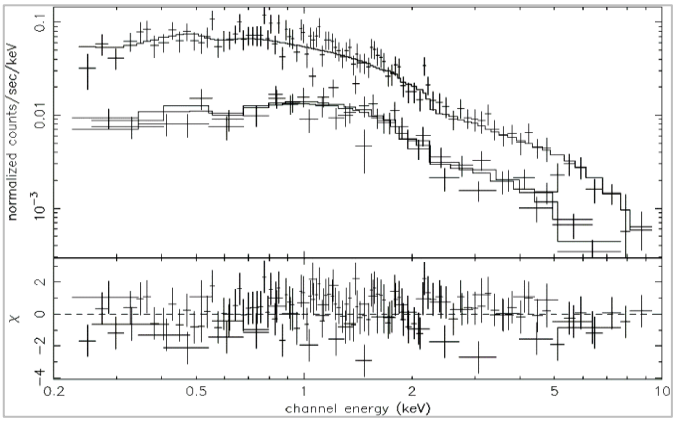

Figure 5: The PN, MOS1 and MOS2 spectra fitted using Power-law model with fixed photoelectric absorption component for Obj_12.368_75.438

In order to test whether intrinsic absorption is present, photoelectric absorption at the redshift of the source (0.65 and 0.24) is fitted, where the redshift was taken from Barcons, et al. (2002) [6]. In this case three parameters are free, the normalization, the photon index Γ, and the rest frame absorption. There is no significant improvement by adding this component, in the reduced χ^2 (0.89 and 1.07 respectively). The intrinsic absorption components (NH) from this fit are 1.13×10^{11} ±0.05 and 3.53×10^{11} ±0.015, this does not make sense. It is not possible to measure NH values much lower than 10^{20} cm^{-2} with XMM. This means that we need data with much better statistics to simultaneously fit the different contributions of intrinsic absorption for this object. The F-test (F = 5.8, F-probability = 1.73×10^{-2}) tells us that going from power-law model with fixed NH to a power-law model with intrinsic NH as additional fit parameter represents a significant improvement of the fit (Figs. 6-7). The agreement for this object is excellent so, one can assume that the flux distribution is affected by intrinsic absorption.

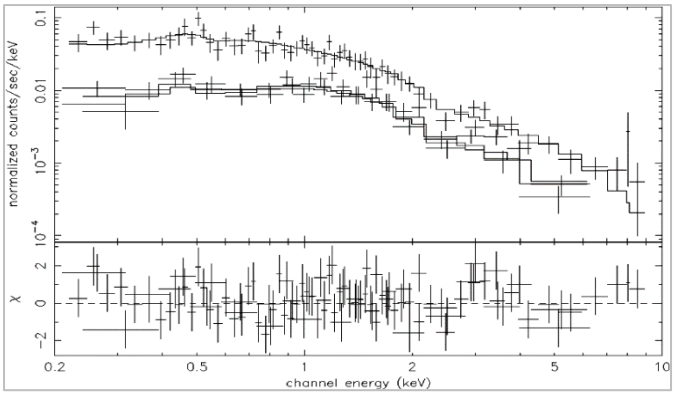

Figure 6: The PN, MOS1 and MOS2 spectra fitted using Power-law model with photoelectric absorption at the redshift for Obj_12.348_75.833

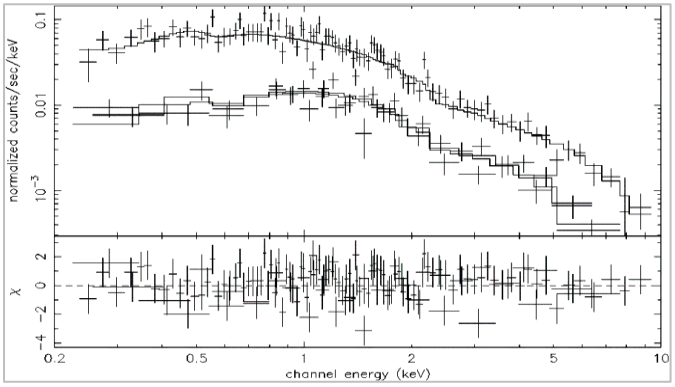

Figure 7: The PN, MOS1 and MOS2 spectra fitted using Power-law model with photoelectric absorption at the redshift for Obj_12.368_75.438

The determination of soft excess may depend on the knowledge of the shape of the power-law and the quantity of absorption. It has been interpreted as a primary emission from the accretion disc, the gravitation energy released by: the emission from the accretion disc, by the viscosity in the disc or as secondary radiation from the reprocessing of hard X-rays in the surface layers of the disc. We can provide a good fit to this soft excess by several models, such as: single black body, multiple black bodies, multicolor dick black body, blurred reaction from partially ionized material, smeared absorption, and thermal computerization in the optically thick medium [7]. To do this, the spectra were fitted with power-law and a low energy black body component (at the redshift of the source) taking into account absorption in our Galaxy. The χ^2/odf are 85.05/97 and 149/136, respectively for these fits. The photon indexes are changed to 1.42±0.04 keV and 1.42±0.05 keV and the thermal temperatures from the black body component (KT) are 0.39±0.17 and 0.38±0.17 keV (Table 2 summaries the fit parameters) as shown in Figures (8 and 9).

The F-test (F 1.01, 1.90 and F-probability 0.368, 0.153) tells us that going from power-law model to a power-law model with black body component, as an additional fit parameter does not represent a significant improvement of the fit. This means that we need more data with much better statistics to simultaneously fit the different contributions of the soft excess component.

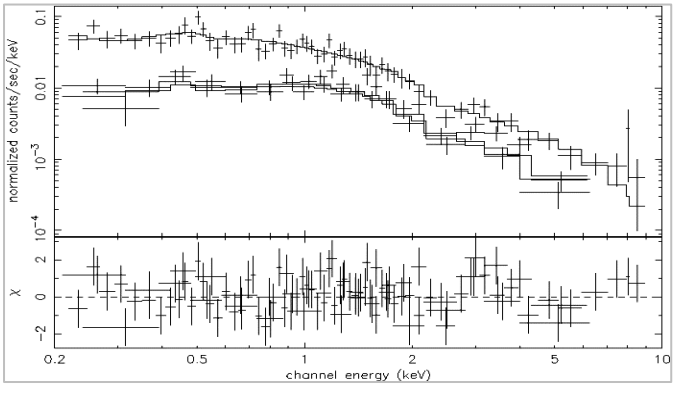

Figure 8: The PN, MOS1 and MOS2 spectra fitted using Power-law model with a black-body component for Obj_12.348_75.833.

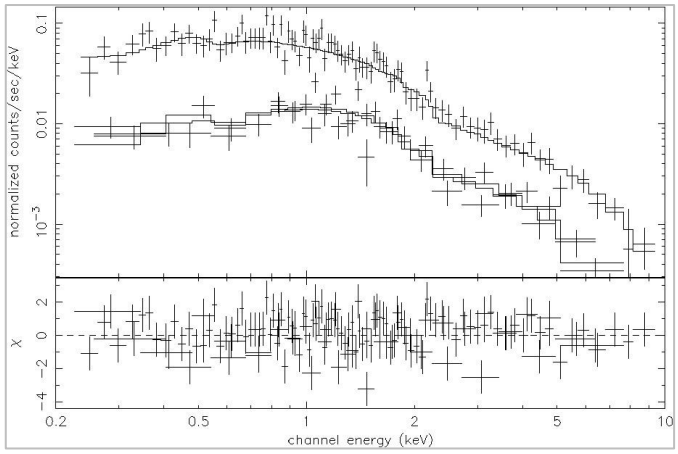

Figure 9: The PN, MOS1 and MOS2 spectra fitted using Power-law model with a black-body component for Obj_12.368_75.438

Table 2: The fit parameters of the power-law model with a black-body component for the two objects

Parameter	Obj_12.348_75.833	Obj_12.368_75.438
Absorption column density (N_H)	3×10^{20} cm^{-2} (fixed)	3×10^{20} cm^{-2} (fixed)
Γ	1.6±0.06	1.4±0.05
KT	0.39±0.17 keV	0.38±0.17 keV
χ^2	85	149
Odf	97	136
Norm	1.45×10^{-7}	4.68×10^{-7}

4. Discussion and Conclusion

The aim of the paper was to detect, classify and spectral analyze the possible bright X-ray non-target sources in MKN 205 field. We detected three bright objects in this field, these sources are located at right ascension & declination 12.338&75.370, 12.348&75.833 and 12.368&75.438 and classified optically as Early-type galaxy, BLAGN, and NELG, respectively.

The flaring high background periods checked by creating alight curves. For the first object an X-ray spectrum with a single-temperature thermal plasma model modified by interstellar absorption was fitted from 0.2 keV to 10.0 keV with a fixed the absorption column density at 3 × 1020 cm-2. The thermal temperature (KT) of this fit is 0.72±0.015 keV and the abundance parameter is 0.16±0.02. A thermal bremsstrahlung model for the hard component to estimate the temperature variation above 2 keV was assumed. The bremsstrahlung model, together with Raymond model, were then fitted to the same band. The assumption of thermal bremsstrahlung model to this spectrum provided an acceptable fit and the output thermal temperature from this fit is 0.41±0.01 keV, while the thermal temperature from the bremsstrahlung is 5.39±1.6 keV. In this fit the abundance parameter is 0.21±0.03. When the spectrum fitted by Power-law with Raymond model, an acceptable fit was obtained with a photon index 1.82±0.19, and the thermal temperature from Raymond- Power-law model is 0.40±0.01 keV as from Raymond-Bremsstrahlung model.

The two other objects fitted firstly by a single power-law to the background-subtracted spectra and a fixed photoelectric absorption component was included to account for the effect of the galactic absorption along the line of sight. A photoelectric absorption at the redshift of the source was fitted in order to test whether intrinsic absorption is present. There is no significant improvement by adding this component. The intrinsic absorption components (NH) from this fit were 1.13×10^{11} ±0.05 cm^{-2} and 3.53×10^{11} ±0.015 cm^{-2}. It is not possible to measure NH values much lower than 10^{20} cm^{-2} with XMM. The F-test tells us that going from power-law model with fixed NH to a power-law model with intrinsic NH as an additional fit parameter represents a significant improvement of the fit. The agreement for this object is excellent so, one can assume that the flux distribution is affected by intrinsic absorption. Finally, we tested the X-Ray soft excess by adding a black body component to the power law model, and the thermal temperatures from the black body component (KT) are 0.39±0.17 and 0.38±0.17 keV. But, the F-test tells us that going from power-law model to a power-law model with black body component

as an additional fit parameter does not represent a significant improvement of the fit.

References

[1] S. Laha, R, Ghosh, S. Tripathi, M. Guainazzi. Investigating the origin of the Fe emission lines of the Seyfert 1 galaxy Mrk 205. MNRAS, 2019, 486, 3124–3133. https://arxiv.org/abs/1904.06476

[2] M. J. L. Turner, A. Abbey, M. Arnaud, et al. The European Photon Imaging Camera on XMM-Newton: The MOS cameras. A&A, 2001, 365, L27-L35.

[3] L. Strüder, U. Briel, K. Dennerl, K.; .et al , The European Photon Imaging Camera on XMM-Newton: The pn-CCD camera, A&A, 2001, 365, L18-L26.

[4] T. Maccacaro, I. M. Gioia, A. Wolter, G. Zamorani, J. T. Stocke, The X-Ray Spectra of the Extragalactic Sources in the Einstein Extended Medium-Sensitivity Survey. AphJ, 1988, 326, 680-690. DOI: 10.1086/166127

[5] J. C. Raymond, B. W. Smith, Soft X-ray spectrum of a hot plasma. Astrophysical Journal, 1977, 35, 419-439. DOI: 10.1086/190486

[6] X. Barcons, F. J. Carrera, M. G. Watson, et al,. The XMM-Newton serendipitous survey . II. First results from the AXIS high galactic latitude medium sensitivity survey, A&A, 2002, 382, 522-536. DOI: 10.1051/0004-6361:20011615

[7] B. Korany, M. Nouh, X-Ray Warm Absorber Variability of the Seyfert Galaxy Arakelian 564. Astrophysics, 2019, 62, 300-312. https://arxiv.org/ftp/arxiv/papers/1810/1810.00175.pdf

Journal of Umm Al-Qura University for Applied Science 6 (2020) 39-43

Journal of Umm Al-Qura University
for Applied Science

journal homepage: https://uqu.edu.sa/en/jas/87823

The Impact of PG Classes and Addition of FGDB on Air Pollution Emitted from Shuaibah III (IWPP) Plant: Screening Model

Abdel-Baset H. Mekky [a].

[a] *Physics Department, Faculty of Science and Arts Al-Methnab, Qassim University, Al-Methnab, Kingdom of Saudi Arabia.*

ARTICLE INFO

Article History:
Submission date: 16/9/2019
Accepted date: 24/12/2019

Keywords:
Screening model, Pollutant gases, Shuaibah III (IWPP) Plant, Flue gas desulfurization by-products (FGDBs), Pasquill-Gifford classes.

ABSTRACT

The objective of the present work is the studying of air quality that contained pollutant gases (SO_2, NO_x, CO), and PM released from the Shuaibah III (IWPP) plant as a case study. Also, we tried to evaluate the effect of Flue gas desulfurization byproduct (FGDB) on SO_2 that turned into carried out within the studied place. For the determination of dispersion, the source of pollution was taken into consideration to be in a rural area. The screening model was used to calculate concentrations dispersion of gas pollutants at different Pasquill-Gifford stability classes' conditions. The levels C_{max} (maximum concentrations) decreased from A-class to F-class, and the influence distance D_{max} (maximum distance of downwind concentrations) quickly grows. The SO_2 dispersion became affected by the FGDB system. The results confirmed that the C_{max} of air pollutants released from the stack may additionally decreases than the Saudi Arabian standard.

1. Introduction

The power generating plants are the main source of gas pollutants in the rural and urban in addition to industrial activations. It's usually agreed that SO_2 decreases the visibility in any region, harm several materials, crops and health of human [1]. Once SO_2 is changed and hydrolyzed, it offers rise to air pollution. The quantitative estimation of the long-time period common of SO_2, NO_2, CO, and PM has been handled by means of several researchers [2–5]. Chih-Chung and Hui-Hsuan [6] investigated, however, region air pollutants (PM, SO_2, NO, CO) and environmental conditions (wind speed) have an effect on region turbidity. The relation between the concentration of SO_2 within the air and also the degree of injury to nearby became studied with the aid of Navara and Kaleta [7]. In closed environments, the concentration of CO will simply rise to total levels. On average, 170 people within the United State die each year from CO made by non-automotive users produces [8]. The energy created by power stations comes from the combustion of oil and natural gas fuel. The combustion method of fuel is accompanied *via* emission to the surroundings of huge quantities of exhaust waste gases, with an increasing rate annually corresponding to that of conventional electric power produced.

To satisfy clean air requirements, moist scrubber generation presently used eliminates lots of SO_2 to produce large quantities of (FGDBs), flue gas desulfurization by-products [9,10]. However, FGDB is additionally called a potential environmental waste material at each regional and international levels [11]. Thus, FGDB represents a good useful use to low disposal of the waste material. A number of investigators work on the influence of FGDB as changing in some applications lead to many organizations and institutes at dispersed spaces over all the world [12–15].

Computational science has come to be a significant tool in forecasting and examining many systems of emissions. With increasing interest in numerical methodologies, software tools are established for demonstrating the plant releases and its effect on air dispersion [16–18]. This consists of the progress and support of different computational software, additionally as optimization of plant abilities to improve the air feature. Those simulations are not essential to forecast the emission of pollutant concentrations only but also to identify the relations between changed measures in the air [19,20].

The target of this research aimed to use a screen view to estimate ground-level concentration of emission gases pollutant from the Shuaibah III (IWPP) plant in Jeddah, Saudi Arabia. The special effects of variations for Pasquill-Gifford stability classes in the model, and the Flue gas desulfurization by-products (FGDBs) those are predicted to affect the pollutant dispersion in air were investigated.

2. Study Area

The Shuaibah III (IWPP) plant is a power and desalination station on the coast of the Red Sea, south of Jeddah in the Kingdom of Saudi Arabia. Figure 1 shows the location of the study area.

Figure 1. Location of Shuaibah Phase III Power and Desalination Plant in Saudi Arabia.

3. Meteorological Description of The Study Area

The dispersion of pollution inside the atmosphere is substantially dependent on the atmospheric conditions. So, an evaluation of some meteorological parameters became completed. The period of time from 1980 to 2016 that considered for determined temperature, the amount of cloud cover, ambient and wind speed, and direction, as shown in Figure 2 (a to d), respectively. These parameters are for King Abdul-Aziz airport meteorological station in Jeddah city.

3.1. Temperature

The average of excessive temperature is above 37°C for the hot season. The hottest day is with an average (39 - 27°C). Furthermore, the common every day excessive temperature below 30°C for the cool

* **Corresponding Author**
Physics Department, Faculty of Science and Arts Al-Methnab, Qassim University, Al-Methnab, Kingdom of Saudi Arabia.
E-mail address: **univ.physics@yahoo.com**

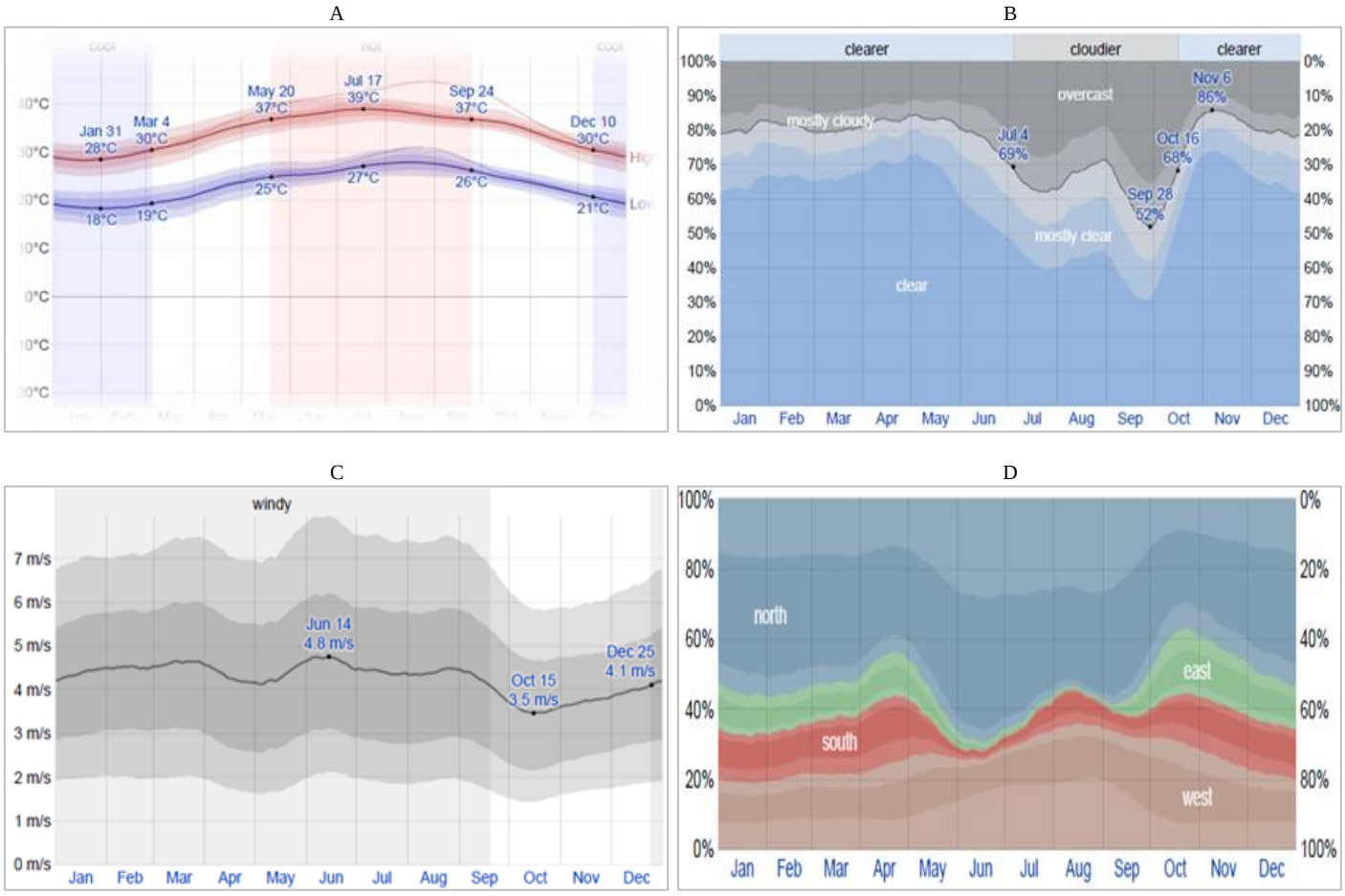

Figure 2. (a) Average High and Low Temperature, (b) Cloud Cover Categories, (c) Average Wind Speed and (d) Wind Directions

time of year. The coldest day is with an average low of 18°C and excessive of 28°C. At Figure 2(a), the red and blue lines represent the daily average high and low temperatures, respectively.

3.2. Clouds

The percentage of the most part cloudy skies is 48% of the year, and the percentage of the most part clear skies is 52% of the year. Here cloud cover mark is 10 which designed for completely clear, dropping to 9 which designed for the most part clear, and to 1 which designed for completely cloudy.

3.3. Wind speed and directions

Almost, the average wind speed is calm over the year. The windier days has more than 4.1 m/s wind speed. The calmest day has 3.5 m/s wind speed. The prevailing wind direction is north during the year.

4. Methods and calculations

The objective of this case examine is to estimate gaseous pollutants concentration emitted constantly by a point source (chimney stack). The predicted values are obtained considering ground level, under plume center-line, in the function of distance from the source and the source of pollution is considered to be in a rural area. In addition, the effluent plume consists of a mixture of the following pollutants: SO_2, NO_x, CO and PM (particulate matter) in suspension. These pollutants are known to be emitted by electric power plants functioning with solid fuel [21–25].

In this study, SCREEN3 software was used to simulate the dispersion from the stack of a plant, after 1 hour of emission. The SCREEN3 is a software (Likes Environmental Software, Waterloo, Ontario, Canada) [23], established by the EPA established on the Gaussian plume dispersion model [23]. It is a version of the ISC3 model [25,26]. To evaluate the concentrations air pollutants, the using model includes several input parameters associated with the source of emitting and meteorological characteristics. The requested input parameters to run the software contain:

- emission source type
- pollutants emission rate
- stack height
- stack inside diameter
- stack exit velocity
- temperature of exit gas
- ambient air temperature
- receptor height
- wind speed and direction

The Pasquill-Gifford stability classification categorizes six classes of atmospheric stability: A (very unstable), D (neutral), B (unstable), E (slightly stable), C(slightly unstable) and F (stable). Table 1 illustrated Pasquill-Gifford stability classification [27,28].

Table 1. Pasquill-Gifford Stability Classes

Wind Speed (at 10m) (m/s)	Day Time Solar Insolation (W/m^2)			Radiation Overcast
	Strong >600	Moderate 300-600	Slight <300	
<2	A	A-B	B	C
2-3	A-B	B	C	C
3-5	B	B-C	C	C
5-6	C	C-D	D	D
>6	CA-B	D	D	D

To express real conditions of atmospheric dispersion phenomenon, as emission conditions, considered input data for simulations were taken the following experimentally measured parameters at the proposed Shuaibah III, Independent Water, and Power Plant (IWPP) and presented in reference [29] that is provided below in Table 2.

Moreover, the effect of flue gas desulfurization by product (FGDB) on SO_2 was conducted in studied area has evaluated.

Table 2. General description and specifications for Shuaibah III **(**IWPP) Stack emissions.

Parameter	Standard IWPP 0% FGDB (Flue gas desulfurization byproduct); 2.0% S-fuel Content; 35° C Sea-water Temperature	Mitigated IWPP 95% FGDB (Flue gas desulfurization byproduct); 2.0% S-fuel Content; 35oC Sea-water Temperature	Units
Stack Coordinate	20° 41' N, 39° 31' East	20° 41' N, 39° 31' East	Degree / direction
Stack Height	150	150	m
Equivalent Stack Diameter[2]	7.0	5.7	m
Thermal Input	4,182	4,182	MWt
Flue Gas Flow Rate, STD, Wet, Actual O2[1]	1,995,000	1,927,500	Nm^3/h
Flue Gas Flow Rate, STD, Dry, 3% O_2	1,631,510	1,631,510	Nm^3/h
Exhaust Gas Velocity2	25	25	m/s
Flue Gas Temperature	190	46.6	°C
Sulfur Content in Fuel[1]	2.0	2.0	%
SO2 Emissions	5,710	375	Kg/h
NOx (as NO_2) Emissions	653	653	Kg/h
Particulate Matter Emissions	82	82	Kg/h
CO Emissions	2.72E-7	2.72E-7	Kg/h

1 Estimate/Assumed by Siemens.
2 Estimate/Assumed by WSP Environmental Ltd.
STP: Standard Temperature and Pressure (273 K, 1013 hPa).

5. Results and discussion

As the emission conditions listed above (Table 2)**,** were considered the same for all pollutants, except the emission rates. For analyzed pollutants, maximum 1-hour concentration values are given in Figures (3-7) for SO_2, NO_x, CO, PM, and that related to the effect of FGDB on SO_2 pollutant, respectively, for the six stability classes. Further, pollutant concentrations decrease with distance from the source.

As the release occurs from the stack, the plume first increases with distance reach a maximum value and then decreases as shown in Figures from 3 to 7.

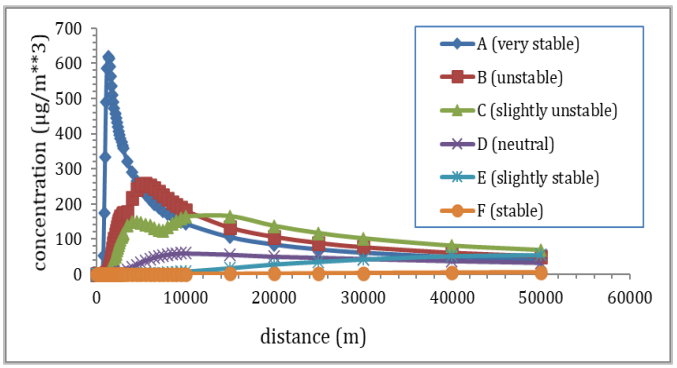

Figure 3. SO_2 concentration as a function of distance from the stack.

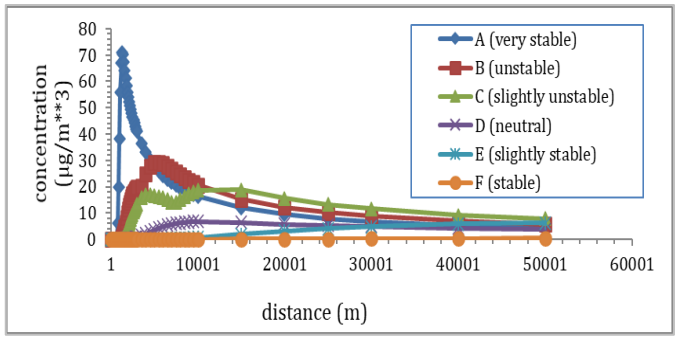

Figure 4. NO_x concentration as a function distance from the stack.

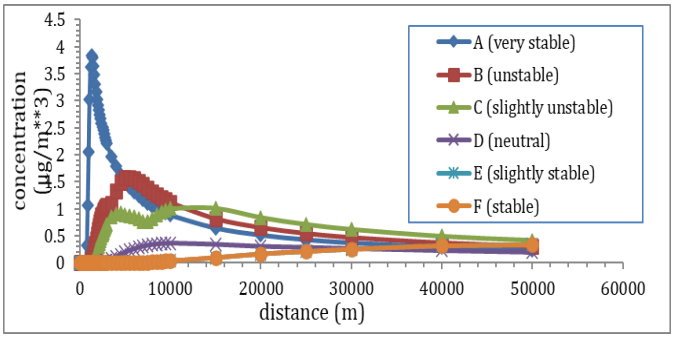

Figure 5. CO concentration as a function distance from the stack.

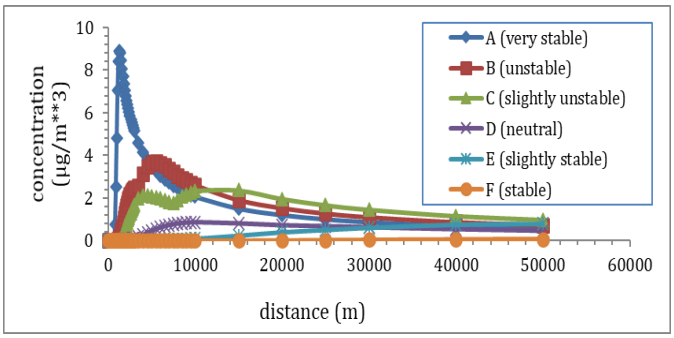

Figure 6. PM concentration as a function distance from the stack.

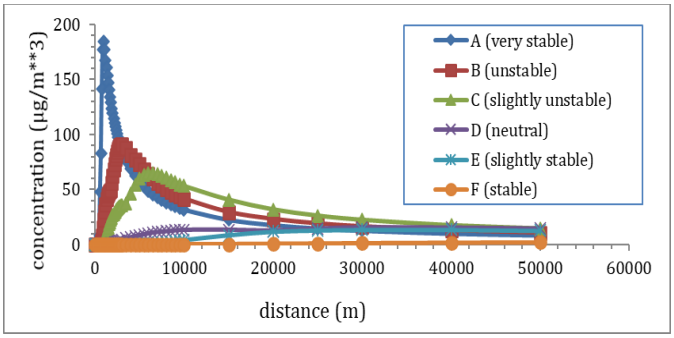

Figure 7. FGDB on SO2 concentration as a function distance from the stack.

Great concentrations of pollutants occur under unstable category at ground level adjacent to stack. These due to the high grade of convective turbulence (strong instabilities) which associated with clear sky conditions that go together with strong heating and small winds. Pollutants disperse fairly extended distances before dropping on the ground in weighty amounts, occurs in the neutral category. These due to the small scale and stable turbulence associated with moderated overcast and strong winds. At the very stable category, which associated with a little turbulence at a considerable ground distance above the stack, will be occurred.

Maximum predicted concentration established at ground level of SO_2, NO_x, CO, PM, and these aimed at the influence of FGDB on SO_2 emission, dispersion simulated by the user model for the six stability classes are offered in Figures 8 (a and b) and 9 (a and b).

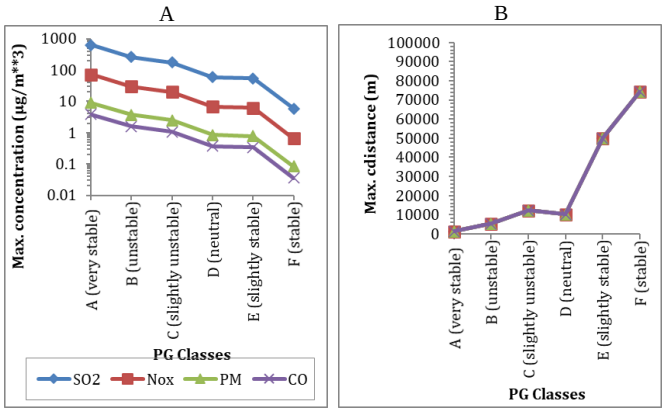

Figure 8. (a) The relation between C_{max} And PG Classes for all studied pollutants, (b) The relation between D_{max}. distance (m) and PG Classes for all studied pollutants.

The very stable conditions F class causes great dispersion area of the toxic cloud, the contrasting very unstable A class conditions interprets during a very small affected region around the source. D_{max} will increase as increasing of categories from A to F.

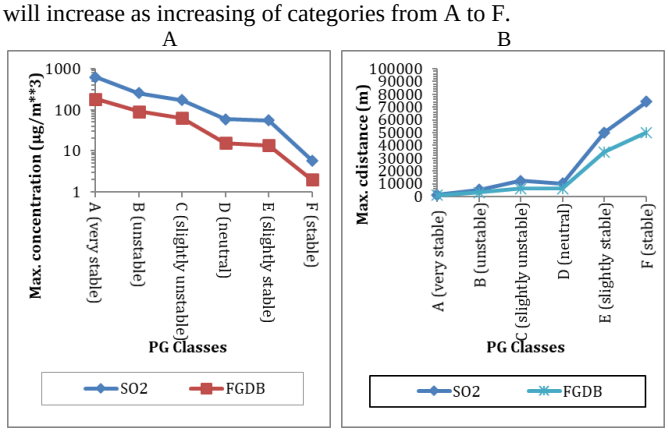

Figure 9. (a) C_{max}. concentration (µg/m^3) and PG Classes for case SO_2 and FGDB system, (b) The relation between max. distance (m) and PG Classes for case SO_2 and FGDB system.

Under the presented conditions, over the whole thought of vary (as much as 5 km faraway from source), the concentration values do not go above the 1-hour limit value needed by the AQI (air quality index) in Kingdom Saudi Arabia. For comparison, in Table 3 are given the pollutants maximum allowable concentrations standards required by AQI in Saudi Arabia.

Table 3. Pollutants maximum admissible concentrations (*AQI Saudi Arabia)*

Pollutant	Average admissible concentrations [µg/m3]			
	8 hours	1 hour	24 hours	Annual
SO2	-	730	365	80
NOx	-	660	-	100
CO	10	40	-	-
PM 10	-	-	340	80
PM 2.5	-	-	35	15

6. Conclusions

This study shows the results of modeling air dispersion of four types of gaseous pollutants (SO_2, NO_x, CO, and PM) which may be emitted by Shuaibah III, Independent Water and Power Plant (IWPP) plant which functions on P-G stability, and addition of FGDB system. By the used software, the ground level concentration of pollutants and the FGDB system was estimated. The turbulence falls from category A to F thus rapid dispersion of pollutants at F stability category, so that C_{max} decrease with the same path and D_{max} rapidly raises. The addition of the FGDB system decreased the dispersion of SO_2. Also, it was determined the concentration of the maximum pollutant and compared with the admissible values required by the AQI in Saudi Arabia and found that the concentration values do not exceed the 1-hour limit value required by the Saudi AQI.

References

[1] M.S. Naik, Dispersion of sulphur dioxide around the thermal power plant at Ahmedabad, India, *Atmos Environ Part B Urban Atmos.*, **1992**, *26*, 331–338. doi:10.1016/0957-1272(92)90008-G.

[2] S.B. Patil, S. B. Patil Estimation of A Quantitative Air Quality Impact Assessment Score For A Thermal Power Plant, *Atmospheric Environment* , **1990** 24B, 443~-48.

[3] P. Goyal, M.P. Singh, The long-term concentration of sulphur dioxide at Taj Mahal due to the Mathura Refinery, *Atmos Environ Part B*, Urban Atmos., **1990,** *24*, 3, 407–411. doi:10.1016/0957-1272(90)90048-Y.

[4] N. Raghavan, P. Goyal, S. Basu, A Gaussian model for predicting SO_2 concentration in the City of Agra, *Atmos Environ.*, **1983,** *17*, 2199–2203. doi:10.1016/0004-6981(83)90216-0.

[5] A. Kansal, M. Khare, C.S. Sharma, Air quality modelling study to analyse the impact of the World Bank emission guidelines for thermal power plants in Delhi, *Atmos Pollut Res.*, **2011**, *2*, 99–105. doi:10.5094/APR.2011.012.

[6] C.C. Wen, H.H. Yeh, Comparative influences of airborne pollutants and meteorological parameters on atmospheric visibility and turbidity, *Atmos Res.*, **2010**, *96*, 496–509. doi:10.1016/j.atmosres.2009.12.005.

[7] J. Navara, I. Horváth, M. Kaleta, Contribution to the determination of limiting val*ues of sulphur dioxide for vegetation in the region of Bratislava, Environ Pollut.*, **1978**, *16*, 263–275. doi:10.1016/0013-9327(78)90077-0.

[8] A. A. Sabri, Mathematical Model For The Study Effects Of Meteorological Conditions On Dispersion Of Pollutants In Air, **2011,** *04*, 150–165.

[9] H.L. Yu, W. Gu, J. Tao, J.Y. Huang, H.S. Lin, Impact of addition of FGDB as a soil amendment on physical and chemical properties of an alkali soil and crop yield of maize in Northern China Coastal Plain, *J Chem.*, **2015**, *2015*, 1-11. doi:10.1155/2015/540604.

[10] S.O.R. Program, S O 2 Scrubbing Technologies : *A Review*, **2001**, *20*, 219–228.

[11] M. Ahmaruzzaman, A review on the utilization of fly ash, *Prog Energy Combust Sci.*, **2010,** *36*, 327–363. doi:10.1016/j.pecs.2009.11.003.

[12] F.E. Rhoton, D.S. McChesney, Influence of FGD gypsum on the properties of a highly erodible soil under conservation tillage, *Commun Soil Sci Plant Anal.*, **2011,** *42*, 2012–2023. doi:10.1080/00103624.2011.591473.

[13] T.M. DeSutter, L.J. Cihacek, S. Rahman, Application of Flue Gas Desulfurization Gypsum and Its Impact on Wheat Grain and Soil Chemistry, *J Environ Qual.*, **2014,** *43*, 303-311. doi:10.2134/jeq2012.0084.

[14] M.E. Buckley, R.P. Wolkowski, In-Season Effect of Flue Gas Desulfurization Gypsum on Soil Physical Properties, *J Environ Qual.*, **2014,** *43*, 322-327. doi:10.2134/jeq2012.0354.

[15] [15] L. Chen, R. Stehouwer, M. Wu, D. Kost, X. Guo, J.M. Bigham, J. Beeghly, W.A. Dick, Minesoil Response to Reclamation by Using a Flue Gas Desulfurization Product, *Soil Sci Soc Am J.*, **2013**, *77*, 1744-1754. doi:10.2136/sssaj2013.02.0054.

[16] E. Miyata, S. Mori, Optimization of Gas Detector Locations by Application of Atmospheric Dispersion Modeling Tools, Sumitomo Kagaku. I **2011** 1–10.

[17] M. Bradley, J. Nasstrom, B. Kosovic, Models and Measurements: Complementary Tools for Predicting Atmospheric Dispersion and Assessing the Consequences of Nuclear and Radiological Emergencies, Int Conf Monit Assessments, *Uncertainties Nucl Radiol Emerg Response*. **2005**. https://e-reports-ext.llnl.gov/pdf/327514.pdf.

[18] W. E. Heilman, Z. Shiyuan, J. L. Hom, J. J. Charney, Development of Modeling Tools for Predicting Smoke Dispersion from Low-Intensity Fires (JFSP Research Project Reports. Paper 51.), **2013**, 65.

[19] J.M. Stockie, The Mathematics of Atmospheric Dispersion Modeling, *SIAM Rev.*, **2011**, *53*, 349–372. doi:10.1137/10080991X.

[20] J. Behrens, Adaptive Atmospheric Modeling, *www-M3.Ma.Tum.De*. **2006**. doi:10.1007/3-540-33383-5.

[21] A. Diffusion, N. Stokes, T. Diffusion, T.D. Coefficient, D.C. Dt, *Atmospheric dispersion modeling*, **197**1, 1–7 .
[22] L. Vîlceanu, Prediction Of Gaseous Pollutants, **2017,** 187–190.
[23] US EPA, SCREEN3 Model User's Guide, US Environ Prot AGENCY Off Air Qual Plan Stand Emiss. EPA-454/B- **1995**. doi:10.1016/j.ophtha.2012.04.029.
[24] M.D. Diener, J.M. Alford, Isolation and properties of small-bandgap fullerenes, *Nature.*, **1998**, *393*, 668–671. doi:10.1038/31435.
[25] User ' S Guide for the Industrial Source Complex (Isc3) Dispersion Models Volume I - User Instructions**, I 1995**.
[26] S. Zhong, L. Zhou, Z. Wang, Software for environmental impact assessment of air pollution dispersion based on ArcGIS, *Procedia Environ Sci.*, **2011**, *10*, 2792–2797. doi:10.1016/j.proenv.2011.09.433.
[27] G. Asadollahfardi, M. Asadi, M. Youssefi, S. Elyasi, M. Mirmohammadi, Experimental and mathematical study on ammonia emission from Kahrizak landfill and composting plants, Tehran, Iran, *J Mater Cycles Waste Manag.*, **2015,** *17*, 350–358. doi:10.1007/s10163-014-0242-1.
[28] S.D. Chambers, D. Galeriu, A.G. Williams, A. Melintescu, A.D. Griffiths, J. Crawford, L. Dyer, M. Duma, B. Zorila, Atmospheric stability effects on potential radiological releases at a nuclear research facility in Romania: Characterising the atmospheric mixing state, *J Environ Radioact*., **2016,** *154*, 68–82. doi:10.1016/j.jenvrad.2016.01.010.
[29] P. Wilson, Shuaibah Phase III IWPP Environmental and Social Impact Assessment, 1 **2005**.

Journal of Umm Al-Qura University for Applied Science

journal homepage: https://uqu.edu.sa/en/jas/87823

Probing the X-ray Spectra of Alpha Coronae Borealis

B. A. Korany [a,b].

[a] *Department of Physics, Faculty of Applied Science, Umm Al-Qura University, Saudi Arabia.*
[b] *Department of Astronomy, National Research Institute of Astronomy and Geophysics (NRIAG), Helwan, Cairo, Egypt*

ARTICLE INFO

Article History:
Submission date: 22/10/2019
Accepted date: 6/12/2019

Keywords:
Eclipsing Systems, X-ray, Alpha Coronae Borealis, α CrB

ABSTRACT

In this context, I presented a detailed spectral and timing analysis of X-ray observations of the brightest eclipsing system Alpha Coronae Borealis taken by XMM-Newton. We got from the thermal plasma metal model the abundances of some elements (O, Mg, Si, and Fe) and an emission line at 1.3 Kev from the simple Gaussian line profile. From the light curves, there is a strong, active region at the lower left of the maps, near the limb of the G component, and increasing in some parts, which means a band diagonally, runs across the G star disk from lower left to upper right, close to the projected center.

1. Introduction

Alpha Coronae Borealis (α CrB) is one of the brightest eclipsing systems; so many studies were interested in this system in different energy bands. Stebbins [1] discussed it early in an optical band [2]. Tomkin [3] gives detailed optical information for this system as; it is a 17.4 day eclipsing binary, the spectral types of its components are A and G with different masses, the G- type component is a dwarf star in a 17.4 day orbital period, and the system orbital property is i=88.2, rp =0.07±0.007, rs = 0.021±0.001. Schmitt, in 2016, used the TIGRE 1.2 m telescope observation to get a new radial velocity curve, apsidal motion, and the alignment of the rotation and orbit axes. The apsidal motion rate $0.035 < \omega < 0.054$ degrees/year and the apsidal motion period (Paps) is in the range of 6600 yr < Paps < 10 600 yr, while the apsidal motion values results in a difference of 7.2 s < ΔPsp = Ps − Pp < 11.6 s [4].

The First X-ray observation of this system was by ROSAT in 1993 [2]. Schmitt and Kurster [2,5] reconstructed a rough surface X-ray map, applying a maximum likelihood method. The resulting map revealed a patchy surface coverage of X-ray emitting material. The X-ray light curve of α CrB shows a total X-ray eclipse during the secondary optical minimum with the G star behind the A star. The totality of the eclipse demonstrates that the A-type component in α CrB is X-ray dark and that the x-ray flux arises exclusively from the later-type companion [2]. Güdel et al. [6] used X-ray data, observed by XMM-Newton, during a total X-ray eclipse of this binary system and studied the tomography of a stellar X-ray corona. They calculated the binary orbital elements (a, e, i, ω: 2.981 × 1012 cm, 0.370, 88.2o, 311.0o respectively) and the stellar radii are RA=3.04 RΘ and RG =0.09 RΘ.

We report in this paper the spectral and timing analysis of X-ray observations of the eclipsing system α CrB , taken by XMM-Newton observations. We organized the paper as follows: The X-Ray observations and data reduction are presented in section 2, section 3 is devoted to the spectral analysis, while the results are summarized and concluded in section 4.

2. X-Ray Observations and data reduction

We used XMM-Newton observations for α CrB from the XMM-Newton archive; the observing log is given in Table 1. All EPIC cameras were operated in the small-window mode with the thick filter inserted in order to suppress the strong optical flux from the primary A star [6]. We made use of the data from the two EPIC MOS [7] cameras and the EPIC PN camera [8]. The raw data were processed with the EPIC pipeline chains of the Science Analysis System (SAS) software version 9.0. Some bad time intervals, characterized by high background events (so-called soft-proton flares), were rejected by creating light-curves for the observations (PN, MOS1, and MOS2), which are best visible above 10 Kev. To optimize the signal-to-noise ratio in the light curve and to suppress large background contributions and contributions from warm pixels in the very soft range. Because of the poverty of the hard x-ray photons of this object, the only soft X-Ray band extracted exclusively is in the energy range 0.30-2.0 Kev for the PN and 0.14-2.5 Kev for the MOS1&MOS2 cameras. The spectrum of the star was extracted using circular extraction regions centered on the star, with radii of approximately 25" for both the MOS and PN cameras. In order to utilize the $\chi 2$ technique, the X-ray spectra were rebinned to contain at least 20 counts in each spectral bin using grppha command. All the spectra were subsequently analyzed using the Xspec software (v12).

For the timing analysis, we extracted the source and background light curve by using the evselect task of SAS software version 9.0. The light curves obtained were corrected to account for a number of effects, which an impact in the detection efficiency can have like; vignetting, bad pixels, PSF variation and quantum efficiency, as well as to account for time-dependent corrections within an exposure, like dead time and GTIs, by using the SAS task epiclccorr. Because in the short time periods of the x-ray binaries, the arrival time of a photon is shifted as it would have been detected at the barycenter of the solar system (the center of mass) instead of the position of the satellite. In this way, the data are comparable. We used the SAS barycen to correct these timestamps to the Earth's barycenter for each event. The Xronos program package was used to make a timing analysis (producing a binned light curve, calculating a power spectrum, searching for periodicities etc.).

Table 1. Observing log for α CrB with XMM-Newton

Instrument	Mode	Filter	Date @Exp. Start Time	Date @ Exp. End Time
MOS1	Small-window	THICK FILTER	2001-08-27 @04:42:44	2001-08-27 @15:42:18
MOS2	Small-window	THICK FILTER	2001-08-27 @04:42:44	2001-08-27 @15:42:18
PN	Small-window	THICK FILTER	2001-08-27 @04:58:46	2001-08-27 @15:43:09

* **Corresponding Author**
Department of Physics, Faculty of Applied Science, Umm Al-Qura University, Saudi Arabia.
E-mail address: **baewiss@uqu.edu.sa**

3. X-Ray Data Analyses

The first model used to fit the spectra was a single temperature variable-abundance thermal plasma model. In this model, an emission spectrum from hot diffused gas based on the model calculations of Mewe and Kaastra with Fe L calculations. The model includes line emissions from several elements. The He element in the model was fixed at cosmic, and the normalization was calculated from following equation:

$$\frac{10^{-14}}{4\pi[D_A(1+z)]^2}\int n_e n_H dv \quad (1)$$

where DA is the angular diameter distance to the source in cm, ne & nH are the densities in cm^{-3} of the electron and hydrogen respectively [8] (in Xspec software this model called vmekal). Figures 1 to 3 explains the fit for PN and MOS, while Figure 4 is the fitting of the three detectors (PN, MOS1, and MOS2 respectively). The elements of metal abundance included in the model are C, N, O, Ne, Na, Mg, Al, Si, S, Ar, Ca, Fe and Ni. We set O, Ne, Mg, Si, S, and Fe are free parameters in the fit. We got a best fit for this single model, χ^2/odf is 141.16/121. The output temperature is 0.46±0.02, while the output values of the abundance of the elements O, Mg, S, and Fe are 0.25±0.05, 0.44±0.12, 0.52±0.27 and 0.26±0.02 respectively. The X-ray luminosity evaluated from 0.3-10.0 Kev is 5.3 × 1028 erg s^{-1}, which agrees with the luminosity reported previously [2,6]. By adding the A photo-electric absorption due to the hydrogen column density, no significant change in the fitting was seen (the results are summarized in Table 2). The simple Gaussian line profile, which was calculated from the equation

$$A(E) = K\frac{1}{\sigma\sqrt{(2\times\pi^2)}}e^{\left(\frac{-(E-E_t)^2}{2\sigma^2}\right)} \quad (2)$$

(here Et is the line energy in Kev, σ is the line width in Kev and K is the total photons/cm^{-2}/s in the line), was applied, the fitting was improved (χ^2/ odf = 123.75/ 107) (the fitting of the thermal plasma model with simple gaussian line for PN data shown in Figure 5) and we got an emission line at 1.3 Kev (all the parameter in Table 2).

The produced binned light curve for the three detectors (PN, MOS1, and MOS2) explains that the data covers the complete second eclipse (Figures 6-9). The gross shape of the ingress and egress portions of the curve is symmetric; the total ingress and egress durations are 2.74 and 1.66 hrs, respectively. During ingress and egress, a sequence of fast drops/rises in flux and several flux plateaus are evident. We can note from the light-carve figures, a strong asymmetry in all light curves, and the individual steep flux decreases and increases. We can see from Figures 5 to 7 a strong active region at the lower left of the maps, near the limb of the G component, the lower right part which in increasing means a band diagonally runs across the G star disk from lower left to upper right, close to the projected center. The upper right part has the same features as the lower part, but weaker band displaced somewhat to the right, and to the bright source of the upper right secondary limb. The banded structure from lower left to upper right may partially be an artifact since the ingress light curve decays relatively smoothly below feature of the lower right part.

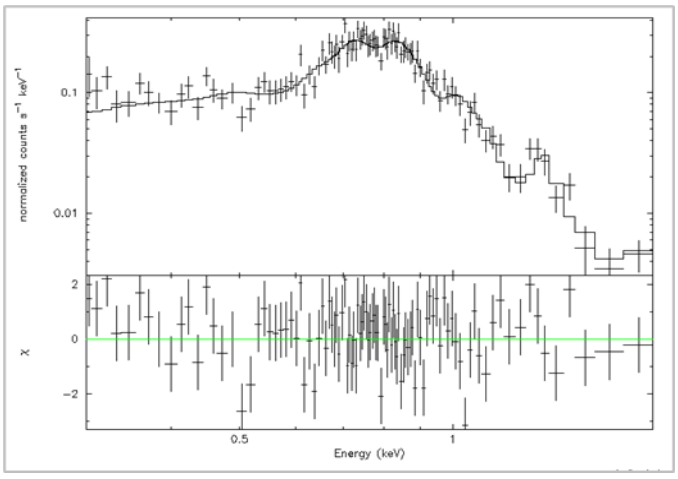

Figure 1: The EPIC PN spectrum which fitted using single thermal plasma model, with χ^2 test.

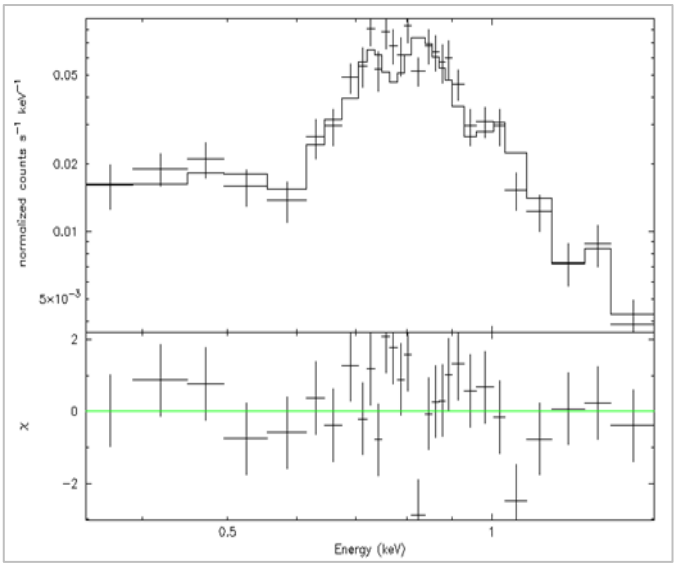

Figure 2: The EPIC MOS1 spectrum which fitted using single thermal plasma model, with χ^2 test.

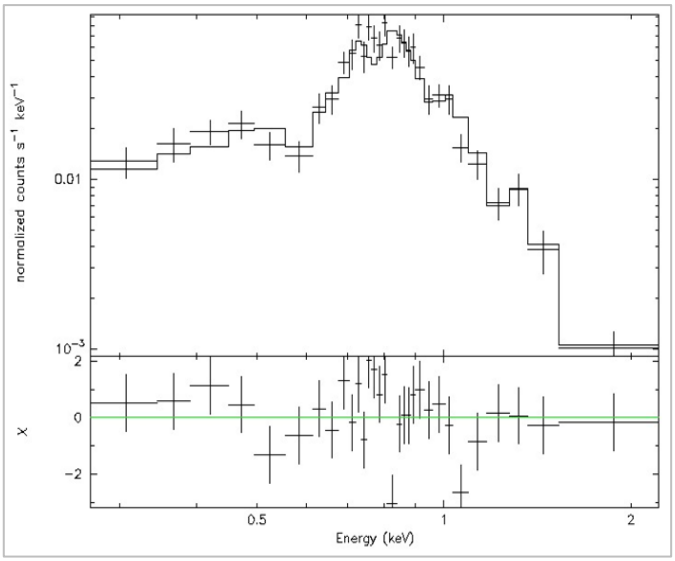

Figure 3: The EPIC MOS2 spectrum which fitted using single thermal plasma model, with χ^2 test.

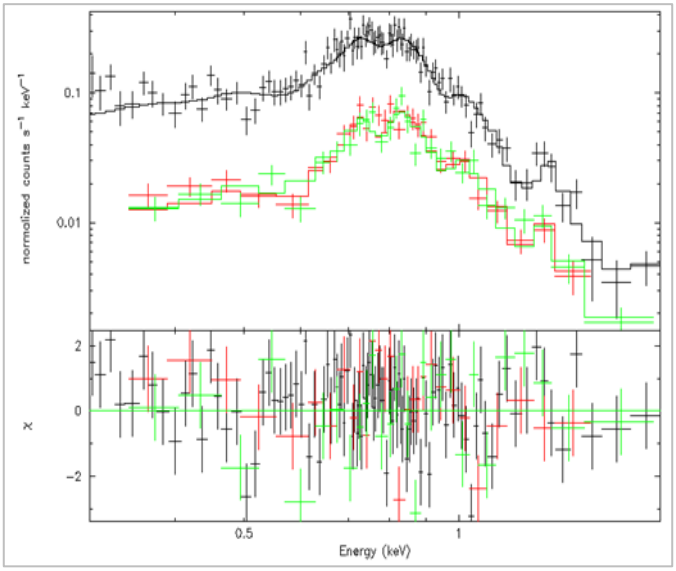

Figure 4: The EPIC PN, MOS1 and MOS2 spectra which fitted using single thermal plasma model, with χ^2 test.

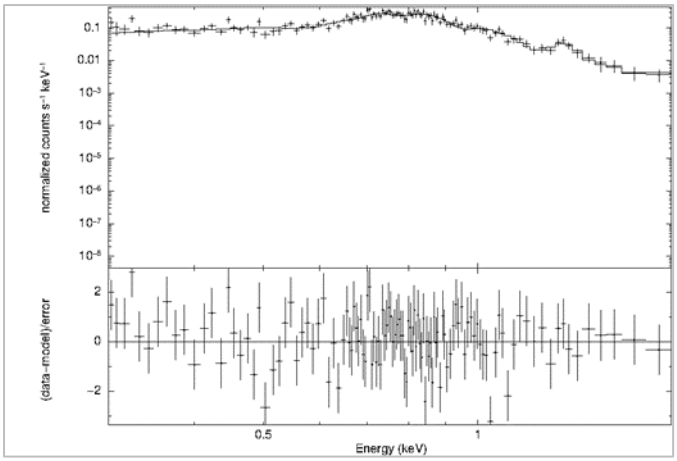

Figure 5: The EPIC PN spectrum which fitted using single thermal plasma Model and single gaussian line, with χ^2 test.

Table 2. Summarizing the parameters of the output fitting

Parameter	Thermal plasma model	Thermal plasma model+ A photo-electric absorption	Thermal plasma model+ Gaussian line
Kt	0.46 ±0.02 Kev	0.46 ±0.02 Kev	0.47 ±0.02 Kev
O	0.25 ±0.05	0.27±0.06	0.33±0.06
Mg	0.44±0.12	0.47±0.13	0.54±0.16
Si	0.52±0.17	0.56±0.28	0.37±0.19
Fe	0.26±0.02	0.28±0.03	0.31±0.06
χ^2/odf	141.16/121	140.65/111	123.75/107
Normalization	2.5×10^{-4}	2.4×10^{-4}	2.6×10^{-5}

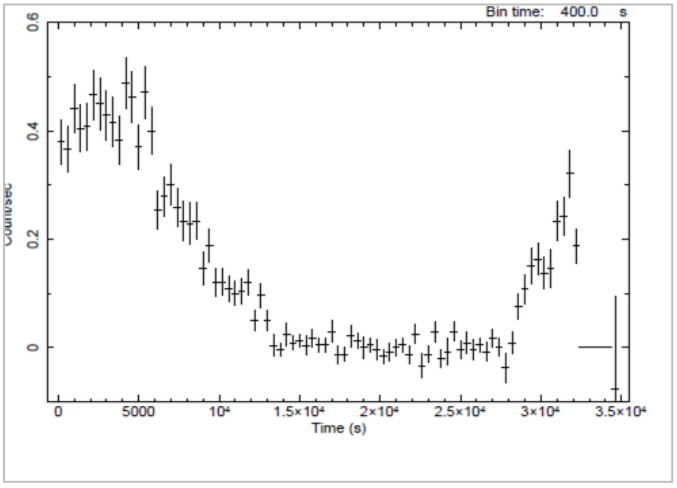

Figure 6: The X-ray light curve for PN data

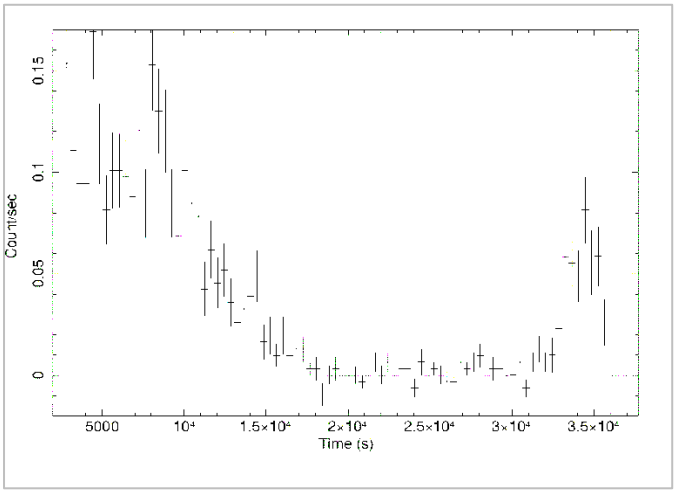

Figure 7: The X-ray light curve for MOS1 data

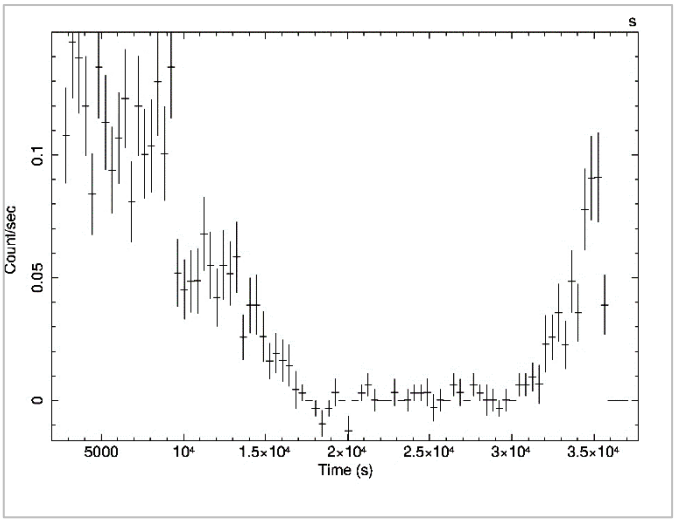

Figure 8: The X-ray light curve for MOS2 data

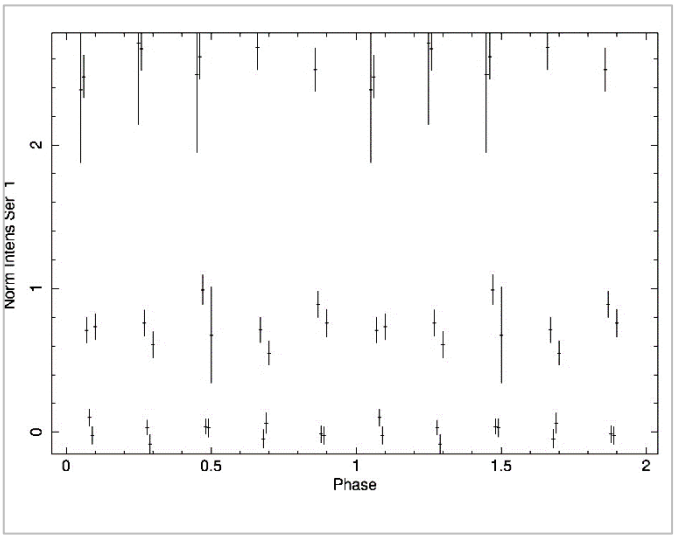

Figure 9: Phase of the eclipsing binary

4. Discussion and conclusions

A detailed spectral and timing analysis (EPIC) has been performed for XMM-Newton observation of the alpha Coronae Borealis (α CrB) system. The soft X-Ray range (0.3-2.0 Kev) is described by three models. From these models, we got the best-fit temperature in the range 0.45 to 0.47 Kev, while the abundances of the elements O, Mg, Si and Fe that have the range 0.25 to 0.33, 0.44 to 0.54, 0.37 to 0.56 and 0.26 to 0.31 respectively, are low compared to solar photospheric values. By using Guessing model there is an emission line at 1.3 Kev. From the timing analysis there is a strong active region at the lower left of the maps, near the limb of the G component, and increasing in some parts means a band diagonally runs across the G star disk from lower left to upper right, close to the projected center. Some parts indicated that a weaker band displaced somewhat to the right, and to the bright source of the upper right secondary limb. The banded structure from lower left to upper right may partially be an artifact since the ingress light curve decays relatively smoothly below feature of the lower right part.

References

[1] Güdel, M., Arzner, K., Audard, M., and Mewe, R., Tomography of a stellar X-ray corona: alpha Coronae Borealis, 2003, A&A, 403, 155-171

[2] Liedahl, D.A., Osterheld, A.L., and Goldstein, W.H., New Calculations of Fe L-Shell X-Ray Spectra in High-Temperature Plasmas, 1995, ApJL, 438, 115-127

[3] Schmitt, J. H. M. M., & Kürster, M., A Spatially Resolved X-ray Image of a Star Like the Sun, 1993, Science, 262, 215-226

[4] Schmitt1, J. H. M. M., Schröder, K.-P., Rauw, G., Hempelmann, Mittag, A, M. , González-Pérez1 J. N., Czesla1, S., Wolter, U., and Jack, D., The α CrB binary system: A new radial velocity curve, apsidal motion, and the alignment of rotation and orbit axes, A&A, 2016, 586, 1-13
[5] Schmitt, J. H. M. M., & Kürster, M., APS Conference Series, The Eclipsing X-Ray Binary alpha CrB, 1994, 64, 137-150
[6] Strüder, L.; Briel, U.; Dennerl, K.; The European Photon Imaging Camera on XMM-Newton: The pn-CCD camera, 2001, A&A, 365, L18-L26
[7] Turner, M. J. L., Abbey, A., Arnaud, M., The European Photon Imaging Camera on XMM-Newton: The MOS cameras, 2001, A&A, 365, 27-35
[8] Tomkin, J. and Popper, D. M, Rediscussion of eclipsing binarties. XV. Alpha Coronae Borealis, a main-sequence system with components of types A and G. ,1968 , AJ 92, 1428-1437

Journal of Umm Al-Qura University for Applied Science

journal homepage: https://uqu.edu.sa/en/jas/87823

Indoor Radon Concentration in Some Villages of Al-Lieth Province in Saudi Arabia

Amal Mohamed [a,b], H. T. Mahdy [c,*].

[a] *Physics Department. Faculty of Science, Umm Al-Qura University, Makkah, Saudi Arabia.*
[b] *Physics Deprt. Faculty of Science, Zagazig University, Zagazig, Egypt.*
[c] *Physics Department, College of Applied Sciences, Umm Al-Qura University, Makkah, Saudi Arabia*

ARTICLE INFO

Article History:
Submission date: 24/12/2019
Accepted date: 22/6/2020

Keywords:
Radon, solid state nuclear track detector, effective dose, sealed can technique

ABSTRACT

Building composites are a main source of radioactive radon gas. Determination of such a gas and its descendants are usually performed by passive detection technique using 105 radon detectors C-39. One hundred and five sealed were used in houses of villages in Al- Lieth Province. The radon concentration was determined using the "sealed can technique" and CR-39 solid state nuclear track detectors (SSNTDs) which were installed in different locations in every building (Kitchens, bed rooms and bathrooms). The results of the measured radon concentrations in the selected houses were analyzed and found to be in the range of 7.39 Bq/m^3 to 9.11 Bq/m^{3}in studied buildings. From the measured radon concentrations, the effective dose rate was calculated and found to be in the range from 0.17 mSv/y, to 0.21 mSv/y. The results were discussed in the light of the geographic peculiarity of the studied area.

1. Introduction

Radioactive Radon gas is created during the decay of U-238. There are many natural and industrial sources of radiation to which humans are exposed to, such as cosmic rays, terrestrial radionuclides, radon and its daughters. The highest rate of 60% comes from natural sources of radiation. Natural radiation that penetrates us from the Earth's crust varies from place to place on the Earth's surface, depending on geology, and topography [1].

Being odorless and tasteless besides being invisible, Radon is a radioactive gas formed by the disintegration of radium, in a decay chain of uranium. It emits α particles and produces many solid radioactive products called radon daughters or "progeny. Inhalation of radon gas or its progeny exposes the lung tissue to short-lived alpha emitting radionuclides that increases the risk of lung cancer. It is also suspected that Radon is a major factor of increasing skin cancer, where alpha particles induce some damages to epithelial cells due to deposition of such gas on the skin. Kidney related diseases have also been observed. This is because it receives the highest dose, amongst the body organs, after radon being transferred from the lungs to it by blood. Radon and its descendants may constitute a significant health hazard, especially if present with relatively high concentrations in poorly ventilated areas such as underground mines or caves; or badly designed houses. Radon concentration in such enclosed areas is important due to its side effects on health [2]. In closed rooms for a long duration and in air - conditioned rooms, the radiation levels may be raised due to the accumulation of radon gas [3].

Radiation exposure due to natural radionuclide's as well as high radon concentrations has been recognized in early seventies of the 20th century in building's closed spaces [4]. Due to the above consideration, measurement of radon concentration and calculating the effective dose in commonly used building construction materials in the selected area was the aim of this study.

2. Methodology

2.1. Peculiarity of Studied area

Al-Lieth region is one of the governorates of Makkah Province, located at the confluence of the Hijaz mountains on the Tihama plains on the western coast of Saudi Arabia 180 km south of Mecca and Jeddah province, see map in Fig (1). It is adjacent to the Red Sea coast. Al-Lieth is a rocky area and its geology can be divided into two main types of rocks. The first type is basically composed of a set of basements which are huge massive bodies of granitic schist complex. The second type is a series of quaternary deposits, that are located mainly close to the shoreline along a northwest-southeast direction. Wadi fills are filling the main valley of Al-Lieth area, uncomfortably overlying the underlying crystalline rocks [5].

2.2. Materials and Methods

In order to conduct the current radon measurement survey, 105 radon CR-39 detectors were installed in the study area. These detectors were distributed and installed at a carefully selected site within Al-Lieth area. Three reagents are installed in each location and distributed in the living room, the kitchen and the bathroom. The detector was put in the houses in some villages of the province Lieth in Saudi Arabia, such as (Rubue Aleayn – Bani Yazid – Tafil – Aduma- Alshiwaq). In each village, a detector was put in different houses in the bedroom, the kitchen and the bathroom. In each Village, 7 houses were considered in this study. Radon gas and its descendants were detected by solid state nuclear track passive technique using the "sealed can technique" [6,7]. A total of 105 sealed were collected from different places. Inside each container, a cylindrical plastic container having CR-39 track is placed in a diffusion chamber, see Fig (2); and is then sealed for a period of four months; during which, α particles emitted by radon and their descendants' bombard the plastic can. After such period, detectors are then developed in Sodium Hydroxide solution at 70ºC for 6 hours. After chemical etching, α particle track densities are then determined by an optical microscope as high as 400X. The radon concentration C_{Rn} (measured in Bq/m^3) could be determined by the equation (1) [8].

$$= \rho x / F t \quad (1)$$

Where ρx is track density (in tracks/mm^2), t is the exposure time in days and F is a calibration factor (0.42 ± 0.02 tracks.m^3.cm^{-2}.Bq^{-1}.h^{-1}). The Radon concentrations (Bq/m^3) and track density for standard samples are represent in Fig (3). The measured results are fitted well to a linear function, with regression factor R^2 = 0.9998.

From the measured data, the annual effective dose E (mSvy^{-1}) indoor closed room was determined by the following relation [9].

$$= C \times F \times H \times T \times D \quad (2)$$

Where, C is the radon concentration (Bq/m^3), F *is* the equilibrium factor (0.4), H is the occupancy factor (0.8), T is hours in a year (7000 hy^{-1}) and D *is* the dose conversion factor: 9×10^{-6} m Sv (Bq/m^3 h^{-1}).

* **Corresponding Author**
Physics Department, College of Applied Sciences, Umm Al-Qura University, Makkah, Saudi Arabia.
E-mail address: **eemohammad@uqu.edu.sa** (H. T. Mahdy).

Figure 1 Al – Lieth Governorate

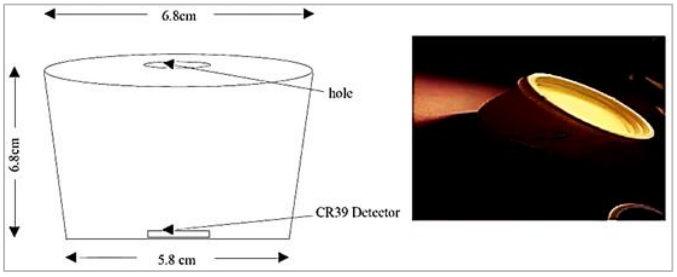

Figure 2 Sealed Can Technique.

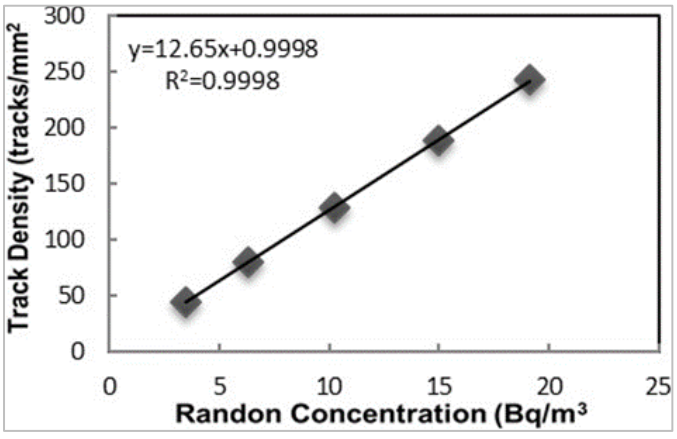

Figure 3 Radon concentration (Bq/m^3) and track density for standard samples

3. Results and discussion

Concentrations of such radon nuclides in houses reported in many publications whose indoor intensity varies according to the houses geometry, villages, and the geography of study area. The radon concentration and the annual effective dose rate were calculated according to Equations 1 and 2 respectively. The results, also, are tabulated in Table 1. It can be seen that the radon concentration varies from 7.39 Bqm-3 to 9.11 Bqm-3 with a mean value of 8.3 Bqm-.3 in the study area of Saudi Arabia. From the measured data given in table 1 the radon one can notice that alpha-activities per unit volume of the buildings were different from one place to another (Kitchens, bed rooms and bathroom) and from one building to another. The effective dose rate was found to vary from 0.17 mSv/y to 0.21 mSv/y respectively. Concentrations of such samples were found to be under the global acceptability limit which has been observed all over the world [10-15].

Table 1, lists the minimum, maximum, and average radon concentration in different types of house rooms in Al-Lieth Governorate. From the measured data, it can be seen radon concentration have their highest mean values in the kitchens compared with the other rooms. These results are consistent with early results of [16,17]. The difference in densities is because of convection current and circulation of the air inside the rooms. In other words, radon concentration could be reduced by the air exchange near windows and in kitchens. From the above remakes, one can conclude that the concentrations of the remaining samples were found to be below the global permissibility limit which is well observed all over the world. Moreover, the high concentrations of Radon in kitchens are due to the bad ventilation present in such a place, more than in bedrooms and bathrooms, which results in more accumulation of Radon. This can be attributed to the peculiarity of kitchen design in the studied area houses, where the buildings are ground floor only, and the kitchens have narrow windows and are ventilated naturally only. This means that the room usage is the main key affecting radon concentration in connection with ventilation. Therefore, rooms having continuous ventilation exhibit smaller concentration.

Table 1: The radon concentration measured the studied places in Al-Lieth Province.

Types of rooms	No. of Samples	Rn. Concentration (Bq/m^3)		Average (Bq/m^3)	Effective dose (mSv/y)
		Minim.	Maximum		
Kitchens	35	3.56	19.26	9.11	0.21
Bed rooms	35	3.56	16.18	8.4	0.19
bathroom	35	3.38	12.02	7.39	0.17
Average				8.3	0.19

4. Conclusion

The highest average radon concentration in houses and buildings have been observed mostly in kitchens and guest rooms while measured with minimum concentrations in bed rooms and living rooms. This can be due to the use of narrow windows in kitchens that lead to natural ventilation. Obtained results range from 12.02 Bq/m^3 to 19.26 Bq/m^3 with a value of 8.3 Bq/m^3 as an average, which is the less than the UNSCEAR limits. Annual effective dose from indoor air is 0.19 mSv/y in average. So although the geology of the province of Al-Lieth is a rocky region consisting of granite and sedimentary rocks, the radon concentration is permissibly distributed as follows. The high concentrations of Radon in kitchens are due to the bad ventilation present in such a place, more than in bedrooms and bathrooms, which results in more accumulation of Radon. This can be attributed to the peculiarity of kitchen design in the studied area houses, where the buildings are ground floor only, the kitchens have narrow windows, and are ventilated naturally only. This means that the room usage is related to radon concentrations, which reduces with ventilation. Rooms with good ventilation show lower concentration.

References

[1] UNSCEAR ; United Nations Scientific Committee on the Effect of Atomic Radiation. Sources and Effects of Ionizing Radiation. Report to the General Assembly, **2000**.

[2] A.K. Singh, K. Ashavani, P. Rajendra, Distribution of Radon Levels in Udaipur. *Asian J. Chem.*, **2006**, *18*, 3408-3411.

[3] UNSCEAR; Report, United Nations Scientific Committee on Effects of Atomic Radiation, UN, New York. **2017**, 12,No. E 11.

[4] D. Popovic, D. Todorovic, Radon Indoor Concentrations and Activity of Radionuclide's in Building Materials in Serbia. *Physics, Chemistry and Technology*, **2006**, *4*, 11- 20.

[5] A. A. Arafat, M. S. El-Tahwaya, H. Samrab. Comparison of Radon Concentrations In Three Types of Egyptian Houses. *J. Nucl. Radiat. Phys.*, **2018**, *13*, 147-156.

[6] A. J. Khan, R. Prasad, R. K. Tyagi, Measurement of Radon Exhalation Rate From Some Building Materials. *Nucl. Tracks Radiat. Meas*, **1992**, *20*, 609-610.

[7] J. Chen, N. M. Rahman, I. A. Itiya, Radon Exhalation from Building Materials for Decorative Use. *J. of Environ. Radioactivity*, **2010**, *101*, 317-322. https://doi.org/10.1016/j.jenvrad.2010.01.005
[8] A. Mohamed, T. H. Alsheddi, S. Almansour. Study of Radium and Radon Exhalation Rate in Some Sand Samples Using Solid State. N*uclear Track Detectors*, **2015**, *48*, 100-104.
[9] UNSCEAR Report, Exposure from Natural Sources. United Nations, New York. **2010**, 12,No. B 12.
[10] M. Al-Jarallah. Radon Exhalation from Granites used in Saudi Arabia. *J. Envir. Radioact*, **2001**, *53*, 91-98. https://doi.org/10.1016/S0265-931X(00)00110-7
[11] M. A. Misdaq, A. Amghar. Radon and Thoron Emanation from Various Marble Materials: Impact on the Workers. *Radiation Measurements*, **2005**, *39*, 421-430. https://doi.org/10.1016/j.radmeas.2004.06.011
[12] A.O. Ferreira, B. R. Pecequilo, R. R. Aquino, Application of Sealed Can Technique and CR-39 Detector For Measuring Radon Emanation From undamaged Granitic Ornamental building materials. *Radioprotection*, **2011**, *46*, 49-54. DOI: 10.1051/radiopro/20116557s
[13] M. A. Misdaq, H. Moustaaidine. A New Method for Determining Radon Emanation Coefficients and Radon Production Rates in Different Building Materials Using Solid State Nuclear Track Detectors. *J. Radioanal. Nucl. Chem.*, **1997**, *218*, 9- 12. https://doi.org/10.1007/BF02033966
[14] M. A. Kobeissi, O. EL Salmad, K. Zahraman, S. Milky., F. A. Bahson, K. M. Abumurad, Natural Radioactivity Measurements in Building Material in Southern Lebanon. *J. Environ. Radioactivity*, **2000**, *99*, 1279-1288. https://doi.org/10.1016/j.jenvrad.2008.03.007
[15] B. M. Moharram, M. N. Suliman, N. F. Zahran, S. E. Shennawy, A. R. El Sayed. 238U, 232Th Content and Radon Exhalation Rate in Some Egyptian Building Materials. *Ann. Nucl. Energy*, **2012**, *45*, 138-143. https://doi.org/10.1016/j.anucene.2012.03.008
[16] M. A. Rafat, Evaluation of radon gas concentration in the drinking water and dwellings of south-west Libya, using CR-39 detector. *Intr. J. Environ. Sci.*, **2013**, *4*, 484-490.
[17] A. Lashin et. al. Geophysical Exploration of the Western Saudi Arabian Geothermal Province: First Results from the Al-Lieth Area. Proceedings World Geothermal Congress, **2015**.